The Elastic Properties of Calcium Leached Cement Pastes and Mortars: A Multi-Scale Investigation.

by

Georgios Constantinides

B.Eng., University of London

Submitted to the Department of Civil and Environmental Engineering
in partial fulfillment of the requirements for the degree of

Master of Science

at the

MASSACHUSETTS INSTITUTE OF TECHNOLOGY

February 2002

Signature of Author .....
Department of Civil and Environmental Engineering
January 18, 2002

Certified by.....
Franz-Josef Ulm
Associate Professor of Civil and Environmental Engineering
Thesis Supervisor

Accepted by.....
Oral Buyukozturk
Chairman, Department Committee on Graduate Students

The Elastic Properties of Calcium Leached Cement Pastes and Mortars: A Multi-Scale Investigation.

by

Georgios Constantinides

Submitted to the Department of Civil and Environmental Engineering
on January 18, 2002, in partial fulfillment of the
requirements for the degree of
Master of Science

Abstract

Calcium leaching induced aging in concrete creates a new material with degraded macroscopic mechanical properties. Although the degradation of strength has been elaborately studied in the last decade, the degradation of elasticity has not been investigated in the same depth. This thesis presents a combined experimental-theoretical investigation of the loss of elastic modulus due to calcium leaching.

The first part of this thesis describes the experimental study performed on the elastic modulus of asymptotically leached cement paste and mortar. A combined qualitative-quantitative approach is adopted to characterize and quantify the chemical degradation at various length scales. The macroscopic elasticity ($10^{-2} - 10^{-4}$ m) is measured using three different techniques: (a) Ultrasonic Pulse Velocity, (b) Resonant Frequency, and (c) Uniaxial Compression. The microscopic effect ($10^{-5} - 10^{-7}$ m) is quantified using state-of-the-art Nanoindentation tests. Scanning Electron Microscope images complete the characterization by providing qualitative information about the concrete microstructure and its evolution through calcium leaching.

The second part of the thesis is devoted to modeling the experimentally observed material behavior. Based on a micromechanical approach, using different homogenization schemes available, the different levels of characterization are linked together by a new multiscale model. The macroscopic values predicted by the model compare well with the values obtained experimentally. The combined experimental-theoretical approach confirms both the deleterious effects induced by calcium leaching on concrete and the capacity of the model to predict the degradation of elasticity caused at the material level.

Thesis Supervisor: Franz-Josef Ulm
Title: Associate Professor of Civil and Environmental Engineering

Contents

List of Tables

List of Figures

Chapter 1

Introduction

1.1 Industrial Context

Concrete is a ubiquitous material and its versatility, comparative cheapness, energy efficiency and good mechanical properties made it the most widely used construction material in the world[1]. Among many applications, concrete is used in the nuclear and energy-related industry as construction material for containment barriers, liners or encasement of containers for radioactive waste disposals. In addition, most of today's nuclear power plants have a large containment structure made of concrete to shield the environment from radiation releases. Of the 110 U.S. nuclear power plants licensed for commercial operation, over 60% have a concrete containment [89]. The others use a steel containment but rely on concrete structures to provide additional radiation shielding and protection against environmental effects [64]. Because of the critical nature of nuclear contamination, the functionality and serviceability of these structures must be ensured over long periods of time - the longer, the higher the radioactivity. In the case of nuclear waste containment the time-scale of the service-life corresponds roughly to the time for

[1]Estimates in the year 2000 suggest that the approximate cement consumption is on the order of 1.625×10^9 tons. Assuming a population of 6.1 billion people, this corresponds to a per-person consumption rate of 266 kg/year, which corresponds roughly to one cubic meter of concrete. Man consumes no material except water in such tremendous quantities.

the waste radioactivity to reach the natural one. For instance, the typical time scale of interim surface storage of weak and medium radioactivity (mixed waste), in which concrete is used as waste cover, protection layer and solid construction material for container encasement, is about 300 years. It will be some orders of magnitude higher for future deep storage of medium-level and high-level radioactive waste, in which concrete (e.g., high performance cement composites) will not only be involved as protection material, but probably also as construction material of the containers [107].

The durability performance of concrete structures becomes of significant importance in cases like nuclear waste storage where concrete is applied in long term applications. Conventional design approaches (Figure 1-1) consider constant material properties and extreme loading conditions, in an attempt to ensure the load-bearing capacity of the structure throughout its intended lifetime. By contrast, a durability design approach (Figure 1-2) considers, in addition, the degradation of the mechanical properties of the material. These properties are no longer assumed constant. The ultimate goal is to preserve the functionality of the structure so that its mechanical performance, even at the asymptotic degraded state[2], meets the requirements of its usage. Durability design itself is based on intimate knowledge of the evolution of the mechanical properties over time as the material undergoes degradation processes. With this knowledge in hand, the functionality of the different structures can be ensured at all times.

The use of concrete in hazardous waste containments requires monitoring the aging kinetics at the time-space scale of the storage system. Given the time-scale of some hundred of years, the durability design approach needs to consider some reference scenario of chemical degradation and account for the effects of the chemical attack on the concrete material properties. Among possible degradation scenarios of cementitious materials, calcium leaching induced aging, in particular the one caused by pure water [18], is one of the most severe. In the case of nuclear waste containment, calcium leaching can be caused by streaming water intruding into the underground nuclear waste storage

[2]State at which no further degradation of mechanical properties can be expected.

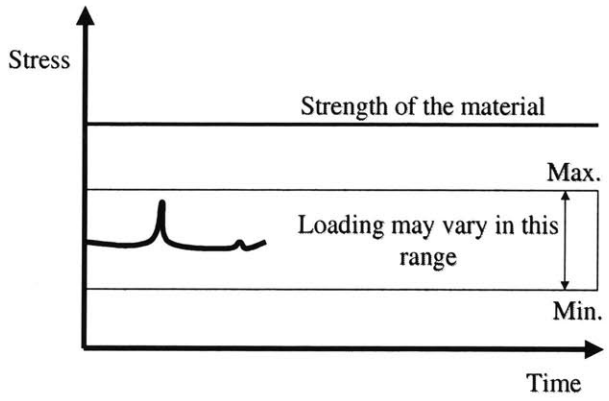

Figure 1-1: Conventional design considerations.

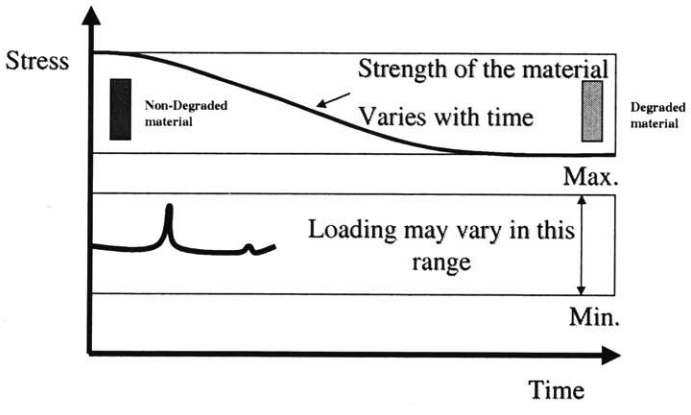

Figure 1-2: Durability design considerations. Material properties degrade with time. Ensures no overlap, at any time, with the possible loading.

structure[3]. Calcium leaching produces a new material with degraded mechanical and physical properties.

1.2 Calcium Leaching

The leaching of cement paste is a typical example of a dissolution mechanism in a porous material: a mineral that is a part of the solid matrix is dissolved in the interstitial pore solution. This diffusion-dissolution process involves propagation fronts that move at a finite velocity in the porous medium. Calcium leaching, which is similar to the "Stefan problem"[4] [104], has been studied in the last decade, both experimentally and theoretically. Most approaches limit the analysis to one global diffusion of calcium ions through the structure, and one or several skeleton dissolution processes defined by the equilibrium between the calcium concentration in the pore solution and the calcium concentration of the solid constituents [4, 18, 38], with a focus on pore space percolation and diffusivity [13]. These efforts have led to the development of some reliable tools for modeling calcium leaching, of which the main features are presented below. An analytical solution of this problem, when one dissolution front separates a completely dissolved zone from a non-degraded one, has been developed by Mainguy and Coussy [72] and is presented first.

1.2.1 Problem Formulation

Calcium leaching occurs when concrete is set in contact with a liquid phase having a lower calcium ion concentration (below the chemical equilibrium, than the one in the interstitial pore solution. Such a chemical unbalance causes the depletion of Calcium Hydroxide

[3] As part of its strategy for the management of low and intermediate (but not high) level wastes, the US Government developed a deep underground disposal facility which would isolate the waste from the environment while its radioactivity decays to safe levels [66].

[4] A problem for which Stefan first obtained in 1891 the closed-form solution.

(CH)[5] crystals and a progressive decalcification of the Calcium Silicate Hydrates (C-S-H). The chemical reaction of the dissolution of CH crystals reads:

$$Ca(OH)_2 \rightarrow Ca^{2+} + 2OH^- \tag{1.1}$$

and the simultaneous autoprotolysis reaction of water is:

$$2H_2O \leftrightarrow H_3O^+ + OH^- \tag{1.2}$$

The equilibrium concentration for the solute Ca^{2+}, or equivalently the equilibrium volumetric mass of the solute, ρ_{Ca}^{eq}, can be derived from the overall electron charge neutrality of the interstitial solution together with the solubility products of reactions (1.1) and (1.2). The equilibrium condition can, therefore, be expressed in the form:

$$\rho_{Ca} - \rho_{Ca}^{eq} = 0 \tag{1.3}$$

Consider now a cement sample in an initial equilibrium state, defined by condition (1.3); there is no dissolution of Portlandite. We assume that this sample is put in contact with permanently renewed deionized water (i.e. water of zero Ca^{2+} ion concentration). The difference in concentration between the deionized water wetting the sample and the interstitial pore solution causes the diffusion of ions toward the fresh water at the sample surface. This diffusion leads to a decrease of the ion concentration in the sample. Hence, equilibrium condition (1.3) is no more satisfied, and a dissolution of Portlandite starts to reestablish equilibrium.

The mass balance equation of the skeleton and the solute phase read:

$$\frac{\partial m_{sm}}{\partial t} + \mu_{sm \rightarrow sol} = 0 \tag{1.4}$$

[5] Cement chemists' notation is used throughout; C=CaO; S=SiO_2; A=Al_2O_3; F=FeO_3; $\bar{S}$=SO_3. Thus, C_3S=$3CaOSiO_2$. Dashes in the formula C-S-H emphasizes its variable composition.

$$\frac{\partial m_{sol}}{\partial t} + \nabla \cdot \mathbf{w}_{sol} - \mu_{sm \to sol} = 0 \tag{1.5}$$

where $\mu_{sm \to sol}$ is the rate of mass formation of the solute, $\mathbf{w}_{sol}$ is the mass flux vector of the solute, m_{sm} and m_{sol} are the apparent volumetric masses, respectively of the solid mineral bound in the skeleton (e.g., the calcium bound in the Portlandite crystals) and the same mineral in the interstitial pore solution (i.e. the solute). The apparent volumetric mass is related to the real mass density ρ_{sol} by:

$$m_{sol} = \phi \rho_{sol} \tag{1.6}$$

where ϕ is the connected porosity of the material, which defines the infinitesimal porous space $\phi d\Omega$ through which the solute diffuses.

The mass balance equations, (1.4) and (1.5), have to be completed by the transport law of the solute through the porous medium. The basic relation for reactive conductive ion transport is Fick's Law which states that the driving force of the transport solute is the concentration gradient. Formulated here in terms of the mass concentration gradient, Fick's Law reads:

$$\mathbf{w}_{sol} = -\phi D \nabla \rho_{sol} \tag{1.7}$$

where D defines the diffusion coefficient of the solute in the interstitial pore solution.

The last law to be specified is the law governing the kinetics of dissolution. In an instantaneous dissolution process, the simultaneous presence of the mineral in both solid and solute form can only occur, if a chemical equilibrium condition such as (1.3) is satisfied. The law governing this instantaneous dissolution of the mineral reads:

$$m_{sm} > 0;\ \rho_{sol} - \rho_{sol}^{eq} \leq 0;\ m_{sm}(\rho_{sol} - \rho_{sol}^{eq}) = 0 \tag{1.8}$$

where ρ_{sol}^{eq} is the equilibrium volumetric mass of the solute. According to Eq. (1.8),

the dissolution front propagating through the material volume separates an intact downstream zone, where $m = m_{sm} + \phi\rho_{sol}^{eq}, m_{sm} > 0$, and $\rho_{sol} - \rho_{sol}^{eq} = 0$, from an entirely degraded upstream zone, where $m = \phi\rho_{sol}^{eq}, m_{sm} = 0$, and $\rho_{sol} - \rho_{sol}^{eq} \leq 0$.

Use of the mass balance equations and the two transport laws of diffusion and dissolution, the following equations are obtained:

$$\frac{\partial \phi\rho_{sol}}{\partial t} + \frac{\partial m_{sm}}{\partial t} - \nabla \cdot (\phi D \nabla \rho_{sol}) = 0 \tag{1.9}$$

$$m_{sm} > 0;\ \rho_{sol} - \rho_{sol}^{eq} \leq 0;\ m_{sm}(\rho_{sol} - \rho_{sol}^{eq}) = 0 \tag{1.10}$$

$$(\phi D(\nabla \rho_{sol})_{up} - m_{sm}^{o}\mathbf{V}) \cdot \mathbf{n} = 0 \tag{1.11}$$

Eq. (1.11) is the jump condition over the discontinuity surface Σ moving through volume Ω at a normal velocity $\mathbf{V} \cdot \mathbf{n}$, m_{sm}^{o} stands for the initial concentration of the mineral in solid form. For a material initially in equilibrium, Eqs. (1.9)-(1.11) form a closed set of equations to be completed by boundary conditions.

1.2.2 1-D Diffusion-Dissolution

To illustrate the problem in hand, consider a 1-D diffusion-dissolution problem in the semi-infinite half space $x \geq 0$. The half space is in chemical equilibrium at times $t \leq 0$. For time $t > 0$ the surface $x = 0$ is subjected to a permanently renewed deionized (streaming) water, maintaining the solute at constant zero concentration. Therefore,

$$m_{sm}(x, t \leq 0) = m_{sm}^{o}; \rho_{sol}(x, t \leq 0) = \rho_{sol}^{eq} \tag{1.12}$$

$$\rho_{sol}(x = 0, t > 0) = 0 \tag{1.13}$$

Let $x_d(t)$ be the location of the dissolution front at time t. Eqs. (1.9)-(1.11) applied to the 1-D problem yield, for all $t > 0$,

$$0 < x < x_d(t) : \frac{\partial \phi \rho_{sol}}{\partial t} - \frac{\partial}{\partial x}(\phi D \frac{\partial \rho_{sol}}{\partial x}) = 0 \tag{1.14}$$

$$x_d(t) < x : \rho_{sol} - \rho_{sol}^{eq} = 0 \tag{1.15}$$

$$\phi D (\frac{\partial \rho_{sol}}{\partial x})_{x=x_d^-(t)} - m_{sm}^o \frac{dx_d}{dt} = 0 \tag{1.16}$$

The invariants of the problem (1.14)-(1.16) can be identified through the linear transform of the whole set of variables, functions and parameters involved in the problem:

$$\bar{\rho}_{sol} = \frac{\rho_{sol}}{\rho_{sol}^{eq}}; \xi = \frac{x}{2\sqrt{Dt}}; \varepsilon = \frac{\phi \rho_{sol}^{eq}}{m_{sm}^o}; \bar{m}_{sm} = \frac{m_{sm}}{m_{sm}^o} \tag{1.17}$$

The solution reads in the self-similar form:

$$\bar{\rho} = f(\xi, \varepsilon) \tag{1.18}$$

A substitution of (1.18) into (1.14) leads to an ordinary differential equation with respect to ξ. Its standard solution is the error function $\mathrm{erf}(\xi)$ multiplied by a constant factor. The solution reads:

$$0 \leq \xi \leq \xi_d : \bar{\rho}_{sol} = \frac{\mathrm{erf}(\xi)}{\mathrm{erf}(\xi_d)}; \bar{m}_{sm} = 0 \tag{1.19}$$

$$\xi \geq \xi_d : \bar{\rho}_{sol} = 1; \bar{m}_{sm} = 1 \tag{1.20}$$

The remaining unknown ξ_d, which defines the location of the dissolution front, is obtained as a function of ε by solving the equation resulting from the substitution of (1.19) into (1.16):

$$\varepsilon \exp(-\xi_d^2) = \sqrt{\pi}\xi_d^2 \operatorname{erf}(\xi_d) \tag{1.21}$$

1.2.3 Application to Cement-Based Material

Deionized water in contact with cement-based materials induces concentration gradients and generates the diffusion of ions contained in the interstitial pore solution. In turn the chemical equilibrium is modified. This leads to the leaching of the material. For its major part, this process involves the leaching of calcium from the solid skeleton. In addition, it has been experimentally found [4] that the amount of calcium leaching in time depends almost linearly upon the square root of time. The implication of this finding is that calcium leaching of cement paste is governed, in time and space, by a diffusion-dissolution process with instantaneous dissolution kinetics. The main features of a diffusion-dissolution process have been developed through the 1-D reference problem in Section 1.2.2.

However, the simple model is not totally representative of the "real" leaching process in cement-based materials. In fact, the leaching process involves the calcium of different minerals of the solid skeleton (CH, C-S-H, Ettringite etc.). During the leaching process these minerals dissolve progressively driven by the different equilibrium concentrations. This implies that the equilibrium molar concentration of the calcium in the interstitial solution, noted c_{Ca} (in mol/m^3) depends on the overall molar solid concentration, s_{Ca}, of calcium bound in the different minerals forming the solid matrix. To overcome this problem, it is common practice to introduce an empirical state function, which expresses the solid concentration of the main constituent bound in the minerals involved in leaching, as a function of the concentration of this constituent in its solute form in the interstitial solution. Expressed in a normalized form, this chemical equilibrium condition can be written in the form:

$$s_{\mathrm{Ca}}/s_{\mathrm{Si}} - g(c_{\mathrm{Ca}}) = 0 \tag{1.22}$$

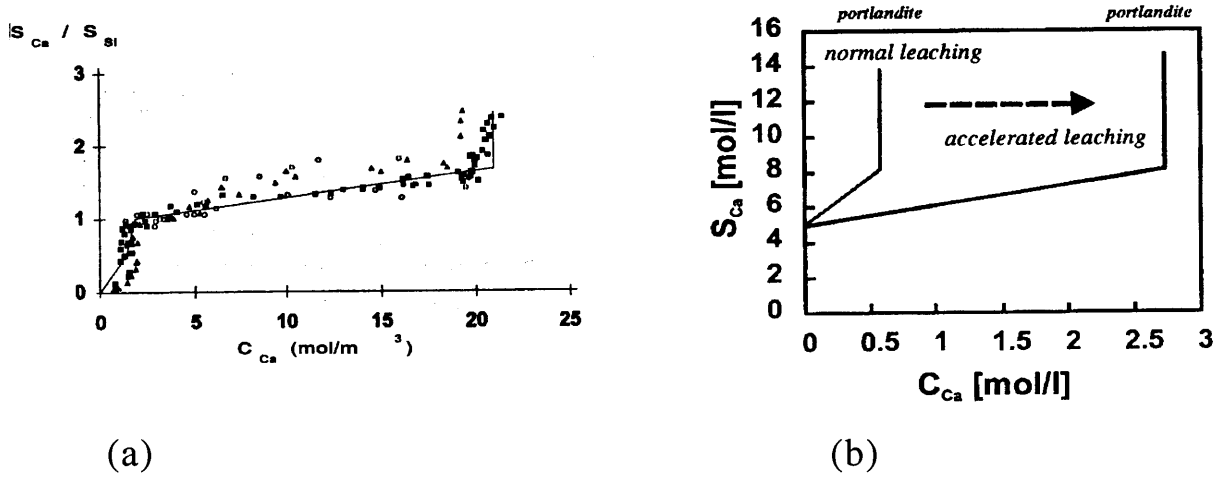

(a) (b)

Figure 1-3: (a) Relation between normalized Calcium/Silica concentration in the solid matrix versus Calcium concentration in the interstitial solution; from the compilation of data by Berner [15] (b) Calcium concentration of solid versus solute in both normal and accelerated leaching conditions [105].

where s_{Si} is the molar silica concentration bound in the solid matrix.

The plot of experimental data of this chemical equilibrium condition for different cement pastes is given in Figure 1-3(a), where ratio $s_{\mathrm{Ca}}/s_{\mathrm{Si}}$ is plotted versus solute calcium concentration c_{Ca} at equilibrium from the compilation of data by Berner [15]. It is remarkable that the experimental values for different cement pastes almost coincide, suggesting that the equilibrium curve, Eq. (1.22), is a general characteristic of cement paste leaching. The different equilibrium points in Figure 1-3(a) (from right to left) represent the progressive dissolution of the different minerals bound in the skeleton: Portlandite is the first to dissolve at a molar solute calcium concentration of 21 mol/m^3. With decreasing c_{Ca} a progressive decalcification of the C-S-H and Ettringite occurs, leading to multiple degradation fronts. With $s_{\mathrm{Si}} = 4900$ mol/m^3, which does not vary significantly during the leaching process [57], the chemical equilibrium condition between the calcium concentration of the solid matrix s_{Ca} and the one in the interstitial pore solution is obtained:

$$s_{\mathrm{Ca}} - f(c_{\mathrm{Ca}}) = 0 \tag{1.23}$$

The experimental equilibrium curve is given in Figure 1-3(b).

In addition, the leaching of calcium from the solid matrix leads to a significant increase of the porosity which makes the diffusion problem non-linear. This variation of the porosity must be taken into account in the expression of the effective diffusion coefficient, which strongly depends on the porosity. Experimental data by Tognazzi [103] suggest a function of the form:

$$D_{\mathrm{Ca}}(\phi) = D_o \exp(\alpha\phi) \tag{1.24}$$

where D_{Ca} represents an effective diffusion coefficient. Collecting all the results above, the leaching process is governed by equilibrium equation (1.23) and the non-linear diffusion equation:

$$\frac{\partial}{\partial t}[\phi(s_{\mathrm{Ca}})c_{\mathrm{Ca}}] + \frac{\partial s_{\mathrm{Ca}}}{\partial t} - \nabla \cdot [D_{\mathrm{Ca}}(\phi(s_{\mathrm{Ca}}))\nabla c_{\mathrm{Ca}}] = 0 \tag{1.25}$$

where $D_{\mathrm{Ca}}(\phi)$ and $\phi(s_{\mathrm{Ca}})$ are given empirically found functions of the material, [72].

1.2.4 Accelerated testing

The equilibrium curve shown in Figure 1-3(b) corresponds to normal leaching conditions in cement-based materials. Accelerating this slow procedure requires accelerating the diffusion-dissolution processes in the material, by increasing the calcium efflux of the sample (i.e. increasing ε in Eq. (1.17)). This can be achieved by adding other solutes that shift the equilibrium curve to higher equilibrium c_{Ca} values (Figure 1-3(b)). Replacing water with an ammonium nitrate solution was first introduced by Carde [20], while an electrochemically induced leaching process was pioneered by Saito [93] and Gérard [38]. While the ammonium nitrate solution achieves an acceleration of the leaching process due to the increased calcium concentration gradient in the attacking fluid phase, the

electrochemical acceleration results from the strong electrical potential difference. Accelerated leaching process allowed for degraded material to be studied and their mechanical performance to be investigated.

1.3 Mechanical Properties of Calcium Leached Material - Research Objectives

Calcium leaching produces a new material with increased porosity and reduced macroscopic mechanical properties. The effect of calcium leaching on cementitious material has been investigated by several researchers with emphasis placed on the degradation of strength [4,20–22,55,56,107,108]. The degradation of elasticity, however, has not been investigated to the same extent. Macroscopic (10^{-2} m) elastic modulus measurements have been performed and a macroscopic model within the framework of chemo-mechanics has been proposed [108]. Stress-Strain curves obtained from three-point bending and uniaxial compression tests, as well as damage models, have been reported by Carde [20–22] and Gérard [38], respectively. However, little is known about the effect of calcium leaching on the intrinsic elastic properties of the individual cement paste constituents. In addition, existing micromechanical models concentrate on the centimeter scale, treating concrete as a two-phase material consisting of rigid inclusions (sand and/or aggregates) embedded in a porous matrix (cement paste or mortar), e.g. [47,64,118]. Since the chemical attack occurs at a much lower length scale, these models do not allow to capture the effect of chemical degradation on the macroscopic effective elastic properties.

The focus of this thesis, therefore, is to investigate in depth the effect of calcium leaching induced aging on the elastic properties of cement paste and mortar. The investigation aims (1) to describe in a qualitative and quantitative way the elastic properties of the two asymptotic states of degradation, and (2) to model the behavior using existing micromechanical theories. In particular, the combined experimental-theoretical approach focuses on:

1. Assessing, in a qualitative and quantitative way, the multi-scale degradation of the elastic modulus of cement paste and mortar. An effort is made to isolate the effect of leaching on the individual constituents in an attempt to identify the Achilles' heel of concrete.

2. Bridging between the micro- and the macro-scale. Such a scale-bridging approach shall capture and quantify the effects of chemical degradation on the macroscopic effective elastic modulus of cement paste and mortar.

The first objective is achieved by means of an experimental study measuring the elastic properties of the material at different length scales. The second is achieved by a multi-step homogenization approach that bridges the different existing length-scales of cement paste and mortar.

1.4 Thesis Outline

The thesis is structured in the following way: Chapter 2 gives a description of the multiscale structure of concrete materials. In this chapter, the constituents composing the multiphase composite are presented, and the different constituents are categorized in terms of their length scale. Chapters 3 to 5 present the experimental results performed on calcium leached material at different length scales. The experimental program adopted, as well as a description of the different used materials and specimen preparation are presented in Chapter 3. The series of macroscopic tests is discussed in Chapter 4, and the microscopic one is focus of Chapter 5. Chapters 6 and 7 deal with the modeling of calcium leached materials. Different homogenization schemes available in the open literature are discussed in Chapter 6. Chapter 7 is devoted to modeling the experimentally observed material behavior. The conclusions drawn from this study and perspectives for future research are developed in Chapter 8.

1.5 Research Significance

Providing the means of quantifying and modeling the degradation of the elastic modulus is a significant input to the durability design of concrete materials and structures, and contributes to preserving their service state in both space and time.

A 1996 report from Oak Ridge National Laboratory [89] stated that:

> *"By the end of this decade, more than 60 U.S. commercial nuclear power plants will be more than 20 years old, with some nearing the end of their initial operating license period. Faced with the large costs of shutting down and cleaning up reactors and replacing lost generating capacity with other sources, many U.S. utilities are expected to seek extensions of their initial plant operating licenses (nominally a 40-year period). Although mechanical and electrical equipment in a plant can be replaced, it would be extremely difficult and economically unattractive to replace a concrete containment structure. To get approval from the NRC[6] for a continuation of service, utilities must provide evidence that the concrete structures will continue to perform as designed."*

Experimental data and model provided in this report can contribute to the quantitative assessment of the aging of nuclear power plants and assist managers with the decision process concerning whether the power plants in consideration can continue to perform satisfactorily. Furthermore, additional information is gained on the microstructure of the most widely used construction material in the world and its performance in the calcium leached state. Although this research was motivated from the reference scenario of degradation of nuclear containments, results provided in this report will be valuable for many other applications involving calcium leaching of cementitious materials. Figure 1-4 shows some examples of structures susceptible to the risk of calcium leaching.

[6] *Nuclear Regulatory Commission*

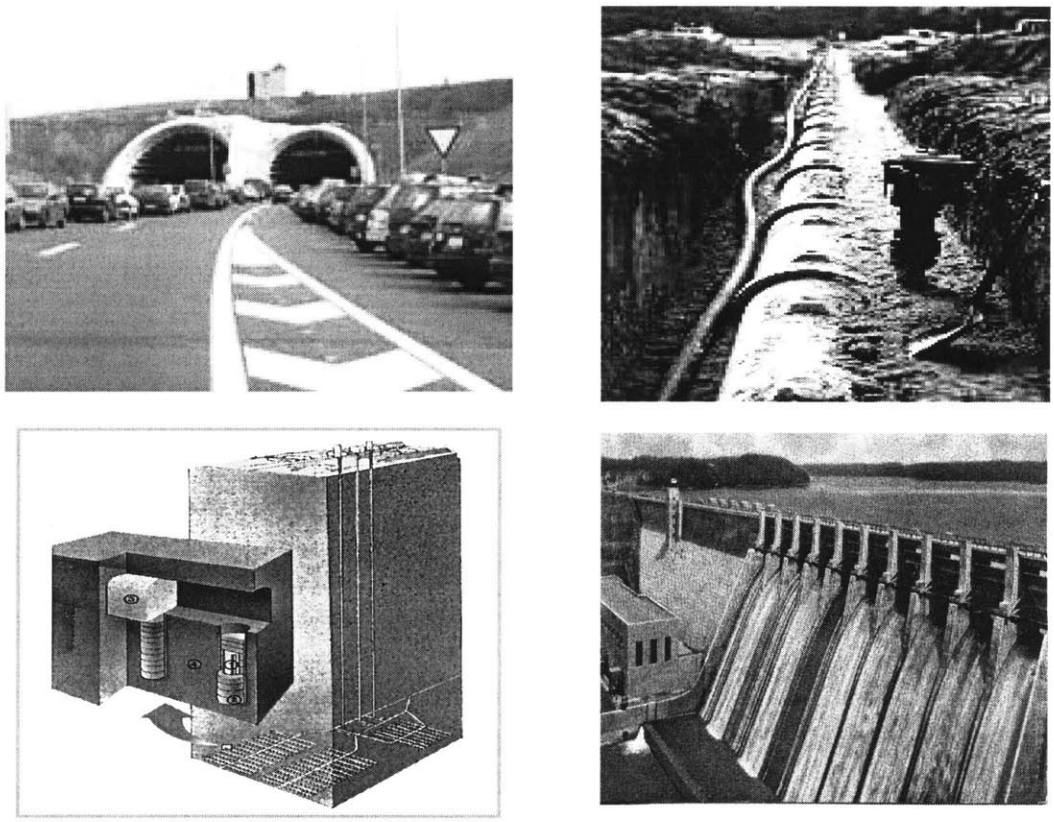

Figure 1-4: Examples of structures subject to the risk of calcium leaching induced aging (From left to right: Tunnels, Pipes, Nuclear waste containments, Dams).

Chapter 2

Multiscale Structure of Concrete

Concrete has a highly heterogeneous and complex structure. The microstructure contains random features over a wide range of length scales, from nanometer to millimeters, with each length scale presenting a new random composite. The calcium silicate matrix ('gel') is a random composite at the nanometer scale. Cement paste has a complex microstructure at the micrometer scale, and the random arrangement of aggregates (coarse and fine) in concrete makes it a random composite at the millimeter scale. In its actual use, at the length scale of meters, concrete is usually considered to be a uniform material, with bulk characteristic properties like elastic modulus, compressive strength and others [35]. This is the usual engineering scale, where effective properties are required to assist engineers in the design process. In this chapter, we develop a "multiscale picture" of concrete based on information found in the open literature. The focus of this review is two-fold: (i) to provide the means to understanding the physical effect of chemical degradation on concrete; and (ii) to develop the basis for modeling its elastic behavior. First, the structure of concrete is identified. Then the different constituents are classified in terms of their length scales. It is shown that the suggested "multiscale picture" satisfies the "separation of scale" principle which is necessary for the micromechanical development later on.

2.1 Structure of Concrete

Figure 2-1(a) shows a section through a typical concrete specimen in which hardened cement paste has the role of a matrix, binding together fine and coarse aggregates. A magnified version is given in Figure 2-1(b), and highlights the individual constituents composing the multiphase material. This presentation of the multiscale structure of concrete is divided in two parts: the first part gives an account of the cement paste microstructure, which constitutes the key component for any cement based composite; In the second part an extension to mortar is presented. This approach can be easily adopted to any other cement-based composite material.

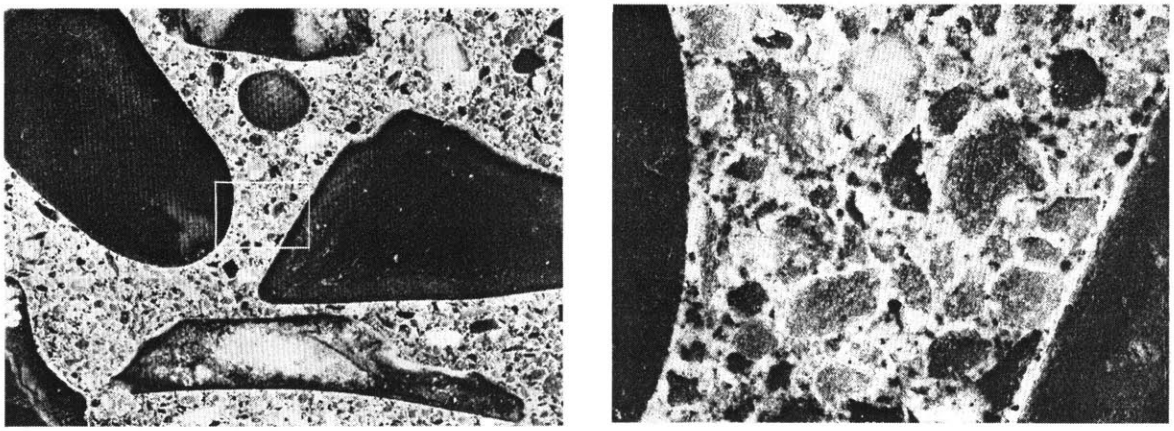

(a) (b)

Figure 2-1: Structure of a typical concrete with a magnified view [16].

2.1.1 Hardened Cement Paste (hcp)

Cement paste is a multiphase composite material. It consists of the hydration products of the different cement phases and residues of unhydrated cement particles, of pores and water. Although there are 5 distinct phases in the cement paste, which are detailed below, there are two phases that dominate in volumetric proportions: C-S-H and CH,

which constitute more than 85% of the total volume.

Calcium Silicate Hydrates - C-S-H

Calcium silicate hydrates build up the main binding phase in all Portland cement-based systems. They account for $50 - 60$ % of the volume, and are considered to be the most important contributors to the elastic properties of hcp. The fact that the term C-S-H is hyphenated signifies that it is not a well defined compound, but that exists in several different forms [101, p. 123]. For an Ordinary Portland Cement (OPC) the C/S-ratio varies between 1.2 and 2.3 with a mean of 1.75, and the structural water content, that is the water chemically bound in the crystal structure, varies even more [92]. The morphology of C-S-H also varies from poorly crystalline fibers to a reticular or crumbled sheet-like network. Of primary importance is their colloidal nature[1], with an extremely high surface area of 100 to 700 m^2/g (about a thousand times greater than the surface area of cement particles). Due to their colloidal dimensions and a tendency to cluster, C-S-H crystals could only be visualized with the advent of electron optical microscopy. First indications of the main features of the C-S-H nanostructure (atomic scale) were obtained from comparisons with already known (about 30) crystalline calcium silicate hydrates [14]. It was suggested that C-S-H resembles the natural mineral of Tobermorite [46] or the mineral of Jennite [75]. A great deal of information has been gained on the nanostructure of C-S-H in recent years principally from the use of trimethilsilylation (TMS) and solid state nuclear magnetic resonance (NMR) spectroscopy. The model of Taylor [101, p. 118] together with more recent contributions from Richardson [92], Jennings [61], Faucon [32] and other researchers suggest that C-S-H can be visualized as a Tobermorite with many imperfections and irregularities; such that it becomes nearly amorphous, possibly intermixed at a very fine scale with a similar version of Jennite. In addition, it has been found that C-S-H consists of dimeric and higher polymeric

[1] A system of finely divided particles, which are approximately 10 to 10,000 angstroms in size. 1 angstrom = 10^{-10}m.

species, mainly linear pentamers and octamers, suggesting a 2,5,8...(3n-1) sequence of linear silicate chain lengths. It is also generally accepted that dimers dominate in high C/S-ratios, and that the chain length by polymerization increases with decreasing C/S-ratio [92]. It is worth noting that calcium leaching with deionized water leads to a decrease of the C/S-ratio, to approximately C/S = 0.6 [56], which favors polymerization.

Calcium Hydroxide crystals (CH)

Calcium hydroxide (CH) is often described by the name Portlandite. It occupies 20 – 25 % of the solid volume in hcp, and appears to grow in regions initially occupied by water. In contrast to C-S-H, CH is a compound with a definite stoichiometry [77, p. 25]. Under ideal conditions of crystallization, it tends to form crystals with a distinctive hexagonal prism morphology [101, p. 116]. But as hydration proceeds, the main deposits of CH become massive and of indeterminate shape, though the good cleavage persists. Actual crystal sizes vary from a few μm to several hundreds of μm, and depend on temperature, hydration time, available space, and impurities present in the system [77, p. 25]. Transmission Electron Microscope (TEM) studies show that a small proportion of the CH in cement pastes, especially in the case of low $w/c-$ratio, is cryptocrystalline and intimately mixed with the C-S-H [45]. Inclusions of CH at that scale were also identified by decomposition and diffraction patterns [101, p. 118].

The large crystals and small surface area make CH a limiting contributor to the strength of hcp. However, CH crystals provide some additional stiffness to cement paste. In fact, at the scale of μm, the cement paste matrix can be considered as a composite material of C-S-H gel with stiff CH crystals as inclusions. Due to the high solubility of CH, the presence of CH makes concrete more vulnerable to chemical attack.

Minor compounds: Calcium sulfates, aluminates and ferrites

Calcium sulfates, aluminates, and ferrites occupy approximately 15% of the solid volume in the cement paste. Their contribution to the macroscopic mechanical performance is

limited. However, in the case of calcium leaching, some of these compounds become important, in particular the trisulfate hydrate, also called Ettringite, which forms needle shaped prismatic crystals. The influence of Ettringite becomes particularly significant for mortars, because of the tendency of Ettringite to accumulate in the aggregate-cement paste interface [74, p. 23]. In fact, Ettringite, together with CH crystals, dominate the interface properties. It should also be noted that in ordinary Portland cement paste, Ettringite eventually transforms into monosulfate hydrate, C_4ASH_{18}, which forms hexagonal, plate crystals. The characteristic length scale of these compounds is in the range of 10^{-8} m to 10^{-6} m [101, p. 123].

Unhydrated cement grains-Clinker

The proportional presence of unhydrated cement grains highly depends on the cement particle size and degree of hydration. Some clinker grains can be found in concrete even long after hydration. Their particle size in modern cement is anywhere between 1 to 50 μm, where 50 μm is usually the maximum cement particle size in modern cements [5]. As the hydration proceeds, the smallest particles dissolve first, and the large ones gradually start decreasing in size. Due to the limited space available, the hydration products tend to crystallize in close proximity and appear as a coating to the clinker grain. In addition, since the hydration product occupies more space than the cement from which it forms, complete hydration cannot occur if the $w/c-$ratio is below a certain value. Powers and Brownyard demonstrated experimentally that a $w/c-$ratio of 0.38 is sufficient to completely hydrate the cement in a mix [84, p. 33].

Pore structure of hardened cement paste

It is generally agreed that the pore structure of hcp consists of several ranges of voids, which can strongly influence the mechanical behavior. According to the International Union of Pure and Applied Chemistry pores can be classified according to their width (see Figure 2-2) as follows:

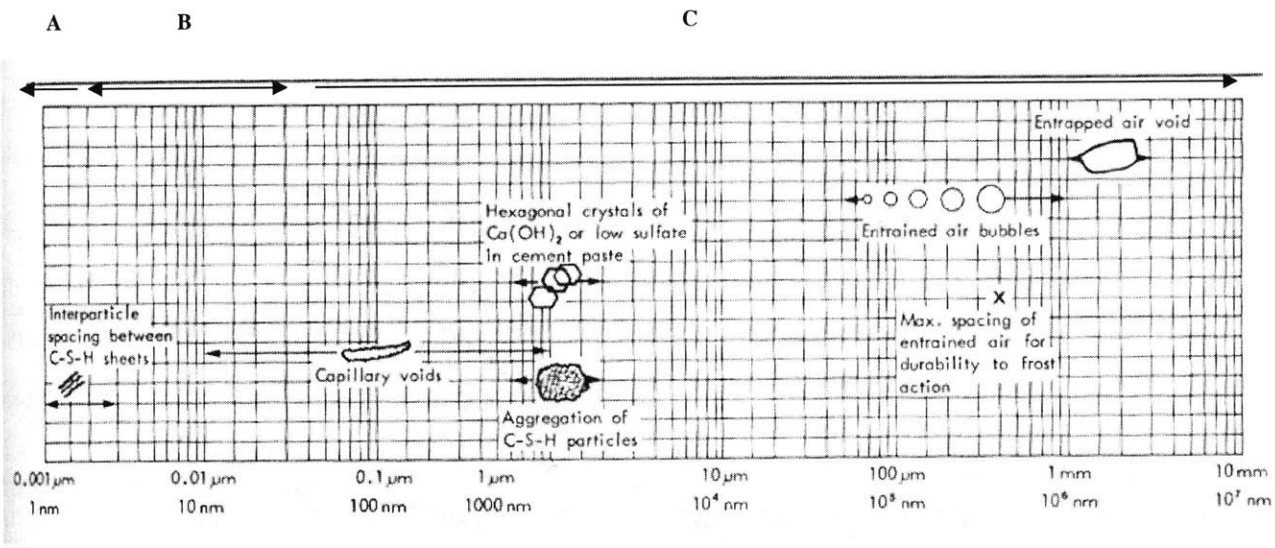

Figure 2-2: Classification of the different pores that might be present to concrete according to their size. The range of CH and C-S-H clusters is also indicated [77, p. 27].

- (A) Micropores < 2 nm
- (B) Mesopores 2-50 nm
- (C) Macropores >50 nm

Micropores (A) are formed by the interlayer spacing within the C-S-H structure, and are often referred to as "gel pores". Several models have been proposed for the C-S-H structure at this scale and as a result various values for the gel pores can be found in the open literature. According to Powers [84, p. 33] the interlayer space is 1.8 nm and accounts for 28 % porosity in solid C-S-H. On the other hand, Feldman and Sereda [33] suggest that this space varies from 0.5 to 2.5 nm. This void size is too small to have an adverse effect on the macroscopic stiffness of hcp. However, water in these small voids can be held by hydrogen bonding, and its removal under certain conditions may contribute to drying shrinkage and creep. It should be noted that the interlayer space within the C-S-H phase is considered as a part of the solid phase in hcp.

Mesopores (B) refer to capillary voids, which represent the unfilled residues of the space between the cement grains. The total volume of a cement-water mixture remains essentially unchanged during the hydration process. By contrast, the average bulk density of the hydration products is considerably lower than the density of anhydrous Portland cement. Thus, cement hydration may be looked at as a process during which the space originally occupied by cement and water is replaced more and more by the space filled with hydration products. The space not occupied by the cement or the hydration products forms the capillary pore space. The volume and size of the capillary voids is determined by the initial distance between the anhydrous cement particles in the freshly mixed cement paste (i.e., $w/c-$ratio) and the degree of cement hydration. In well-hydrated, low $w/c-$ratio pastes, the capillary voids may range from 10 to 100 nm. In high $w/c-$ratio pastes at early ages of hydration, the capillary voids may be as large as 3 to 5 μm. It has been suggested that the pore size distribution, not the total capillary porosity, is a better criterion for evaluating the characteristics of hcp [77, p. 27].

Macropores (C) form the upper range of capillary pores and air voids. They are generally spherical and are usually attributed to improper vibration, i.e. entrapped air during mixing (as large as 3 mm) or entrained air voids introduced with the aid of admixtures (50 to 200 μm). Both are much larger than the capillary voids and may adversely affect the mechanical properties of concrete.

Diamond, in his recent paper "Aspects of concrete porosity revisited" [29] noted:

> *"Experimental evidences of SEM images suggest that some of the pores are elongated, irregular and highly convoluted in outline. Others are triangular or ovoid in outline and are bounded by a definite rim, consisting of a narrow thickness of C-S-H. It would appear reasonable that the irregular, convoluted porosity may be directly inherited from original water filled space. It is rather more difficult to attribute the enclosed pores as descendants of a continuous fluid phase. This suggests that a significant portion of at least the larger pores found in hcp is considered to be derived from the hollow shell (Hadley grain)*

hydration mechanism."

Such pores represent a space that is rather within than in between the original cement grains. This type of pores is associated with diffusion processes, and it is present in cement pastes of low w/c-ratios [29].

2.1.2 Mortar/Concrete

The introduction of sand and/or aggregates into a cement-based system is predominantly responsible for the good shielding properties [64] and the elastic stiffness enhancement of concrete. However, their presence introduces an "aureole" of lower mechanical properties that affects the macroscopic mechanical performance. This specific interface needs to be considered when dealing with the elastic behavior of mortar or concrete.

Interfacial Transition Zone (ITZ)

There are several existing interfaces in cement-based composite materials, all of which weaken the composite stiffness. The most important one which in its contribution overshadows the rest, is the aggregate-cement paste interface, the so-called interfacial transition zone (ITZ). The microstructure of cement paste in the vicinity of an aggregate particle in mortar and concrete differs from the one further away from the aggregate and from that in neat cement paste. Continuous research and technological improvements in the last 50 years resulted in a significant increase in knowledge of the microstructure and mechanical properties of the ITZ. The nature of the microstructure is shown in Figures 2-3(a) and 2-3(b). The thin layer immediately adjacent to the aggregate surface has an approximate thickness of 1 μm and includes products from reactions between the aggregate and the cement paste. The nature of the surface layer has been a matter of much debate. Barnes et al. [8] characterized the layer as a duplex layer consisting of calcium hydroxide crystals on the side of the aggregate, and C-S-H on the cement paste side. Zhang et al [115], Monteiro [81], Ping and Beaudoin [90] verified the existence of

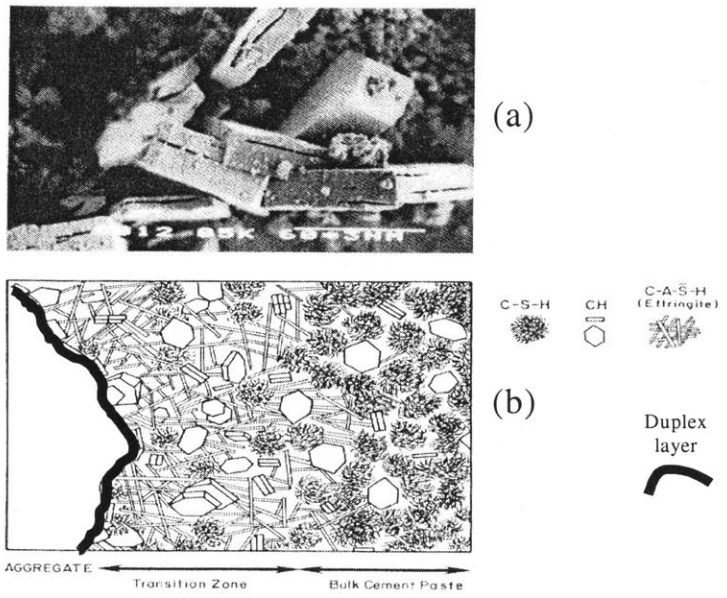

Figure 2-3: (a) SEM picture of the CH crystals in the ITZ. Their tendency to orient their c-axis perpendicular to the aggregate surface can be observed. (b) Schematic representation [81].

this layer, but did not provide evidence of the presence of calcium hydroxide crystals. Maso [74, p. 23] suggests that the techniques used were incapable of detecting the CH layer, which is probably less than one μm thick. The effect of the duplex layer on the mechanical performance of concrete is still not clearly understood. If CH dominated in the ITZ, its effect on calcium leached mortars would be indeed important.

In addition to this layer, there is a significant area of microstructural gradients and increased porosity. It was suggested that the presence of aggregates affects the original packing of the cement grains, which in turn determines the subsequent development of the microstructure [74, p. 23]. This phenomenon, which is often referred to as "wall effect", prevents large cement particles (> 10 μm) to come close to the aggregate surface. This leads, in the vicinity of the aggregate, to a larger effective $w/c-$ratio [74, pp. 8-14], and higher concentrations of calcium hydroxide, Ettringite and porosity, and a lower concentration of C-S-H. The width of this zone is on the order of the size of the largest cement particle, that is $40 - 50$ μm, as simulations by Garboczi [34] and experiments by other researchers, e.g. [74, pp. 8-14] [74, p. 23] [115–117] show. In mature concrete a zone of about 20 μm was found to have an increased porosity, and a high connectivity of the pore structure [81].

In summary, the formation of the ITZ is due to the asymmetric distribution of water in the paste. In general, approaching the aggregate surface:

- The porosity increases;
- The amount of CH increases and may become oriented (the longitudinal or c-axis perpendicular to aggregate surface);
- The amount of Ettringite increases;
- The amount of anhydrous cement decreases.

These trends are sketched in Figure 2-4. Finally, we note that the dominant volumetric proportion of CH and Ettringite in the ITZ suggests that the ITZ significantly affects the elastic performance of calcium leached mortar and concrete.

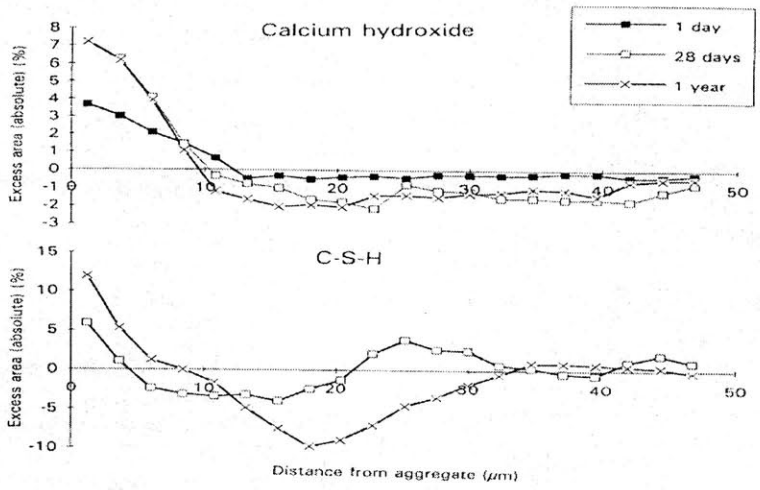

Figure 2-4: Excess percentage of products compare to the bulk cement [74, p. 23].

Finally, although several researchers performed quantitative analysis on the ITZ (e.g. nanoindentation [116, 117], pull-out tests [87], etc.) and several models have been proposed [37, 71], a generalization can hardly be made, as the disturbed packing is a function of several parameters: particle size distribution (of cement), $w/c-$ratio, aggregate/cement ratio, mixing and settling of the concrete, and so on [74, pp. 8-14].

Structure of Aggregate

Cement paste has very good mechanical properties. However, the two main drawbacks,- cost and dimensional instability- suggest that any stiff, cheap filler is beneficial, thus justifying the use of aggregates in large proportions. The aggregate phase usually occupies 70-80% of the total concrete volume, and it is predominantly responsible for the unit weight, elastic modulus and dimensional stability of concrete. Typical range of specific gravity for rocks is $2.55 - 2.75$ and therefore all concretes have similar densities, usually in the range of $2250 - 2450$ kg/m^3. While the high stiffness and volumetric proportions of aggregates significantly contribute to the elastic properties of the composite, the introduction of an additional phase introduces the ITZ which affects the elastic behavior

of the material.

The main aggregate properties that may influence the hardened concrete behavior are the following:

- While size and shape of the aggregates do not have a direct effect on the properties, it is reported that the larger the size and the higher the proportion of elongated and flat particles, the higher the tendency for water to accumulate at the immediate aggregate vicinity [60]. This phenomenon called internal bleeding (Figure 2-5(a)) causes a weaker ITZ, and it indirectly reduces strength and stiffness.

- Grading of aggregates is generally used to achieve the best packing possible and minimize the void space in between. This reduces the amount of paste needed, thus the costs, and improves the mechanical performance of concrete [84, pp. 108-181].

- Texture and surface characteristics have an effect on the ITZ. It was reported that surface roughness can improve the bonding between aggregate and cement paste [74, p. 23]. However, variations among commonly used aggregates were insignificant.

- While the chemical and mineralogical composition of aggregates (disregarding silica aggregates) does not significantly affect the behavior of concrete, however, some aggregates might influence the "duplex layer" immediately adjacent to the aggregate surface, by changing the mineralogical composition of the duplex layer, and thus the mechanical properties, as strength studies show [74, p. 23]. Arrows in Figure 2-5(b) show the likely fracture surfaces for different aggregates, which suggest that the composition of the aggregate may affect the mechanical properties of the duplex layer. The effect on elasticity, however, has not been studied.

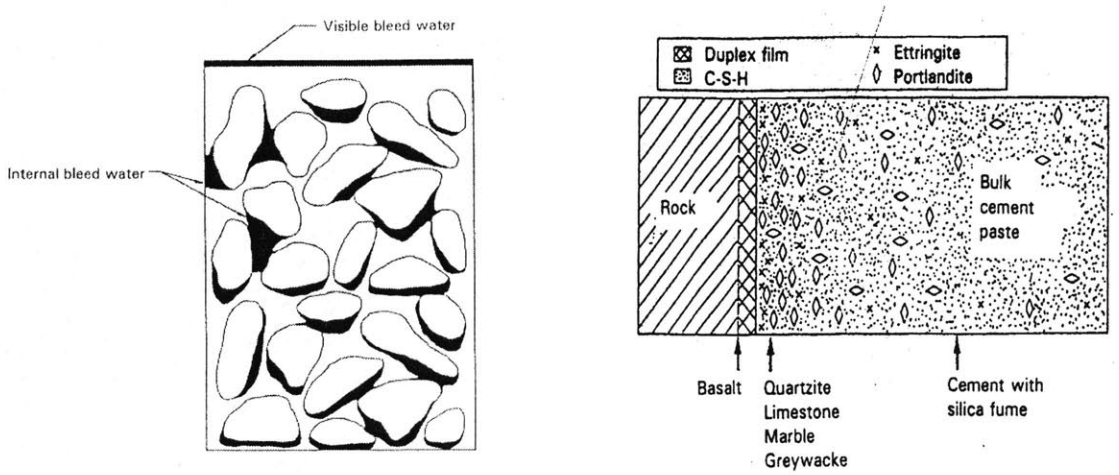

(a) (b)

Figure 2-5: (a) Diagrammatic illustration of bleeding phenomenon. More pronounced effect in large and/or elongated particles [60]. (b) Arrows shoe the debonding zones in systems of different aggregates and binder compositions [87].

2.2 Scales of Observation

In the preceding sections we identified the different phases present in concrete and their structure. It is instructive to separate the different features according to their length scales, and identify the morphological characteristics of the constituents present at the different scales.

2.2.1 Length scales & levels of characterization

Figure 2-6 shows an "organization chart" of the multi-scale structure of concrete going from the meter to the nanometer scale. The upper levels of the chart are generally well accepted and understood. Some ambiguity, however, exists at smaller levels (Level "0" and I) where no direct information is available. This will be discussed first.

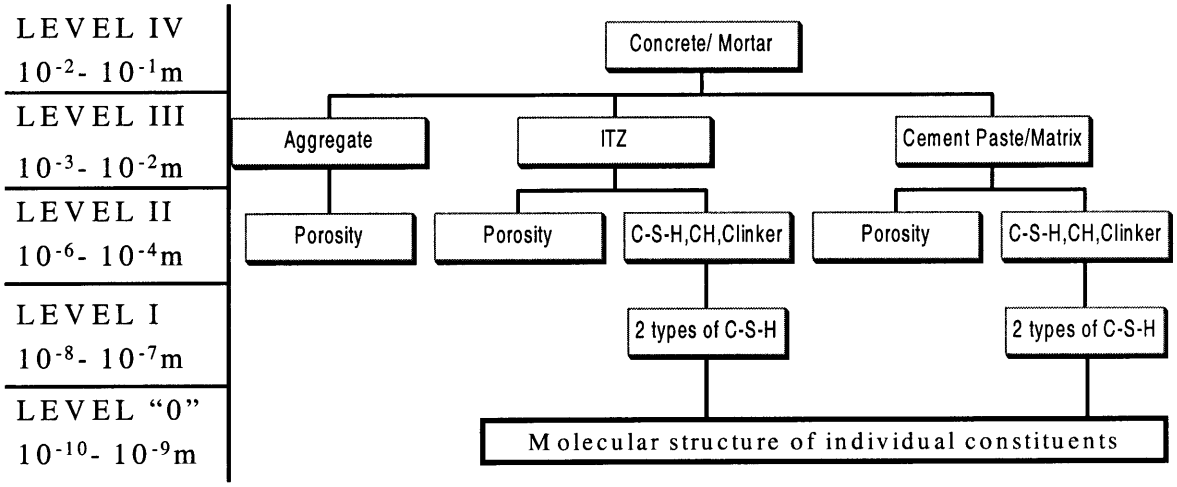

Figure 2-6: Organisation chart of multiscale structure of concrete.

Level "0" ($L = 10^{-10} - 10^{-9}$**m**)

At the nanometer scale, the elementary components of the different constituents are the primary building blocks of the different crystal or amorphous structures of the phases. Chemical structures and morphological characteristics are as described in Section 2.1.1. This is the level, at which the C/S-ratio gives indications about the crystal structure and the length of the silica chains. The porosity present at this level is the interparticle spacing in the structures of the different phases. Data from different researchers suggest that this porosity is constant at 28 % by volume (see Section 2.1.1).

However, to our knowledge, there is no experimental data available on the elastic behavior of the material at this scale, which may well be due to the inability of current experimental techniques to provide information at this fine scale. A simplified theoretical attempt was made by Ashby [6] to find the origins of elastic modulus by considering:

1. The interatomic forces (springs) which link the atoms together in the solid state.

2. The ways in which atoms are packed together.

Cement paste is held together almost entirely by primary bonds (ionic and covalent bonding). However, because of its composite nature, bonds change from phase to phase, i.e. from C-S-H to CH, and along their interfaces. This makes modeling difficult. It is expected that model-based simulations based on molecular dynamics may, in the close future, shed light on the physics at stake at this scale.

Level I ($L = 10^{-8} - 10^{-7}$**m**)

There exists an intermediate length scale because of the tendency of C-S-H to agglomerate and form clusters which are in the range of a few nm to hundreds of nm. Several models were proposed in the open literature throughout the years in an attempt to deduce specific characteristics of the microstructure. Since the structure itself cannot be directly observed research focused on finding *the* hidden underlying structure that is consistent with a variety of observations. We acknowledge the models of Powers and Brownyard [84, p. 33], Feldman and Sereda [33], and Wittman's "Munich model" [101, p. 118]. Feldman and Sereda regard the gel as a three dimensional assemblage of C-S-H layers, which tend to form a subparallel, few layer thick group, and which enclose pores of dimension of the interlayer spaces and upwards. This model is consistent with surface area measurements and sorption isotherm data. It also gives a great deal of information about the state of water and porosity at this scales (see Appendix B). Similarly, the "Munich" model and the "Powers-Brownyard" model present a slightly modified gel structure in the range of 1-100 nm, which is consistent with relative humidity and hydration degree measurements, respectively. But in all these models, C-S-H is treated as a single phase (with some variability), and no distinction between different types of C-S-H is made. Furthermore, none of the models gives insight into the elastic behavior of the material.

Figure 2-7 shows the Powers and Brownyard model in a slightly modified form. Following the original model, immediately after mixing, the unhydrated cement particles in a fresh paste are dispersed in an aqueous solution (Figure 2-7(a)). During the first few minutes, the reaction rate is very rapid, and calcium silicate hydrates form a coating

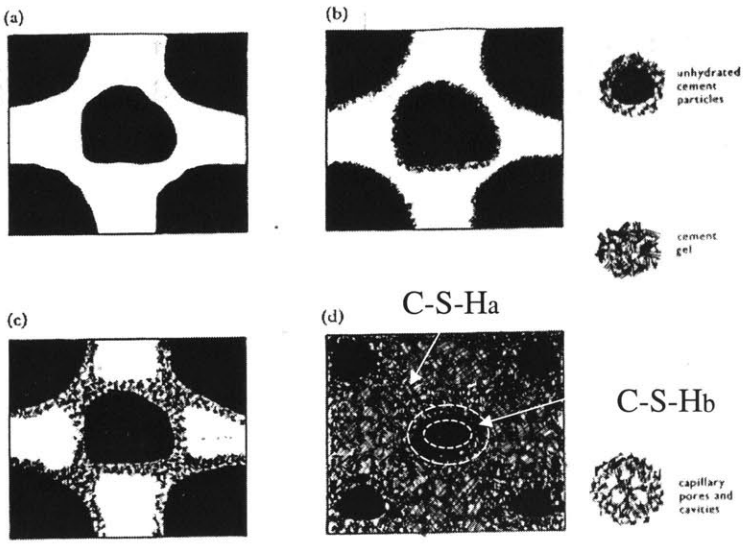

Figure 2-7: Modified Powers and Brownyard Model incorporating two types of C-S-H.

around the cement grains. As hydration proceeds, hydration products including calcium hydroxide, precipitate from the saturated solution in the capillary pores or spaces. The C-S-H formed during this period appears to precipitate in a characteristic pattern with uniform porosity (about 100-1000Å in size). They correspond to the outer product or low density C-S-H (C-S-H_a). Any microcrystalline CH and minor compounds formed during this period is included into the C-S-H_a structure. Since 1 cm^3 of cement produces 2.2 cm^3 of cement gel, about half of the gel forms inside the original boundary of the cement grain, and half is deposited in the surrounding water filled space. Eventually, bridging occurs between cement particles and the paste stiffens into its final shape (see Figure 2-7(b) to 2-7(d)). Further hydration which involves some complex diffusion processes, results in further deposition of cement gel at the expense of unhydrated cement and capillary pore water. C-S-H_b is formed during this period and appears to have a lower porosity and pore size (about 50-500Å). The volumetric proportions of the two types of C-S-H depend on the $w/c-$ratio and probably also on the cement particle size. Recalling that a $w/c-$ratio of 0.38 is enough to cause complete hydration, we note:

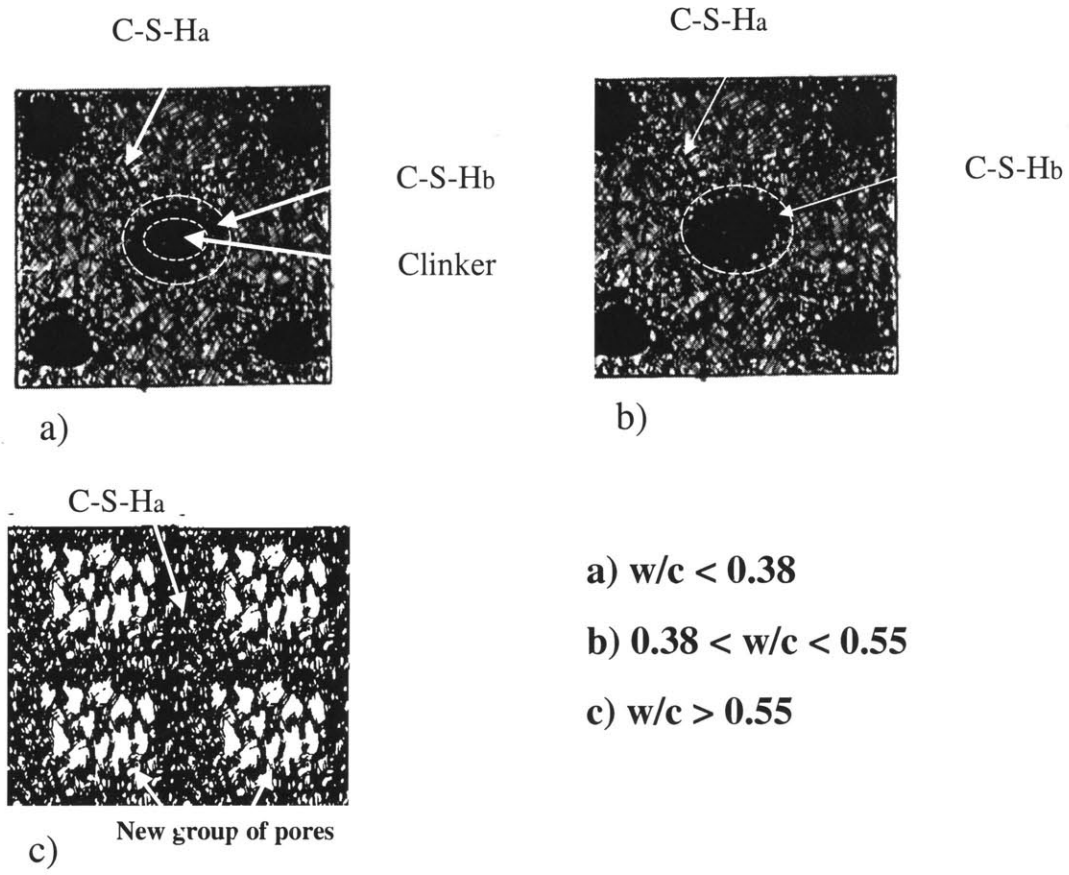

Figure 2-8: Evolution of cement pastes microstructure with increasing $w/c-$ratio.

- For $w/c < 0.38$, both types of C-S-H coexist. In addition to unhydrated cement particles, they form the cement paste at this scale.

- For $0.38 < w/c < 0.55$, cement particles are completely consumed by hydration, the two types of C-S-H are still present, and their relative proportions vary depending on the $w/c-$ratio.

- For $w/c > 0.55$, all C-S-H formed is C-S-H_a due to the large space available for the hydration products to precipitate. In addition, a new group of pores appear, which grow in volumetric proportions and probably in size with increasing $w/c-$ratio. The proposed changes in the cement pastes microstructure with varying $w/c-$ratio are shown in Figure 2-8.

This modified Powers and Brownyard model is consistent with the following observations:

- Figure 2-9 shows a graph of the degree of hydration and surface area measurements with time. The data provided in [61] shows that the surface area curve tends to flatten out during the last stages of hydration, which suggests that this period is intimately related to the formation of a low surface area compound, that is C-S-H_b.

- Measurements of pore size distribution in [9] suggest the presence of a pore group at around 100 nm independently of the $w/c-$ratio. In addition, a new pore group is formed for $w/c > 0.55$ at a scale above.

- Experimental data in [76] present pore size distributions for cement pastes with different $w/c-$ratio replotted after omitting the large pores (> 132 nm) (Figure 2-10). It was found that a single curve could fit the pore size distribution made with four different $w/c-$ratios (all greater than 0.55). This provides strong evidence of a uniform microstructure for all materials. In addition, it shows that the increase in total porosity in hcp resulting from increasing $w/c-$ratios manifests itself in the form of larger pores only (see Figure 2-11). For $w/c-$ratios less than 0.55 the

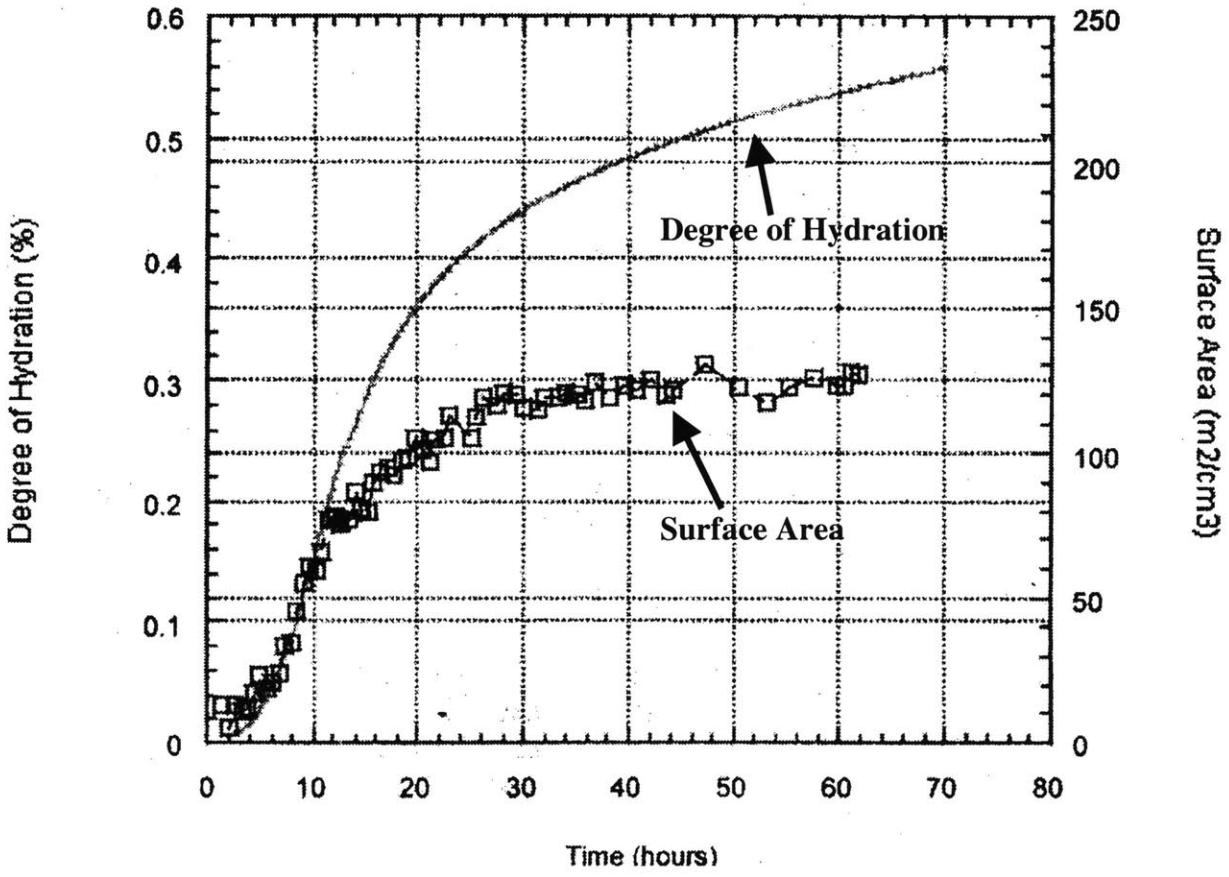

Figure 2-9: Degree of reaction and surface area measurements for a typical cement paste [61].

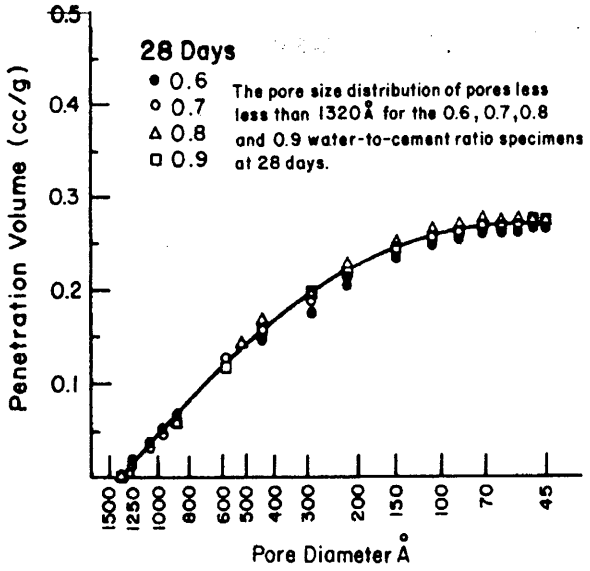

Figure 2-10: Pore size distributions of small pores in cement pastes of varying $w/c-$ratios. Replotted after ommiting the larger pores (>132 nm) [76].

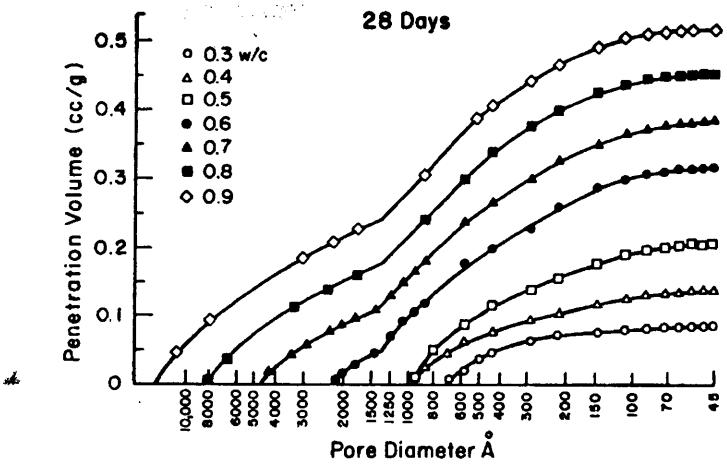

Figure 2-11: Pore size distribution in Hydrated Cement Pastes of different $w/c-$ratios [76].

curve shifts to lower volumes, which is a consequence of the varying volumetric proportions of the two types of C-S-H (see Figure 2-11).

Level II ($L = 10^{-6} - 10^{-4}$**m**)

Level II and above are generally well accepted and understood. Due to the relatively large characteristic length scale of the different inhomogeneities present at that scale, direct visual access is possible by SEM and other microscopy imaging techniques. Consequently, there is a high degree of consistency among the different models proposed in the literature. It is generally agreed that the two types of C-S-H from Level I form a homogeneous matrix that accommodates large Portlandite crystals, as well as the residues of unhydrated cement clinker. Other phases potentially present at this scale, include entrained air incorporated by the use of admixtures (i.e. for freeze-thawing protection), capillary porosity ($> 1\mu$m) present with increasing $w/c-$ratio, and so on. Level II can be considered as representative of the macroscopic mechanical performance of cement pastes.

Level III ($L = 10^{-3} - 10^{-2}$**m**)

At level III, sand particles enter the picture contributing to the heterogeneous nature of this scale. This level can be considered as representative of mortar, which is composed of three phases: a cement paste matrix (formed by the phases of Level II), sand inclusions and surrounding ITZ. Several models have been proposed in the open literature, which consider mortar as a two-phase material [28,59,79], or three phase material [69,83,94,113].

Level IV ($L \triangleq 10^{-2} - 10^{-1}$**m**)

The characteristic length of level IV depends predominantly on the maximum aggregate size. At this level, the material can also be viewed as a three phase material system: a mortar matrix, aggregates including their gradation, and the inclusion–matrix interface. Similarly to level III, each phase can be assumed as a homogeneous phase with distinct

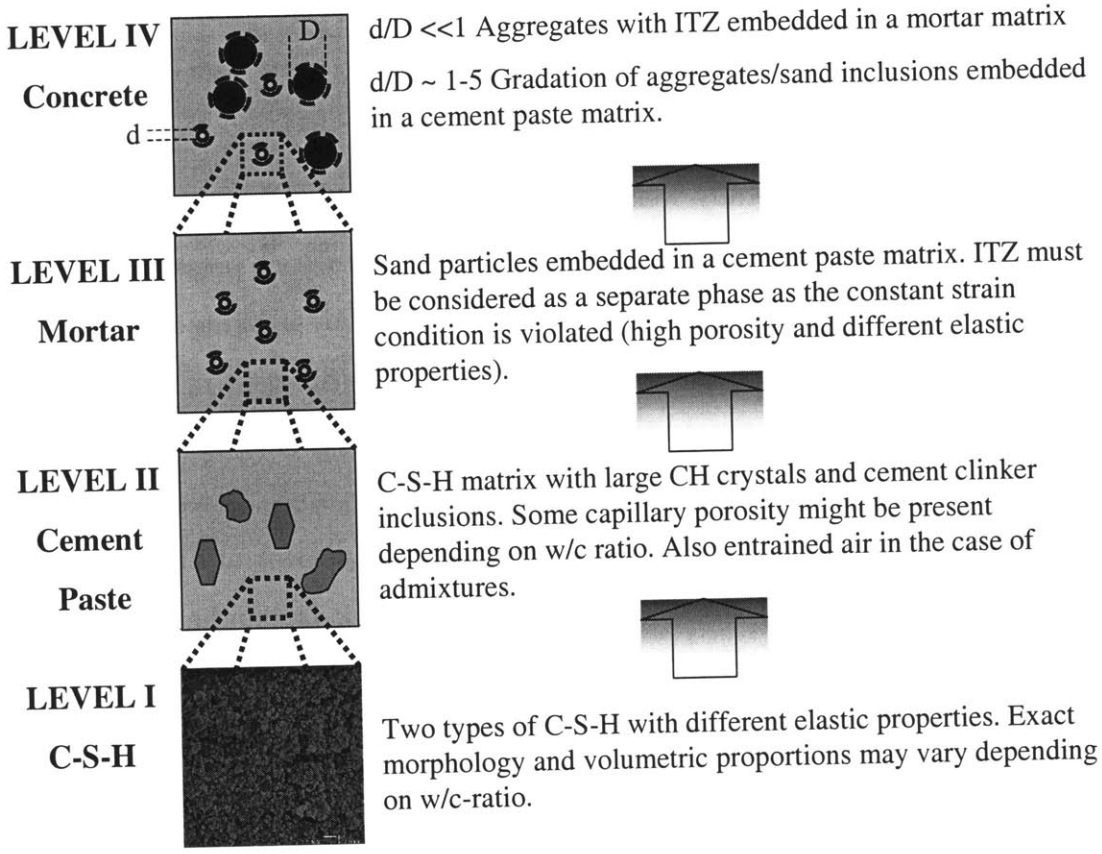

Figure 2-12: Four-level microstructure of cement-based composite materials.

average mechanical properties and volume fractions. The porosity at this scale is assumed to be incorporated into the different phases (level "0", I & II). This level is representative of concrete with coarse aggregates, and the material properties obtained theoretically or experimentally at this scale, are characteristic for laboratory test specimens.

2.3 Concluding Remarks

The categorization of the different concrete constituents in terms of their length scale completes the description of the structure of concrete. Figure 2-12 summarizes, in a schematic way, the multiscale structure of concrete developed in Sections 2.1 and 2.2.

The starting point of this figure is level I which constitutes the smallest material length scale that is , at present, accessible by mechanical testing. The atomic scale, Level "0", is not, at present, clearly understood. Having said that, the elastic behavior of the material can now be studied, by selecting suitable experimental techniques for the different scales, which will allow quantifying the effect of chemical degradation on the elastic stiffness of cement-based composite materials. Macroscopic measurements (Chapter 4), performed on cement paste and mortar, refer to level II and level III, respectively. Nanaoindentation tests concentrate on level I, where the elastic properties of the individual constituents are measured (Chapter 5).

In addition, this four-level microstructure forms the backbone of the "bottom-up" micromechanics approach, and forms the basis for the modeling. It is instructive to note that the four levels satisfy the separation of scale principle, that is, each level is separated from the next one by (at least) one order of magnitude in size of the elementary heterogeneity. This is a prerequisite for the application of micromechanics. Furthermore, from a morphological point of view, all levels are characterized by a matrix–inclusion geometry.

Part I

EXPERIMENTAL INVESTIGATION

Chapter 3

Experimental Program

This part of the thesis presents a detailed account of the experimental approach adopted in this research. The materials tested in our study are presented first. Then the experimental results, which aim at characterizing the effects of calcium leaching induced aging at different scales of cement paste and mortar, are discussed. Emphasis is placed on separating the effects of chemical degradation on the individual constituents. To this end, state-of-the-art material tests were performed at different length scales spanning over 6 orders of magnitude (10^{-7} m to 10^{-2} m). An overview of the experimental program is given in Figure 3-1. The macroscopic effects of calcium leaching, which pertain to length scales on the order of 10^{-4} m to and 10^{-2} m were studied by means of porosity, density, and elastic modulus measurements. The results are presented and discussed in Chapter 4. Chapter 5 is devoted to microscopic measurements referring to length scales on the order of 10^{-7} m to 10^{-4} m, and include SEM investigation and Nanoindentation tests.

3.1 Materials

Cement paste and mortar specimens were prepared using an Ordinary Portland Cement (OPC) Type I (composition provided in Table 3.1) at a water/cement ratio of $w/c = 0.5$. Mortar specimens were prepared at a water/cement/sand ratio of $w/c/s = 1/2/4$,

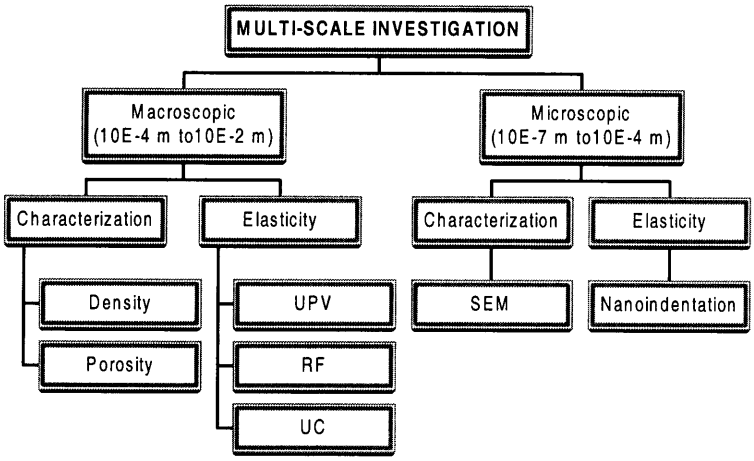

Figure 3-1: Outline of experimental activities, which include macroscopic and microscopic tests.

OPC	CaO	SiO_2	Al_2O_3	MgO	SO_3	Na_2O
TYPE I	62.30	20.80	4.40	3.80	2.90	0.39
	Fe_2O_3	K_2O	C_3Al	C_3S	C_2S	Ignition Loss
	2.40	1.28	8.00	53.00	20.00	0.66

Table 3.1: Composition of Portland Cement Type I in percentage as provided by the manufacturer.

using a fine Nevada sand of density 2650 kg/m^3, $d_{60} = 0.23$ mm[1] and $d_{30} = 0.17$ mm. This composition gives an approximate volume fraction of inclusions of $f_I \simeq 0.5$. The specimens were cast in cylindrical molds with a diameter of 11.5 mm and a length of 60 mm.

[1] d_a denotes the length of the square opening of the sieve for which a percentage a (by weight) of the material passes through (e.g. $d_{60} = 0.23$ mm; 60 % of the weight of the material have a particle size less than 0.23 mm).

3.2 Calcium-Leached Specimen Preparation

3.2.1 Accelerated Calcium Leaching

The tools for modeling the coupled diffusion–dissolution process (calcium leaching) were developed in Section 1.2. Given the slow dissolution-diffusion process, small sample sizes and high calcium efflux favor a rapid leaching process. In the present study, the test program is carried out on pure cement pastes and mortars allowing for small and relatively homogeneous material samples. Moreover, the calcium efflux is artificially accelerated by increasing the chemical equilibrium concentration, i.e. the calcium solubility, at the dissolution front. Leading to a higher calcium concentration gradient in the pore solution, and thus to higher efflux, this is achieved by replacing the deionized water that is part of the reference scenario by an Ammonium nitrate solution (NH_4NO_3). Calculations based on the work of Berner [72] show that the equilibrium calcium concentration is shifted from $\simeq$ 22 mol/m^3 (using deionized water) to $\simeq$ 2900 mol/m^3 in a 6M NH_4NO_3 (480 g/kg) solution (see Figure 1-3(b)). The accelerated test described here below is based on the work of Heukamp et. al. [55].

Portlandite is the first mineral to be leached, the C-S-H decalcify thereafter [4]. The dissolution of Portlandite ($Ca(OH)_2$) in the Ammonium nitrate solution can be written according to the following reaction equation:

$$\begin{cases} Ca(OH)_2 + 2NH_4NO_3 \rightleftharpoons Ca^{2+} + 2OH^- + 2H^+ + 2NH_3 + 2NO_3^- \\ \rightleftharpoons Ca(NO_3)_2 + 2NH_{3g} + 2H_2O \end{cases} \tag{3.1}$$

The high solubility of ammonium nitrate (680g/kg of solution at 20°C), the change to the gaseous phase of NH_3 and the high solubility of calcium nitrate favor the dissolution process. An equilibrium exists between the ammonium (NH_4) and the aqueous ammonia (NH_{3aq}):

$$NH_4^+ \rightleftharpoons NH_{3aq} + H^+; \qquad \frac{[NH_{3aq}][H^+]}{[NH_4^+]} = 10^{-pK_a} \tag{3.2}$$

where $[NH_{3aq}]$, $[H^+]$ and $[NH_4^+]$ are the activities of the different species. The pH at which the equilibrium concentration of ammonium equals that of ammonia (NH_3), is equal to the pK_a of NH_4^+, 9.25. Hence, for a pH smaller than 9.25, there is always more ammonium than ammonia in solution. During the leaching process, the ammonium in the pore solution of the cementitious material dissociates to ammonia and H^+ (Eq. (3.2)), due to the basic environment. H^+ reacts with OH^-, reducing the OH^- activity, and favoring the dissolution of $Ca(OH)_2$. Together with the change to the gaseous phase of NH_3 and the high solubility of calcium nitrate, this qualitatively explains the high calcium equilibrium concentration of $\simeq 2900$ mol/m^3 in a 6M NH_4NO_3 solution, which *in fine* is the key to an accelerated leaching process. By contrast, for pH > 9.25, the lack of ammonium reduces the calcium equilibrium concentration, and thus the overall leaching process. This is why it is important to monitor the pH of the aggressive solution during the accelerated leaching experiment. This accelerated leaching has the same characteristics as "natural" leaching:

- The dissolution that occurs at a higher equilibrium concentration is still quasi-instantaneous in comparison with the diffusion of calcium ions from the dissolution front to the outside; and thus the leaching process is still governed by the diffusion properties of the material.
- Albeit different in kinetics, the ammonium nitrate based calcium leaching leads to the same mineral end products in the cementitious material [25].

As a quasi-self similar diffusion-dissolution problem, the overall acceleration rate can be assessed from the ratio of the similarity parameter of front propagation:

$$a = \left(\frac{\xi_{d1}}{\xi_{d0}}\right)^2 \tag{3.3}$$

where $\xi_{d0} = x_d/\sqrt{t_0}$ and $\xi_{d1} = x_d/\sqrt{t_1}$ are close to a multiplied constant the self-similar parameters that define the position x_d of the dissolution front in the normal and accelerated leaching setting, respectively. For the derivation, see Section 1.2.

Finally, it should be mentioned that the maximum solubility of Ammonium nitrate in water (680g/kg) shows that more than 6M Ammonium nitrate can be dissolved in water. The calcium equilibrium concentration in principle increases with the Ammonium nitrate concentration. However, adding Ammonium nitrate beyond 6M does not accelerate the leaching process, due to the limited amount of Portlandite in the cement paste.

3.2.2 MIT's Accelerated Aging Test

The experimental procedure adopted in this research is summarized in Figure 3-2. Cement paste and mortar are mixed and cast in cylindrical moulds. After 24 hours, the specimens are demolded and cured in a saturated lime solution for 27 days at 20°C. One half of the samples are immersed in the 6M ammonium nitrate solution for accelerated leaching; the other half are stored for control purposes in limewater. To obtain good mixing of the ammonium nitrate solution and most homogeneous leaching conditions possible, the tanks containing the ammonium nitrate bath are mounted on a slowly oscillating table, as shown in Figure 3-3. In that way, the bath is constantly agitated and the sample surfaces are in free contact with the aggressive solution. Each tank of 15×15 cm quadratic shape is filled with 2.2 kg of aggressive solution and contained 26 specimens. In addition, carbonation by CO_2 was prevented through replacing the air in the tanks by pure nitrogen gas (Figure 3-3). In parallel, the pH of the solution is monitored. A necessary renewal of the solution due to a lack of Ammonium (NH_4^+) would have been indicated by a pH greater than 9.25, see Eqs. (3.1) and (3.2). At the chosen combination of ammonium nitrate concentration, bath volume and number of specimens, it turns out that the aggressive solution must not be renewed during the leaching experiment; the leaching process continuously takes place at the highest possible rate. During the leaching process, samples are taken out of the aggressive bath to determine visually the progress of the dissolution front. A square root of time function for the dissolution front progress was obtained being of the order of $\xi_{d1} = 2$ mm/$\sqrt{\text{day}}$. If we take for reference the "natural" progress of the propagation front of $\xi_{d0} = 0.115$ mm/$\sqrt{\text{day}}$ (see e.g. [4]),

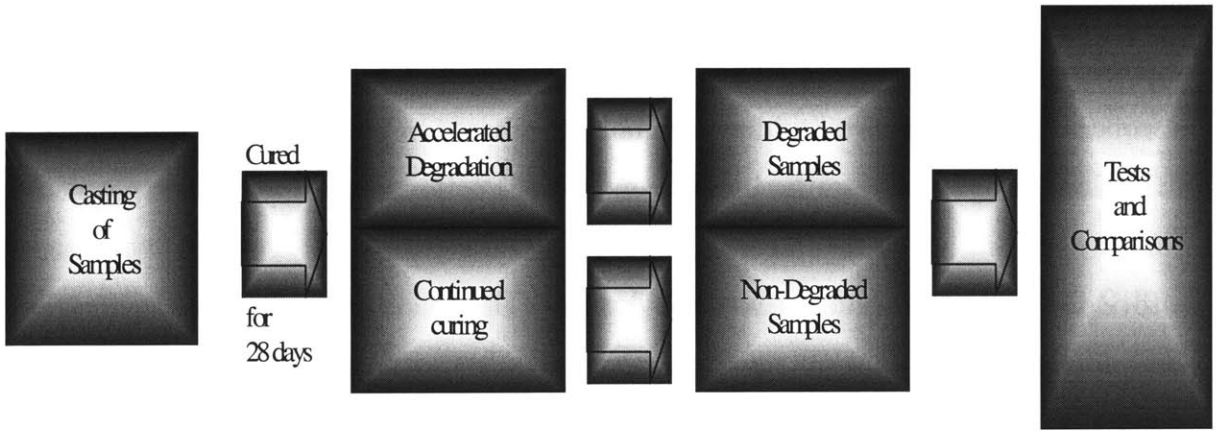

Figure 3-2: Procedure of Experimental Activities

we obtain with the 6M ammonium nitrate solution (480 g/kg of solution), an overall acceleration of $a = 300$ according to Eq. (3.3). For the 11.5 mm in diameter cylinder samples, the dissolution front reaches the center of the specimens in less than 9 days. However XRF analysis show that the average bulk calcium content is still decreasing significantly thereafter (Figure 3-4). The quasi steady state, i.e. homogeneous calcium content, requires 45 days of accelerated leaching.

At the age of 5 months specimens from both batches are tested and compared. Specimens are kept in water at all times to avoid microcracking development. The experimental data reported hereafter refer to these saturated samples.

Figure 3-3: Oscillating table for controlled calcium leaching [107].

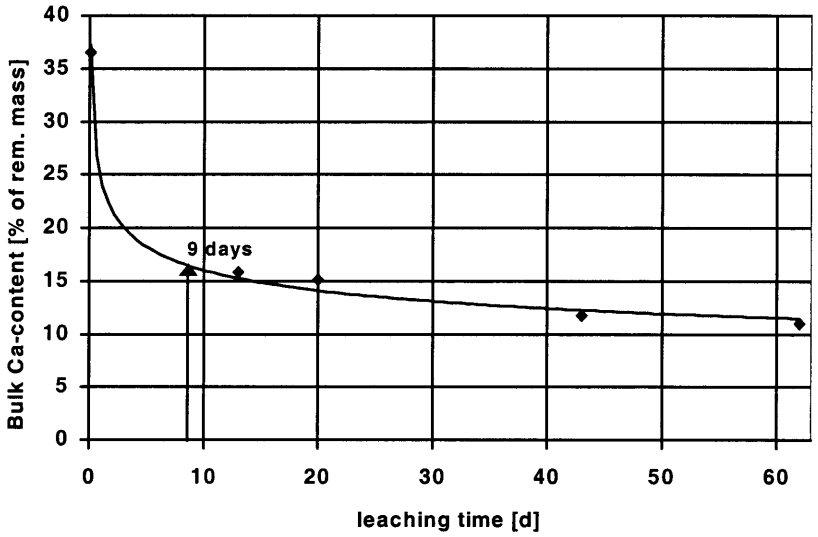

Figure 3-4: Bulk calcium content evolution during leaching [107].

Chapter 4

Macroscopic Measurements

The macroscopic elastic modulus of the different cement paste and mortar samples are measured using 3 different experimental techniques:

- Ultrasonic Pulse Velocity (UPV)-Pulse Modulus
- Resonant Frequency (RF)-Dynamic Modulus
- Uniaxial Compression (UC)-Static Modulus

The first two fall in the category of Dynamic or Vibration methods. These two methods are non-destructive and they provide the "true" elastic modulus of the material, since no mechanical degradation is involved during testing. Two different tests were used in order to ensure the good quality of the results. In addition, the uniaxial compression test was considered as a third complementary method to determine the elastic and elasto-inelastic material properties. The used test apparatus is capable of constantly monitoring the force-displacement behavior of the specimen during the test. Knowledge of the initial specimen dimensions allows the determination of the complete stress-strain curve.

Sample	Cement Paste		Mortar	
	Non-Degraded	Degraded	Non-Degraded	Degraded
Porosity (%)	39.7 ± 1.1	63.2 ± 1.6	27.5 ± 0.4	40.1 ± 2.4
Density$_{(sat.)}$ (kg/m^3)	1898 ± 9	1351 ± 12	2171 ± 15	1831 ± 19

Table 4.1: Porosity and density measurements on degraded and non-degraded cement paste and mortar samples (Mean/St. Dev.).

4.1 Supporting tests

In order to quantify the degree of degradation on the physical properties caused by the depletion of calcium bound in the skeleton of cement paste, porosity and density measurements were performed on all specimens. The results are summarized in Table 4.1. A detailed description of the porosity and density measurements is given in Appendix A. Apart from characterizing the effect of degradation, density measurements provide the input parameter for the determination of the elastic modulus from Ultrasonic Pulse Velocity and Resonant Frequency techniques.

Degraded samples show an average increase in porosity of 24% by volume of cement paste in both cement pastes and mortars. Density values are also significantly affected by this increase in porosity. This effect is less pronounced for mortar due to the presence of the chemically inert sand-filler.

4.2 Non-Destructive techniques

The theoretical principles of the two non-destructive techniques employed in this study are based on the work of Rayleigh [91], i.e. the mathematical relationships between the velocity of sound through a specimen and its resonant frequency, and the relationship between velocity and natural frequency and the elastic modulus of the material. To appreciate this method, we briefly recall the fundamental equations.

Let the displacement vector at a point x_j and time t be denoted by $u_i(x_i, t)$. Neglecting body forces (such as gravity), the dynamic resultant theorem of a unit volume reads:

$$\rho \frac{\partial^2 u_i}{\partial t^2} = \frac{\partial \sigma_{ij}}{\partial x_j} \tag{4.1}$$

where σ_{ij} is the stress tensor. The linear elastic isotropic equation of state reads:

$$\sigma_{ij} = \lambda \varepsilon_{kk} \delta_{ij} + 2\mu \varepsilon_{ij} \tag{4.2}$$

where λ and μ are Lamé constants and $\varepsilon_{ij} = \frac{1}{2}(u_{i,j} + u_{j,i})$ is the strain tensor. Substituting (4.2) into (4.1), we obtain:

$$\rho \frac{\partial^2 u_i}{\partial t^2} = (\lambda + \mu) \frac{\partial^2 u_i}{\partial x_i x_j} + \mu \nabla^2 u_i \tag{4.3}$$

Taking the divergence[1] of (4.3) yields:

$$\rho \frac{\partial^2}{\partial t^2} \left(\frac{\partial u_i}{\partial x_i} \right) = (\lambda + 2\mu) \nabla^2 \left(\frac{\partial u_i}{\partial x_i} \right) \tag{4.4}$$

where $\frac{\partial u_i}{\partial x_i} = \varepsilon_{ii} =$ relative volume variation. The previous equation can be recast in the form:

$$\frac{\partial^2}{\partial t^2} (\varepsilon_{ii}) = C_L^2 \nabla^2 \varepsilon_{ii} \tag{4.5}$$

where C_L is the wave speed:

$$C_L = \sqrt{\frac{\lambda + 2\mu}{\rho}} = \sqrt{\frac{E(1+\nu)}{\rho(1+\nu)(1-2\nu)}} \tag{4.6}$$

E is the Young's modulus, and ν is the Poisson's ratio. Eq. (4.5) refers to a longitudinal wave of speed C_L hence the subscript L.

Consider now a thin rod of length (**L**) vibrating in flexure. It can be shown, according to the relationships established by Rayleigh [91], that the natural frequency n, the velocity of sound V, and a factor depending on the cross section of the specimens ($A = \frac{km^2}{2\pi}$ with k radius of gyration of the section about an axis perpendicular to the plane of bending

[1] Recall that div $(\cdot)$ =tr.(grad$(\cdot)$)

and $m = 4.73$ for the fundamental mode of vibration) are linked by:

$$n = \frac{kV}{2\pi L^2} m^2; V = \sqrt{\frac{E}{\rho}} \tag{4.7}$$

Eliminating V from Eq. (4.7) and solving for E, yields:

$$E = A \times n^2 \times \mathbf{L}^2 \times \rho \tag{4.8}$$

The assumptions made in this derivation is that the material is linear, isotropic, homogeneous, and perfectly elastic in nature. However, as stated by Malhorta [73]: "these relationships can be applied to heterogeneous systems such as concrete when the dimensions of the specimens are large in relation to the size of the constituents of the material."

Eqs. (4.6) and (4.8) establish the basis for measuring the elastic modulus by (1) determining the resonant frequency of a specimen (Resonant Frequency test), and (2) recording the time of travel of short pulses of vibration passing through the sample (Ultrasonic Pulse Velocity test). These two methods require as input parameter to the equations the density of the material. In addition, Ultrasonic Pulse Velocity technique requires knowledge of the Poisson's ratio of the material. Density measurements were performed on all specimens and the corresponding values from Table 4.1 are used. In return, values for Poisson's ratio were taken from the open literature. Results presented in [12] suggest that the macroscopic Poisson's ratio remains unaffected by the degradation process; In this study, constant value of $\nu = 0.24$ was applied.

4.2.1 Ultrasonic Pulse Velocity Test

Experiments were performed using high precision equipment (Figure 4-1) of the Non-Destructive Evaluation Laboratory in the Department of Civil and Environmental Engineering at MIT. ASTM C 597-83 (Reapproved 1991) [2] and BS 1881:Part203 [100] provide a detailed description of the Ultrasonic Pulse Velocity technique. This long established non-destructive method determines the velocity of longitudinal (compressional)

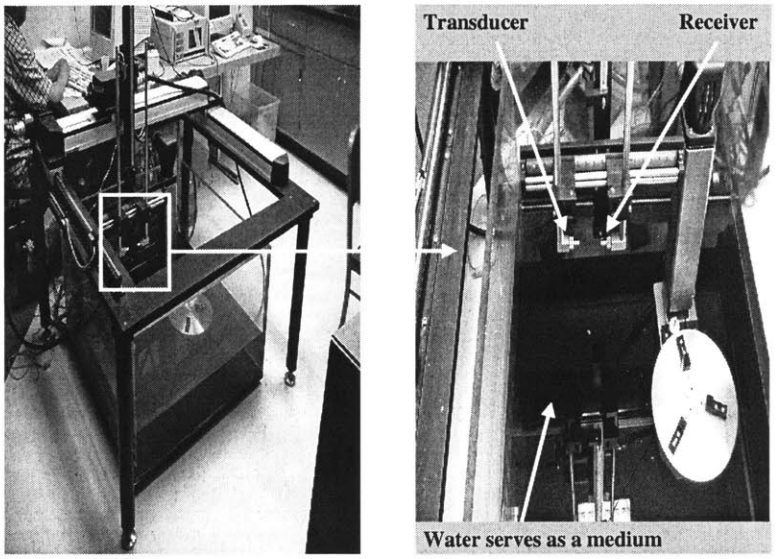

Figure 4-1: Apparatus used for Ultrasonic Pulse Velocity (UPV) measurements.

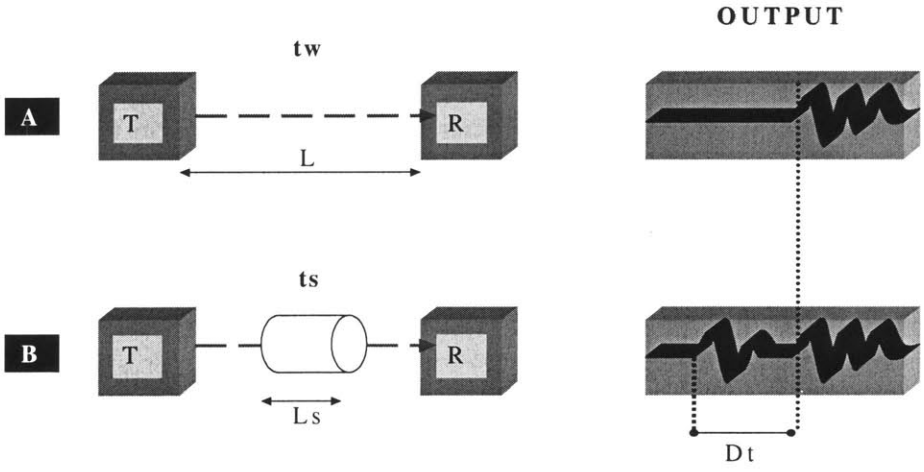

Figure 4-2: Ultrasonic pulse velocity tests: Two types of measurements are required to calculate the velocity of ultrasound through the cementitious specimen.

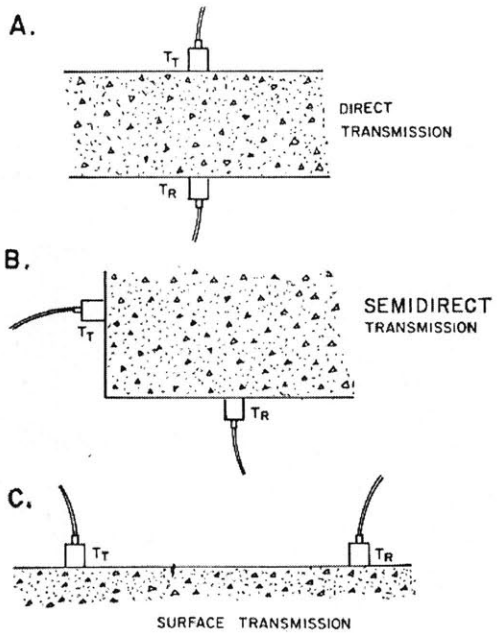

Figure 4-3: Methods of measuring pulse velocity through concrete. A. Direct transmission method. B. Semidirect transmission method. C. Surface transmission method [19].

waves in a medium by measuring the time taken by the wave to travel a certain distance. The experimental set-up, illustrated in Figure 4-2, is a modification of the direct transmission method (see Figure 4.3). The apparatus generates a pulse of vibration at an ultrasonic frequency, which is transmitted by an electroacoustic transducer (T) to the concrete specimen through a water medium. Since the fluid does (almost) not transmit shear, only longitudinal waves are transferred to the specimen. Nevertheless, there are always some shear and surface waves. These waves, however, do not cause much interference, because the longitudinal waves travel at a much faster speed[2]. Consequently,

[2]Taking the curl of Eq. (4.3) and denoting by $\vec{\varpi}$ the rotation vector as $\vec{\varpi} = \nabla \times \mathbf{u}$, we obtain the governing equation of the rotation alone: $\frac{\partial^2 \vec{\varpi}}{\partial t^2} = C_T^2 \nabla^2 \vec{\varpi}$, where $C_T = \sqrt{\frac{\mu}{\rho}} = \sqrt{\frac{E}{2\rho(1+\nu)}}$. Thus,

$$\frac{C_L}{C_T} = \sqrt{\frac{\lambda + \mu}{\lambda}} > 1$$

since $\frac{\mu}{\lambda} = \frac{1}{2\nu} - 1 \geq 0$. Similarly, it can be shown that surface waves travel at a much slower speed than both longitudinal and transverse waves [91].

the exact time of arrival of the longitudinal wave can be picked up easily. After passing through the specimen, the vibrations are received and converted to an electrical signal by a second electroacoustic transducer which serves as a receiver (R). Once the signal is fed through an amplifier to a cathode-ray oscilloscope, the time of the pulse to travel the distance between the two transducers is measured with an accuracy of $\pm$ 0.01μs. With the knowledge of the length of the specimen, and assuming a value for the Poisson's ratio, the elastic modulus is calculated. The water medium limits the error introduced by imperfect transducer-specimen contact. The presence of water medium, however, requires two experimental set-ups and measurements (Figure 4-2) in order to isolate the velocity of sound through concrete. In setup A, the time taken for the wave to travel through water (t_w) at a distance L (distance between transducer (T) and receiver (R)) is measured and the velocity of wave through water (C_w) is obtained from:

$$t_w = \frac{L}{C_w} \tag{4.9}$$

C_w was found to be equal to 1480 m/s at a temperature of 25°C. In setup B, the specimen is introduced in the travel path of the wave, and the time t_s taken for the wave to travel (through the sample and water) is now:

$$t_s = \frac{L - L_s}{C_w} + \frac{L_s}{C_L} = t_w - \frac{L_s}{C_w} + \frac{L_s}{C_L} \tag{4.10}$$

where C_L = velocity of wave through the specimen. The time taken for the wave to travel through the sample is $\Delta t = t_s - t_w$. Then, using Eq. (4.9) in Eq. (4.10) we obtain:

$$C_L = \frac{L_s C_w}{L_s - \Delta t \times C_w} \tag{4.11}$$

Eq. (4.11) gives access to the velocity of the pulse C_L in the concrete specimen by measuring the time delay Δt caused by the introduction of the concrete specimen in the line of pulse traveling. This time delay, Δt, is recorded by measuring the time shift between the two waves obtained in the two experimental set-ups (Figure 4-2). Finally

the elastic modulus is obtained from Eq. (4.6):

$$E = \frac{C_L^2 \rho (1+\nu)(1-2\nu)}{(1-\nu)} \tag{4.12}$$

The results obtained on cement paste and mortar specimens are summarized in Tables 4.2 and 4.3, respectively

Parameter Study

This section is devoted to a sensitivity study of parameters that could be a potential source of error in our experimental procedure. Several introductory tests were performed and the sensitivity of elastic modulus on these parameters is examined. The following parameters are studied:

- *Repeatability of the results:* Measurements on the first three samples were repeated 5 times. The values were almost identical with the deviation from the mean being less than 1 %, demonstrating the good repeatability of the test procedure.

- *Support conditions*: A comprehensive literature review [19] suggests that the supporting conditions of the specimen in test may become critical. Several support conditions were considered in our experiments and no effect was observed. The outcome of our experiments may be attributed to the high frequencies (small wave lengths), which result in very small vibrations of the specimen. In addition, the absence of direct contact of the transducers with the specimen eliminate shear and surface wave contribution.

- *Specimen size*: Variations in velocity measurements due to path length has been reported in the literature [19, 109]. To investigate this effect different specimen lengths were cut and tested. A graph of measured velocity versus specimen length for two different frequencies is shown in Figure 4-4. Variations of $\pm$ 1.5 % for the non-degraded and $\pm$ 3 % for the degraded samples are observed. These variations

Cement Paste								
No	**Frequency**	**Degraded**	**Length**	Δt	C_L	E	**Average E**	**St. Dev.**
	(MHz)	**(Yes/No)**	**(mm)**	**(ms)**	**(m/s)**	**(GPa)**	**(GPa)**	**(GPa)**
1	0.5	YES	51.10	5.66	1770.2	3.81		
2	0.5	YES	51.05	5.66	1770.5	3.81	**3.81**	**0.00**
3	1	NO	51.15	21.00	3771.9	22.91		
4	1	NO	50.94	20.80	3740.4	22.53		
5	1	NO	29.20	11.92	3738.9	22.51		
6	1	NO	17.78	7.40	3853.9	23.92		
7	1	NO	34.92	13.88	3594.6	20.81		
8	1	NO	12.17	4.96	3729.7	22.40	**22.51**	**1.00**
9	1	YES	51.15	8.40	1955.2	4.38		
10	1	YES	51.18	8.40	1954.8	4.38		
11	1	YES	51.10	8.30	1948.4	4.35		
12	1	YES	51.05	8.50	1964.0	4.42		
13	1	YES	54.45	7.13	1835.8	3.86		
14	1	YES	54.55	7.60	1864.4	3.98		
15	1	YES	54.60	8.00	1889.8	4.09	**4.21**	**0.23**
16	5	NO	51.15	21.00	3771.9	22.91		
17	5	NO	50.94	20.62	3691.6	21.94		
18	5	NO	29.20	12.00	3777.6	22.98		
19	5	NO	17.78	7.36	3820.8	23.51		
20	5	NO	34.92	14.30	3757.0	22.73		
21	5	NO	12.17	5.06	3847.6	23.84	**22.80**	**0.69**
22	5	YES	51.15	5.68	1771.1	3.60		
23	5	YES	51.18	5.54	1762.3	3.56		
24	5	YES	51.10	5.92	1786.3	3.66		
25	5	YES	51.05	5.82	1780.4	3.63		
26	5	YES	54.45	4.36	1679.0	3.23		
27	5	YES	54.55	3.64	1642.2	3.09		
28	5	YES	54.60	4.40	1680.4	3.24	**3.43**	**0.23**

Table 4.2: Ultrasonic velocity measurements with different frequencies for cement paste samples. The elastic modulus, E, is calculated assuming a Poisson's ratio of 0.24.

Mortar								
No	**Frequency**	**Degraded**	**Length**	Δt	C_L	E	**Average E**	**St. Dev.**
	(MHz)	**(Yes/No)**	**(mm)**	**(ms)**	**(m/s)**	**(GPa)**	**(GPa)**	**(GPa)**
1	1	NO	54.71	22.90	3889.5	24.36		
2	1	NO	54.80	22.90	3879.1	24.23		
3	1	NO	54.90	23.04	3906.2	24.57		
4	1	NO	16.11	7.14	4301.6	29.80		
5	1	NO	17.60	7.78	4280.3	29.50	**26.49**	**2.89**
6	1	YES	16.30	2.12	1832.8	5.22		
7	1	YES	12.35	1.64	1842.0	5.27		
8	1	YES	17.10	2.32	1851.8	5.33		
9	1	YES	14.53	1.97	1851.5	5.33	**5.29**	**0.05**
10	5	YES	16.30	2.18	1845.2	5.29		
11	5	YES	12.35	1.82	1892.8	5.57		
12	5	YES	17.10	2.20	1828.1	5.19		
13	5	YES	14.53	2.04	1868.2	5.42	**5.37**	**0.16**

Table 4.3: Ultrasonic velocity measurements with different frequencies for mortar samples. The elastic modulus, E, is calculated assuming a Poisson's ratio of 0.24.

result in elastic modulus variations of $\pm$ 0.5 GPa (2 %) for the non-degraded samples and $\pm$ 0.5 GPa (9 %) for the degraded ones. The increase of error is due to the proportionality of the elastic modulus to the square of velocity. The scatter of the data suggests that there is no specific relationship between specimen size and velocity of ultrasound. However, some downward trend on velocity with increasing specimen size can be observed in the case of tests made with frequency of 5 MHz (see Figure 4-4). The little influence of the path length on our velocity measurements suggests that our specimens have a relatively high degree of uniformity. Higher values of scattering for the degraded samples could be attributed to the increased inhomogeneity resulted to the high porosity generated by the degradation process. From Figure 4-4 it becomes apparent that the scatter of the data decreases with increasing specimen size. Therefore, for further analysis, only the measurements performed on the longest samples are considered.

- *Frequency:* Figure 4-5 shows the effect of frequency on the velocity of the wave

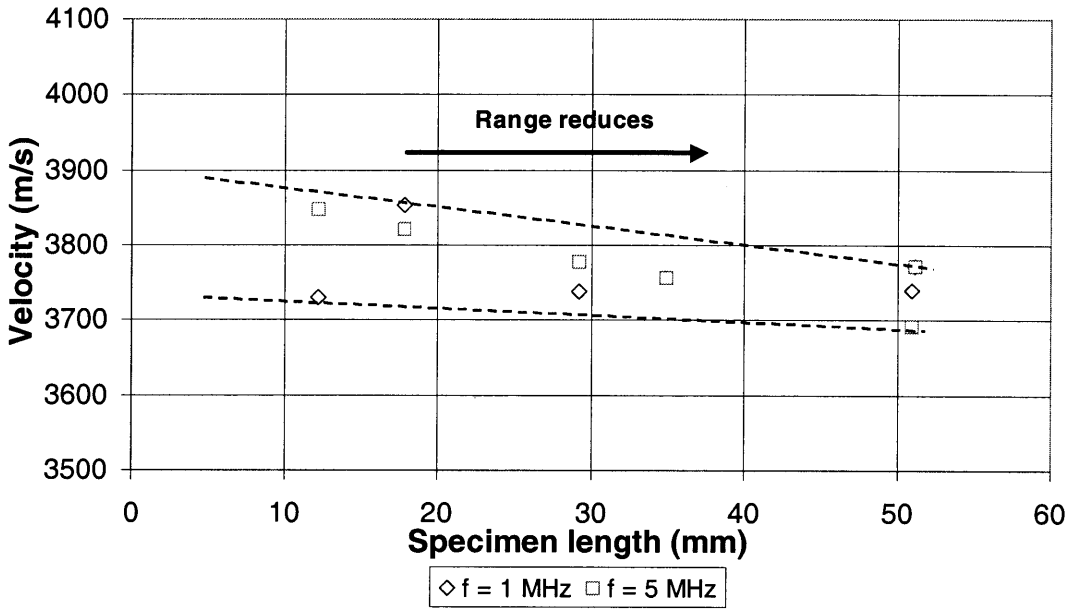

Figure 4-4: Effect of specimen size on Ultrasonic Pulse Velocity measurements. Two different frequencies (f) are used. The results were obtained on non-degraded cement paste specimens.

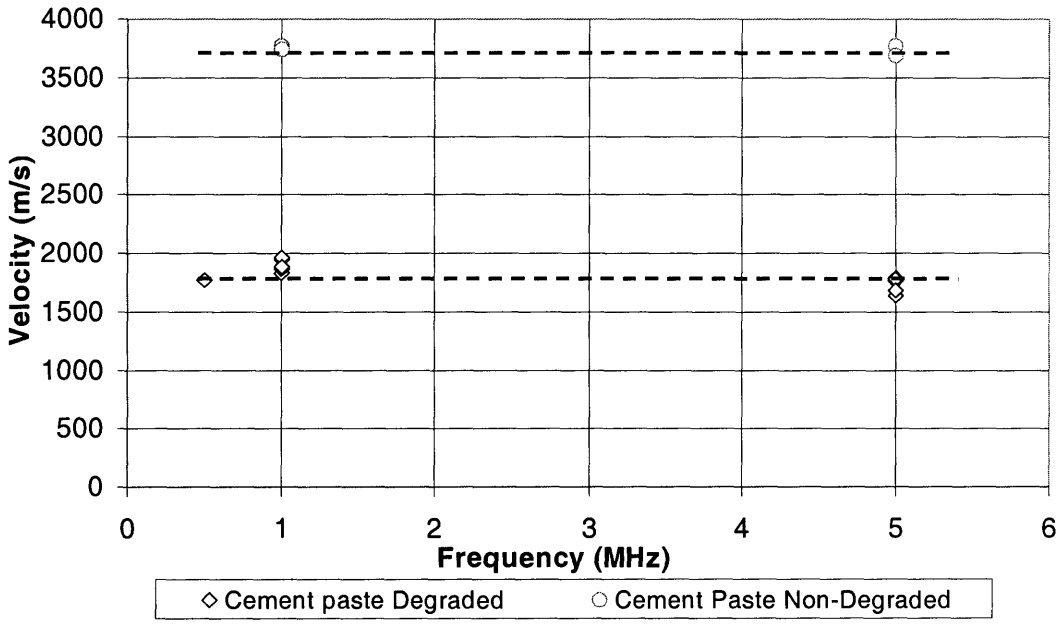

Figure 4-5: Effect of frequency on UPV measurements. No significant effect for both non-degraded and degraded cement paste is found.

through the medium. The variations observed in the case of non-degraded materials were insignificant, while in the case of degraded samples variations are on the order of $\pm$ 1.5 %. This may be attributed to the increased porosity and the imperfect pattern of the microstructure. However, the accuracy of the results is high enough to describe the degraded mechanical behavior.

- *Wave length (λ)*: Eq. (4.12) can be applied to heterogeneous systems such as concrete when the dimensions of the specimens (e.g. length- **L**) is large compared to the wave length (λ). Similarly, the wave length must be considerably larger than the size d of the elementary constituents of the material (characteristic dimension of heterogeneity):

$$d \ll \lambda \ll \mathbf{L} \tag{4.13}$$

Wave lengths (λ) are calculated using the fundamental wave equation:

$$\lambda = \frac{C_L}{N} \tag{4.14}$$

where C_L is the wave velocity. Table 4.4 gives the value for the average wave length of the various used frequencies, N, for both cement paste and mortar. Applied frequencies varied in the range of $0.1 - 5$ MHz giving approximate wave lengths on the order of $300 - 900$ μm. These wave lengths are large enough not to detect the elementary heterogeneities of the material; and they are smaller to avoid any surface interactions. These wave lengths satisfy the principle of separation of scales, expressed by Eq. (4.13), thus ensuring the good quality of the experimental data.

		Average Wave Length - λ (μm)
Cement Paste	**Degraded**	354
Cement Paste	**Non-Degraded**	740
Mortar	**Degraded**	360
Mortar	**Non-Degraded**	840

Table 4.4: Average wave length for the different frequencies used.

- *Ambient Temperature:* It has been reported that variations of the ambient temperature in the range of $4 - 27$ °C do not significantly affect the pulse velocity of concrete [63]. In our experiments the temperature was monitored throughout the test by measuring the temperature of the water medium. The temperature was at all times 15 °C with fluctuations limited to $\pm$ 0.5 °C.

- *Moisture conditions*: In general, the pulse velocity increases with increased moisture content. It is reported that pulse velocity increases by approximately 2 % when dry concrete is saturated [63]. In our case, measurements were carried out on saturated samples, and relative comparison can be made ignoring this effect.

- *Poisson's ratio*: Values of Poisson's ratio are generally not accurately known. However a change in Poisson's ratio over the full range of possible/reasonable values for concrete (that is from 0.18 to 0.25), reduces the computed value of the elastic modulus by only about 7 percent [84, p. 618]. A value of 0.24 was used in our determination. Le Bellego in her work [12] reported that the value of the Poisson's ratio remained unaffected by chemical degradation.

In order to eliminate the effect of frequency and specimen size on the ultrasonic velocity, and consequently on the modulus of elasticity, the measurements using 1 MHz frequency on the longest samples (50mm) were used for further comparisons. An interesting observation pertain to the high attenuation of the ultrasonic wave in the degraded material. Degraded samples of 15 mm were sufficient to attenuate the entire signal, suggesting that such a technique will be quite energy consuming if applied for non-destructive monitoring of structures.

4.2.2 Resonant Frequency test

The Resonant Frequency test is almost exclusively used for laboratory measurements. It involves the determination of the natural frequency of vibrations of a specimen. It can be performed on small samples, and it provides excellent means of studying the deterioration

of concrete [60]. The vibrations can be applied in a longitudinal, flexural or torsional mode. In our experiments, which were performed using high precision equipment of the Non-Destructive Evaluation Laboratory of W.R. Grace, the longitudinal mode was used. A metal sphere hitting on the edge of the specimen vibrates the sample, and a digital machine displays the natural frequency measured by a receiver in contact with the other side of the specimen. The exact test method is described in ASTM C 215-91 [7] and BS 1881: Part 209:1990 [1].

It was reported that E measurements depend on the specimen geometry [109], expressed by the shape factor A in Eq. (4.8). In order to avoid any error induced by the shape factor, all our measurements were compared with an aluminum control specimen of known elasticity (68.95 GPa) and density (2699 kg/m^3), and the same geometry as the cementitious specimens. Eliminating the shape factor from (4.8), the elastic modulus is determined from:

$$(E)_c = (E)_{al} \times \left(\frac{n_c}{n_{al}}\right)^2 \times \left(\frac{\mathbf{L}_c}{\mathbf{L}_{al}}\right)^2 \times \left(\frac{\rho_c}{\rho_{al}}\right) \tag{4.15}$$

where subscript c and al indicate cementitious and aluminum specimen, respectively. n is the natural frequency, $\mathbf{L}$ the specimen length, and ρ the density. The natural frequency and and length of the samples are show in Table 4.5. The resonant frequency results of the tests are summarized in Tables 4.6 and 4.7.

4.2.3 Discussion of Parameters Affecting the Results

- *Reproducibility of results*: Jones [62] reported that the reproducibility of elastic modulus results of resonant frequency is high compared to the static and other test methods. Jones argues that the greater variability in static tests is due to the errors introduced in testing rather than the variability of the specimens. On the other hand, resonant frequency tests depend in essence on length and density, which can be made with a high degree of accuracy. In addition, resonant frequency tests do

Aluminium Samples/ Reference						
No	**Degraded**	**Length**	**Resonance Frequency (N)**	E	**Average E**	**St. Dev.**
	(Yes/No)	**(mm)**	**(KHz)**	**(GPa)**	**(GPa)**	**(GPa)**
1	NO	47.74	21.40	69.85		
2	NO	49.69	21.40	69.85	**69.85**	**0.00**

Table 4.5: Resonant Frequency values for the reference aluminum sample.

not involve assumption on the Poisson's ratio, thus eliminating another potential source of error.

- *Specimen size*: Very little change in the dynamic modulus of concrete with specimen size has been reported [62] for a frequency range of 70 Hz to 10 KHz. Our values are slightly above, 12 KHz, situated within a narrow band at the upper bound of this range. Several specimen sizes were tested, but little effect of the specimen size on the obtained results was found.

- *Curing conditions*: Jones [62], Kesler and Higuchi [65], Obert and Duvall [86] conducted experiments to determine the effect of moisture content on the dynamic modulus of elasticity. They concluded that the effect of curing condition on the resonant frequency and dynamic modulus of elasticity is critical. They recommended *"Unless special curing conditions are required, water curing is to be preferred and the specimen should be in a water-saturated condition at the time of the test. This will help in achieving more reproducible results."* Specimens used in the experimental program were cured in water at all times, and were in a saturated state during testing.

Cement Paste						
No	**Degraded**	**Length**	**Resonance Frequency (N)**	E	**Average E**	**St. Dev.**
	(Yes/No)	**(mm)**	**(KHz)**	**(GPa)**	**(GPa)**	**(GPa)**
1	NO	54.85	12.45	21.66		
2	NO	54.86	12.47	21.74		
3	NO	54.75	12.43	21.52		
4	NO	54.95	12.39	21.53		
5	NO	54.79	12.50	21.79	**21.65**	**0.12**
6	YES	54.64	5.72	3.23		
7	YES	54.72	5.62	3.13		
8	YES	53.95	5.69	3.12		
9	YES	54.78	5.71	3.24		
10	YES	54.65	5.62	3.12		
11	YES	54.62	5.59	3.08	**3.15**	**0.07**

Table 4.6: Elastic modulus of non-degraded and degraded cement paste calculated from resonant frequency measurements.

Mortar						
No	**Degraded**	**Length**	**Resonance Frequency (N)**	E	**Average E**	**St. Dev.**
	(Yes/No)	**(mm)**	**(KHz)**	**(GPa)**	**(GPa)**	**(GPa)**
1	NO	54.90	12.50	25.02		
2	NO	54.90	12.54	25.18		
3	NO	54.90	12.55	25.22		
4	NO	54.90	12.53	25.14	**25.14**	**0.09**
5	YES	54.91	6.00	4.87		
6	YES	54.90	6.02	4.90		
7	YES	54.89	6.05	4.94		
8	YES	54.82	6.03	4.90		
9	YES	54.83	6.06	4.95		
10	YES	54.87	5.94	4.76	**4.89**	**0.07**

Table 4.7: Elastic modulus of non-degraded and degraded mortar calculated from resonant frequency measurements.

4.3 Destructive Techniques

4.3.1 Uniaxial Compression Tests

The uniaxial compression test is the most common of all tests in concrete engineering, partly because it is easy to perform, and partly because it provides a stress-strain curve, which captures many features of the elastic and inelastic concrete behavior. In our test campaign specimens of varying lengths were tested in a displacement driven uniaxial compression machine located in the department of Materials Science and Engineering at MIT. Throughout the whole testing procedure the apparatus monitors force and displacement. For further accuracy 2 LVDT (transducers) were mounted on the two sides of the platens, and the relative displacement of the platens was recorded. An average value was considered to be indicative of the specimen deformation. Figure 4-6 shows (a) an idealized and (b) a realistic stress-strain curve of mortar. Cement pastes behave similarly, but with a steeper profile, and the linear range extends to a higher stress level.

Area I in Figure 4-6 represents the elastic region of the material. Generally, cement paste and mortar exhibit only little elastic behavior characterized by completely reversible deformations and no energy dissipation. Once the yield point is reached, the material moves into a region of hardening plasticity. The material exhausts quickly this elasticity, and starts exhibiting irreversible deformation. The material behaves in a linear but inelastic way, damaging the material and plastically[3] deforming it. At the macroscopic scale of material description, this region (Area II in Figure 4-6(a)) can be considered as the hardening of the material: reloading after load-unloading results in a material with a higher strength compared to the initial one. We will refer to the slope of the stress-strain curve as tangent modulus E_t. In the case of a loading-unloading cycle, a tangent to the initial part of the unloading provides a measure of the damaged elastic modulus of the material. This damage increases with the applied load, and results in a reduced elastic modulus upon unloading. A measurement of the "true" elastic modulus of the

[3]By "plastic" deformations we mean permanent deformation which remain after complete unloading.

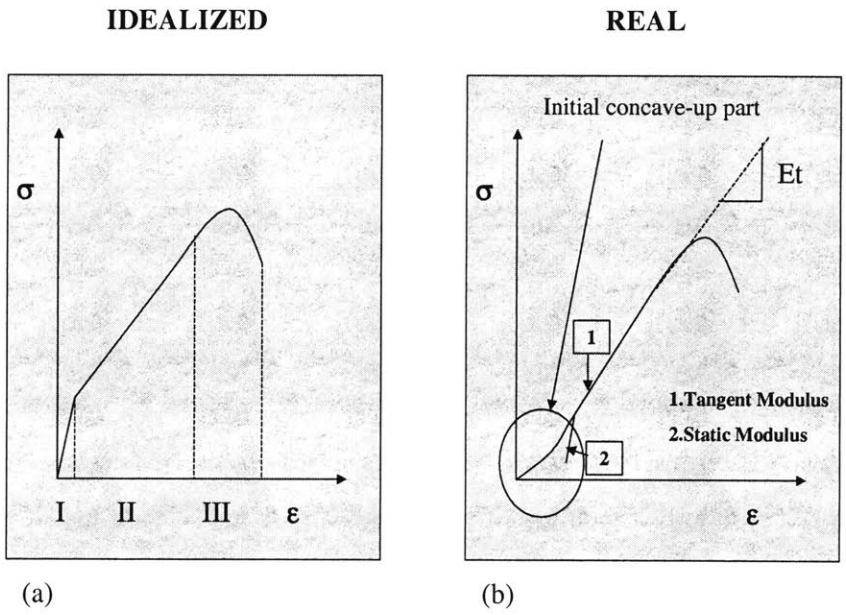

Figure 4-6: Stress/strain curves. (a) Idealized and (b) realistic curve.

undamaged material is provided by any loading or unloading curve which is within the elasticity domain.

The elastic region of cement based composites (mortar, concrete), as for many other materials, is very small, if at all existing. As a result, in real compression tests (Figure 4-6(b)) the initial part of the curve is very difficult to be accurately recorded as it is usually distorted. A small concave part of the curve is usually encountered, which can be attributed to the closing of preexisting fine shrinkage cracks and/or to the incomplete contact of the loading surface at low stresses. This concave part usually includes the elastic response, but also extends into the plastic region. As a result the initial elastic modulus cannot be captured from a uniaxial compression curve. An approximation is obtained by measuring the slope of the unloading part of a cycle performed as early as possible, once complete contact with the machine platen is achieved (Static Modulus; see Figure 4-6(b)). The results of our tests are summarized in Table 4.8.

	Degraded	Tangent Modulus (E_t)		Static Modulus[4]
	YES/NO	Average		Average
Cement Paste	NO	7.65 ± 0.64		18.57 ± 0.59
Cement Paste	YES	0.26 ± 0.05		0.71 ± 0.21
Mortar	NO	11.93 ± 0.38		21.60 ± 0.36
Mortar	YES	0.30 ± 0.03	0.09 ± 0.01	0.49 ± 0.03

Table 4.8: Average values of tangent and static modulus

Parameter Study

- *Effect of end conditions*: When tested in compression the top surface of the test cylinder is brought in contact with the platen of the testing machine. The surface is not obtained by casting against a machined plate, but finished by means of a float (gravity). The resulting top surface is somewhat rough and not truly plane. Under such circumstances stress concentrations are introduced and the apparent stress-strain behavior of the sample in the test is distorted. Convex end surfaces have a more significant effect than concave ones, as they lead to higher stress concentrations [84, p. 130]. To avoid such an influence in our measurements, the end of our samples were carefully cut using a high quality diamond saw. To verify the good quality of our testing procedure, several samples of the same material were carefully polished and tested. The results matched the ones obtained on samples cut with the diamond saw machine, thus confirming the high accuracy of the surface preparation. This delicate cutting procedure gives a smooth surface that minimizes the friction between the end surface and the platen. In addition, several samples were tested using lubricants at the end of the cylinders, and gave identical results. We, therefore, conclude that the diamond saw is creating a surface capable of eliminating most of the restraining influence of friction. In addition, to be plane and relatively frictionless, the end surfaces of the specimen should be normal to its axis. However, experimental data suggest that a small tolerance is permitted. An inclination of the axis of the specimen to the axis of the machine on the order of 1 in 50 was found to have little influence [43]. To further avoid lack of parallelism, a

spherical seat was provided, and a free alignment was achieved.

- *Effect of height/diameter (h/d) ratio*: This effect originates from the friction between platen and sample surface. If the friction is eliminated, which is very difficult to achieve, the effect of h/d on strength disappears. Extensive research [44] has been done on the effect of the h/d-ratio on the compressive strength of samples, suggesting that little effect is observed when the h/d-ratio is in the range of $1.5-4$. The elastic modulus is within 5 % of the elastic modulus of standard specimens ($h/d = 2$) for h/d values between $1.5 - 2.5$. For values greater than 5, the effect of the slenderness ratio becomes apparent. Experimental data shows that the end effect is less pronounced with increasing inhomogeneity; it is thus less noticeable in the case of mortars [84, p. 33]. Our samples were within the range of $1.5 - 2.5$ and the end conditions were carefully prepared. Samples of varying length (the h/d-ratio was kept within $1.5 - 2.5$) were tested and little variation was observed ($\pm$ 1 %).

- *Effect of loading rate application*: The rate of application of the load/displacement can significantly affect the apparent behavior of the concrete sample. The rate used in our experimental procedure was within the range of $0.14-0.34$ MPa/s prescribed by ASTM C 39-93a. For this loading rate range, variations of the elastic modulus is between 97 % to 103 % compared to a rate of 0.2 MPa/s [43].

- *Moisture conditions*: Both British and ASTM standards require that the test specimens be tested in wet or moist conditions as this ensures a better reproducibility than dry conditions [84, p. 33]. In our case, wet samples were tested at all times, not only to improve our reproducibility, but also to avoid any possible cracking induced during the drying process.

- *Accuracy of LVDT*: A small fluctuation on the LVDT measurements was observed during testing, which resulted in a graph similar to the one shown in Figure 4-7a. Therefore, the data was filtered, and the average values were used. In order

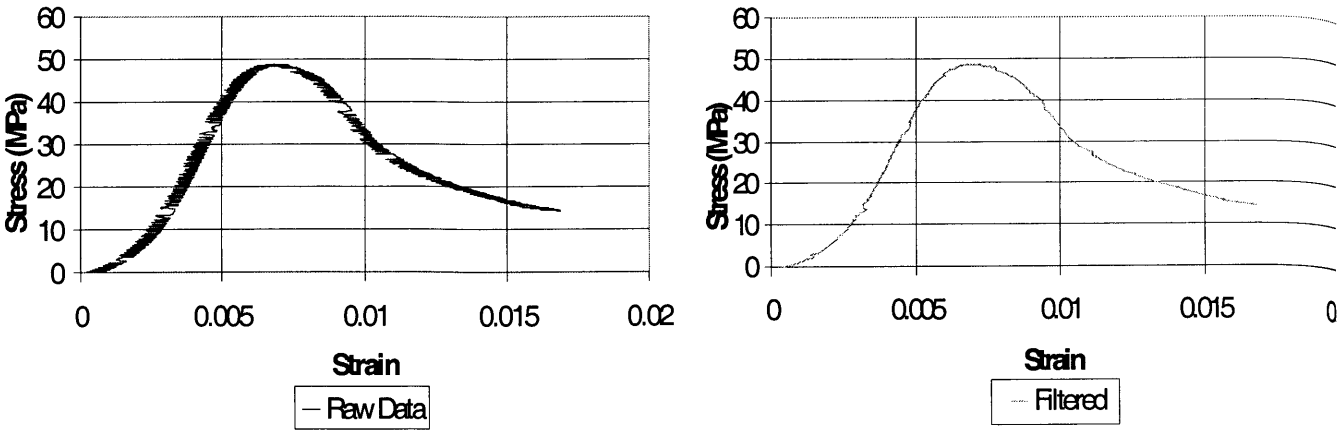

Figure 4-7: (a) Raw and (b) filtered data obtained from uniaxial compression tests.

to achieve the best possible filtering, we performed a test at constant load and displacement, and plotted the LVDT measurements against time. The result, which is indicated in Figure 4-8 is a harmonic wave. The number of points included in a single cycle were counted and used for averaging [39].

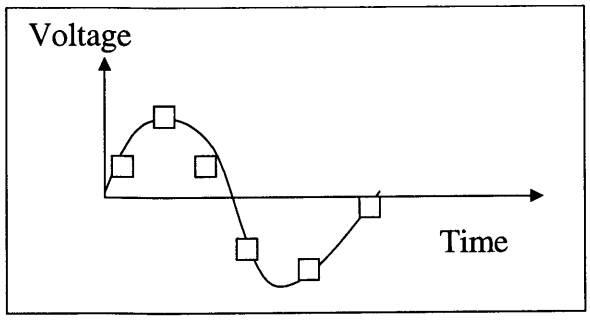

Figure 4-8: Voltage measurements fluctuation under constant load.

	Cement Paste		Mortar	
	Non-Degraded	Degraded	Non-Degraded	Degraded
UPV-Pulse Modulus	22.8 ± 0.5	3.6 ± 0.2	26.5 ± 1.8	5.3 ± 0.1
RF-Dynamic Modulus	21.7 ± 0.1	3.2 ± 0.1	25.2 ± 0.1	4.9 ± 0.1
UC-Static Modulus	18.6 ± 0.6	0.7 ± 0.2	21.6 ± 0.4	0.5 ± 0.1

Table 4.9: Summary of elastic moduli obtained by different methods: UPV,RF and UC

4.4 Discussion

The discussion of the experimental data is divided into two parts. Firstly, the elastic performance of the material assessed by all three methods is presented, and then the elastoplastic behavior indicated by the stress-strain curves is discussed.

4.4.1 Elasticity

The macroscopic elastic modulus was measured using 3 different techniques, and the results are summarized in Table 4.9. The values vary depending on the nature of the test. The two non-destructive methods (UPV,RF) provide data representative of the "true" elastic modulus of the material. The stress applied in these methods is very small, and the behavior of the material during the test is purely elastic. The tests involve very small strains, and the measured elastic modulus coincides with the tangent to the origin of the stress-strain curve. However, the pulse or dynamic modulus measured by UPV or RF technique, is higher than the static modulus measured in a conventional stress-strain test, in which the material operates partly in the inelastic range. Figure 4-9 shows the degradation of the elastic modulus with increasing plastic deformations. Table 4.9 shows that UC measurements are significantly lower than the ones obtained by non-destructive techniques. In summary, UC tests do not allow identifying the elasticity domain. The elastic modulus measured on first unloading is representative of the already mechanically degraded (to a certain degree) specimen. The effect is even more pronounced in the case of chemically degraded materials.

Theoretically the values of the elastic modulus measured by non-destructive tech-

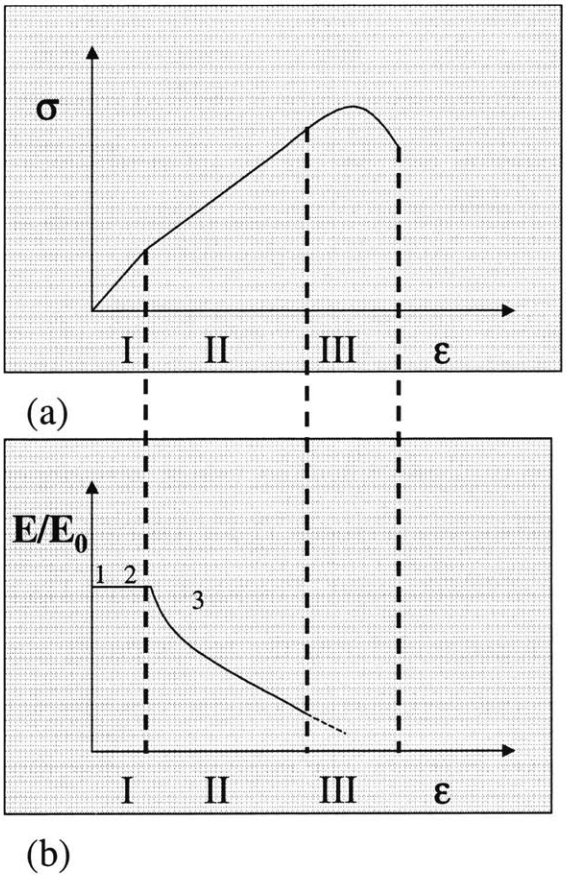

Figure 4-9: Degredation of the elastic modulus with increasing strain: 1=UPV,2=RF,3=UC.

niques (UPV, RF) should be the same. However, in our tests RF values are, on average, 5 % and 10 % lower for non-degraded and degraded specimens, respectively. Philleo et. al. [19] reported attempts to relate the pulse to the dynamic modulus of elasticity. Their extensive experimental studies on 300 samples indicate that the dynamic modulus is on average 15.4 % lower than the pulse. The high quality of equipment used for the UPV measurements, in addition to the high reproducibility of the data, led us to consider UPV values for further analysis in this research. It should be noted that although RF and UPV methods did not give the same results, the relative average drop in elasticity due to calcium leaching, is the same in both methods for both cement paste and mortars. Both methods recorded residual values of 16% and 20% for cement paste and mortar respectively.

4.4.2 Inelasticity

Uniaxial compression tests provide the complete stress-strain behavior of the material. Figure 4-10 shows the significant change in the response of a mortar due to chemical degradation. A similar effect is observed for cement paste samples. The elasticity domain is significantly decreased, and the onset of plastic deformations occurs almost with load application. The degraded material exhibits large deformations and hardening behavior. In order to analyze the data and compare it with the non-degraded samples, a simple 1-D hardening plasticity model is considered. The model is displayed in Figure 4-11. A spring of stiffness E is connected in series with a second spring of stiffness H, which is activated during plastic loading. The force in the elastic spring reads:

$$\sigma = E(\varepsilon - \varepsilon^p) \tag{4.16}$$

Let χ be the relative length increase of the hardening spring and ζ the associated hardening force resisting the extension:

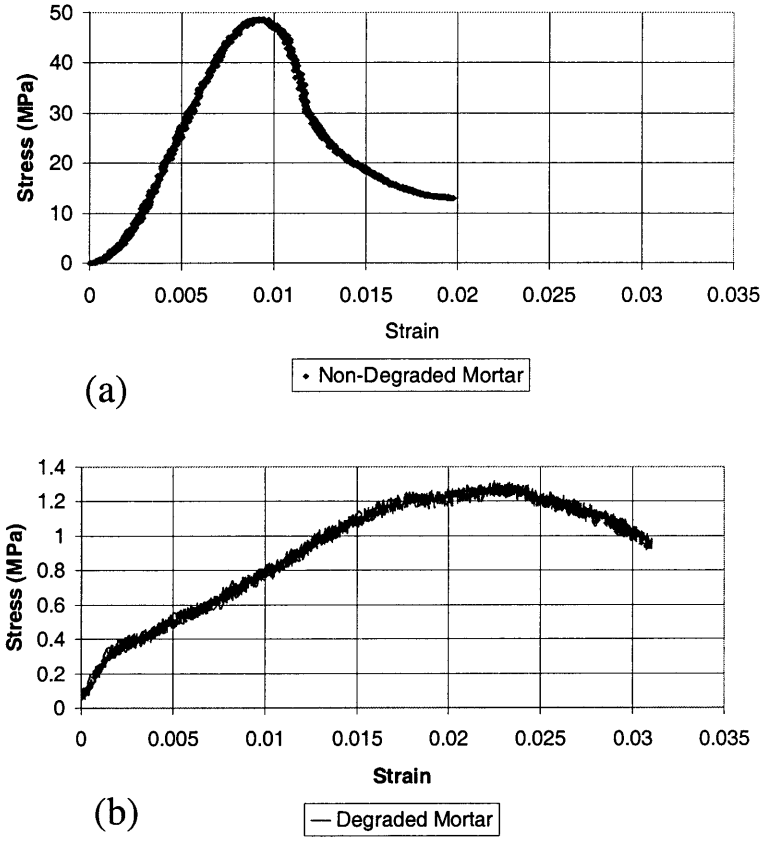

Figure 4-10: Stress-strain curves for (a) non-degraded and (b) degraded mortar. The effect of chemical degradation is apparent.

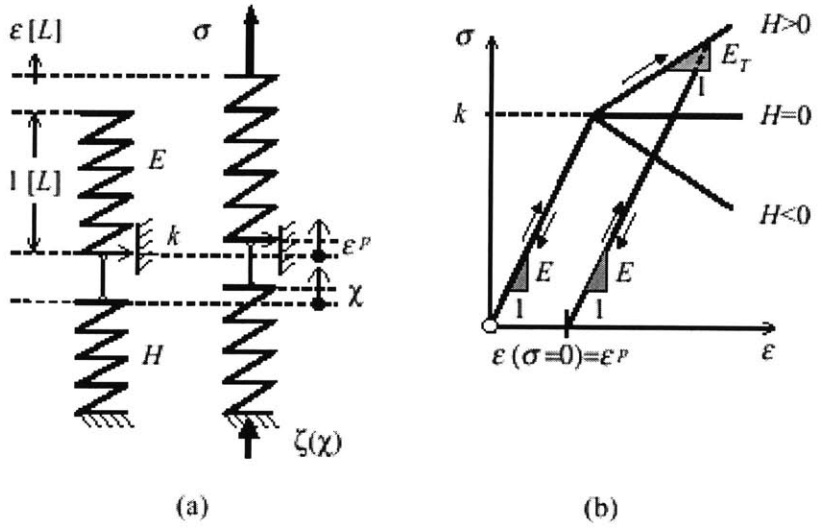

Figure 4-11: 1-D Hardening plasticity model used for analysing the uniaxial compression data [106].

$$\zeta = -H\chi \tag{4.17}$$

The 1-D elasticity domain of the material is expressed in form of the following loading function:

$$\sigma \in D_E : f(\sigma, \zeta) = \mid \sigma + \zeta \mid -k \leq 0 \tag{4.18}$$

where k denotes the strength of the friction element. Satisfying compatibility of the system implies:

$$\chi \equiv \varepsilon^p \tag{4.19}$$

Use of the consistency condition ($df = 0$) during plastic deformation yields the plastic strain increment and the tangential stress strain relation:

	Cement Paste		Mortar	
	Non-Degraded	**Degraded**	**Non-Degraded**	**Degraded**
Hardening Modulus (GPa)	11.6 ± 0.1	0.3 ± 0.06	21.9 ± 0.42	0.1 ± 0.01

Table 4.10: Hardening modulus of non-degraded and degraded specimens

$$d\sigma = \frac{EH}{E+H} d\varepsilon \tag{4.20}$$

The tangent modulus, $E_T = \frac{EH}{(E+H)}$, for the degraded and non-degraded specimens is obtained from the stress-strain curves (see Table 4.8), and the hardening modulus, H, is determined.

Table 4.10 summarizes the average values of the hardening modulus for cement paste and mortar. We note that the presence of aggregates in non-degraded mortar significantly enhances the hardening behavior of the material compared to the cement pastes by a factor of almost 2. However, the degraded mortar has a lower hardening modulus than the degraded cement paste. This chemical softening behavior can be seen in Figure 4-12 where the stress-strain behavior of mortar is softer than the one of cement paste. We therefore conclude that chemical degradation affects in particular the ITZ of mortar leading to the lower hardening capacity of degraded mortars.

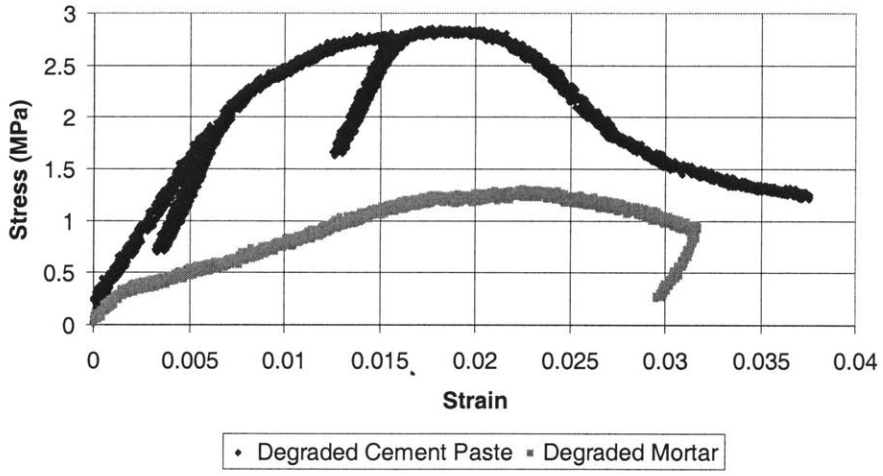

Figure 4-12: Stress-strain curves of degraded cement paste and mortar. The effect of chemical degradation on mortar can be clearly identified.

Chapter 5

Microscopic measurements

The macroscopic degradation of the elastic modulus was identified and quantified in the previous chapter. A microscopic investigation is in addition required for a complete understanding of the material behavior in the calcium leached state. This is the focus of this chapter, which presents the results of the SEM investigation and nanoindentation tests.

5.1 SEM Investigation

Scanning Electron Microscope (SEM) provides qualitative information of the microstructure of cement-based materials, and of its evolution through chemical degradation. The investigation presented here was carried out using a JEOL6320FV SEM of the Center of Materials Science and Engineering (CSME) at MIT. Specimens were prepared with polished, epoxy-impregnated surfaces. Further information on the experimental procedure and sample preparation can be found in detail in [56].

Figure 5-1 shows SEM images of a non-degraded and degraded cement paste. The images reveal a new group of pores at a scale of 10^{-6}m to 10^{-4}m (Figure 5-1(b)). This is the space previously occupied by large CH crystals. Figure 5-2 shows the transformation of the C-S-H phase due to chemical degradation on the micrometer scale. The degraded

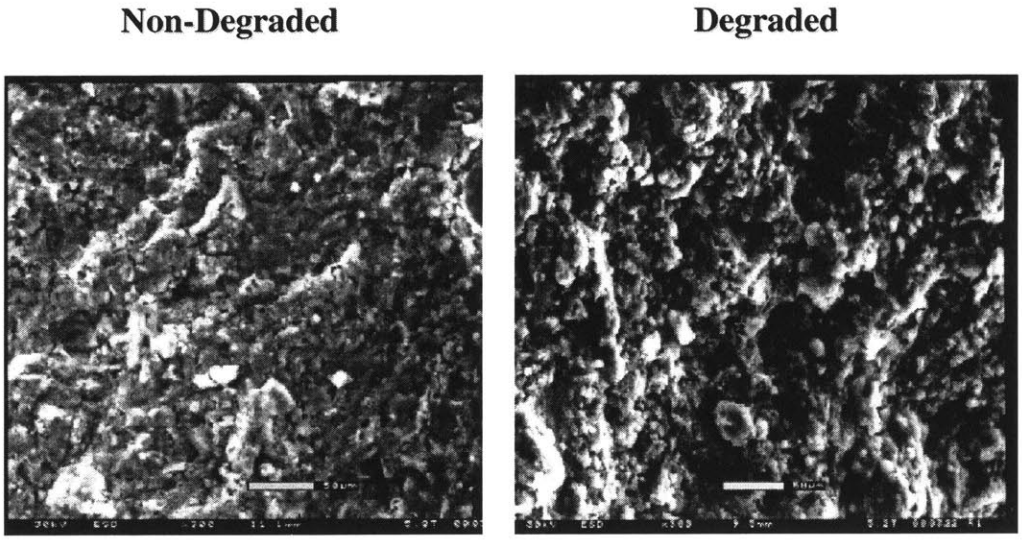

Figure 5-1: Degraded(left) and non-degraded (right) cement paste as seen at the scale of 10^{-5} m. The new pore group created at that scale from the depletion of large CH crystals can be identified [54].

material is characterized by an increased porosity, high homogeneity and uniformity. The microstructure in Figure 5-2(b) may be attributed to the reduction of the C/S-ratio with decalcification. In fact, a reduction of the C/S-ratio favours polymerization of the C-S-H chains [101, p. 118] [32] resulting in a material with continues structure and much smaller subparticles (no clusters). Similar observations have been reported for calcium leached materials using Nuclear Magnetic Resonance (NMR) technique [56]. Furthermore, mortar specimens exhibit similar characteristics after degradation. The effect of leaching is, however, more pronounced in the immediate vicinity of the aggregate surface (ITZ) where the volumetric proportions of CH and Ettringite, are higher than in the bulk paste (see Figure 2-3). Since these compounds are leached by the chemical degradation, the ITZ is heavily affected characterized by a large connected porosity and weak "links" at the aggregate surface, as shown in Figure 5-3. The weakness of this region might be the cause for the weak macroscopic hardening behavior observed in the stress-strain performance found for degraded mortar specimens (see section 4.4.2).

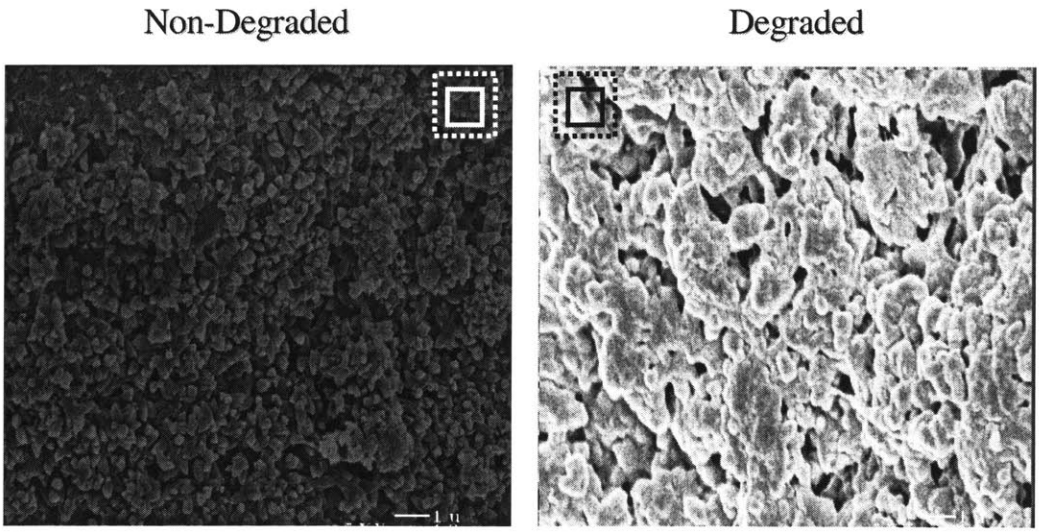

Figure 5-2: SEM pictures of the C-S-H phase. The transformation of the phase by chemical degradation is shown on the right. Solid and dotted squares in the picture indicate the approximate contact area and affected area during a single indentation [54].

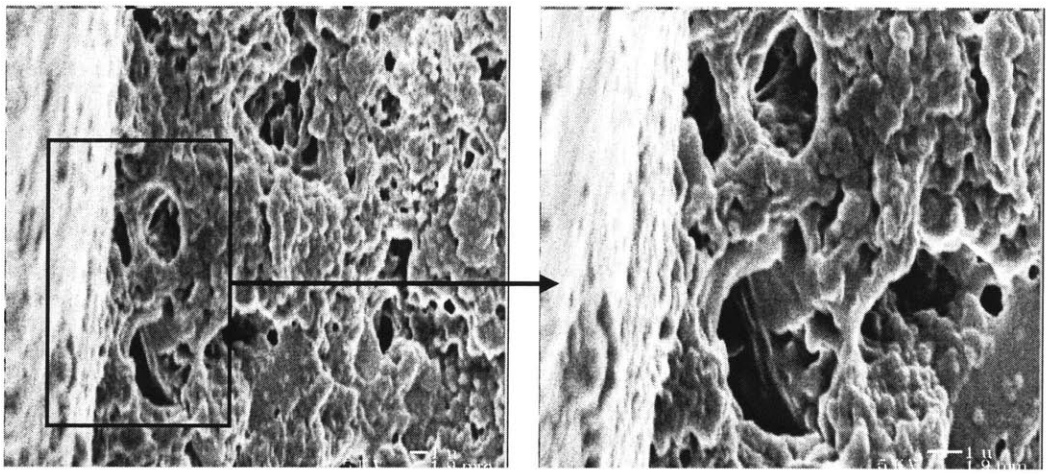

Figure 5-3: Magnification of the interface between sand particle and degraded cement paste. The effect of degredation appears more pronounced in an area previously dominated by the presence of CH and ettringite crystals [54].

5.2 Nanoindentation

The use of instrumented indentation was adopted in this research to assess the elastic properties of the individual constituents of cement paste at scale of 10^{-6} m. In addition, the elastic properties of the chemically degraded phases are measured and their relative contribution to the macroscopic stiffness degradation is quantified.

5.2.1 Experimental Device and Measurements

Specimen Preparation

Cylindrical specimens were cut in slices of an approximate thickness of $10-15$ mm. The surfaces were ground and polished with silicon carbide papers and diamond particles to obtain a very flat and smooth surface finish. This was done in 6 stages of decreasing fineness with the last one being in the range of 0.25 μm. Special attention was paid to keep the specimens flat and parallel on both sides, since this could influence the angle of indentation and thus the result of the measurements. After polishing, the samples were placed in an ultrasonic bath to remove the dust and diamond particles left on the surface or in the porous structure.

Experimental Set-up

The employed apparatus is a NanoTest 200 located in the Laboratory of EXperimental and Computational Micromechanics (LEXCOM) in the Materials Science and Engineering Department at MIT. The device allows monitoring the load (P)-displacement (h) relationship in a load range of 0 to 20 N, and in a displacement range of 0 to 50 mm, with resolutions of 100 nN and 0.04 nm, respectively. The operating principle of the test apparatus and the continuous depth recording measurement device are illustrated in Figure 5-4.

A pendulum pivoting around frictionless bearings applies the load to the specimen. A current passes through a coil mounted at the top of the pendulum and attracts the

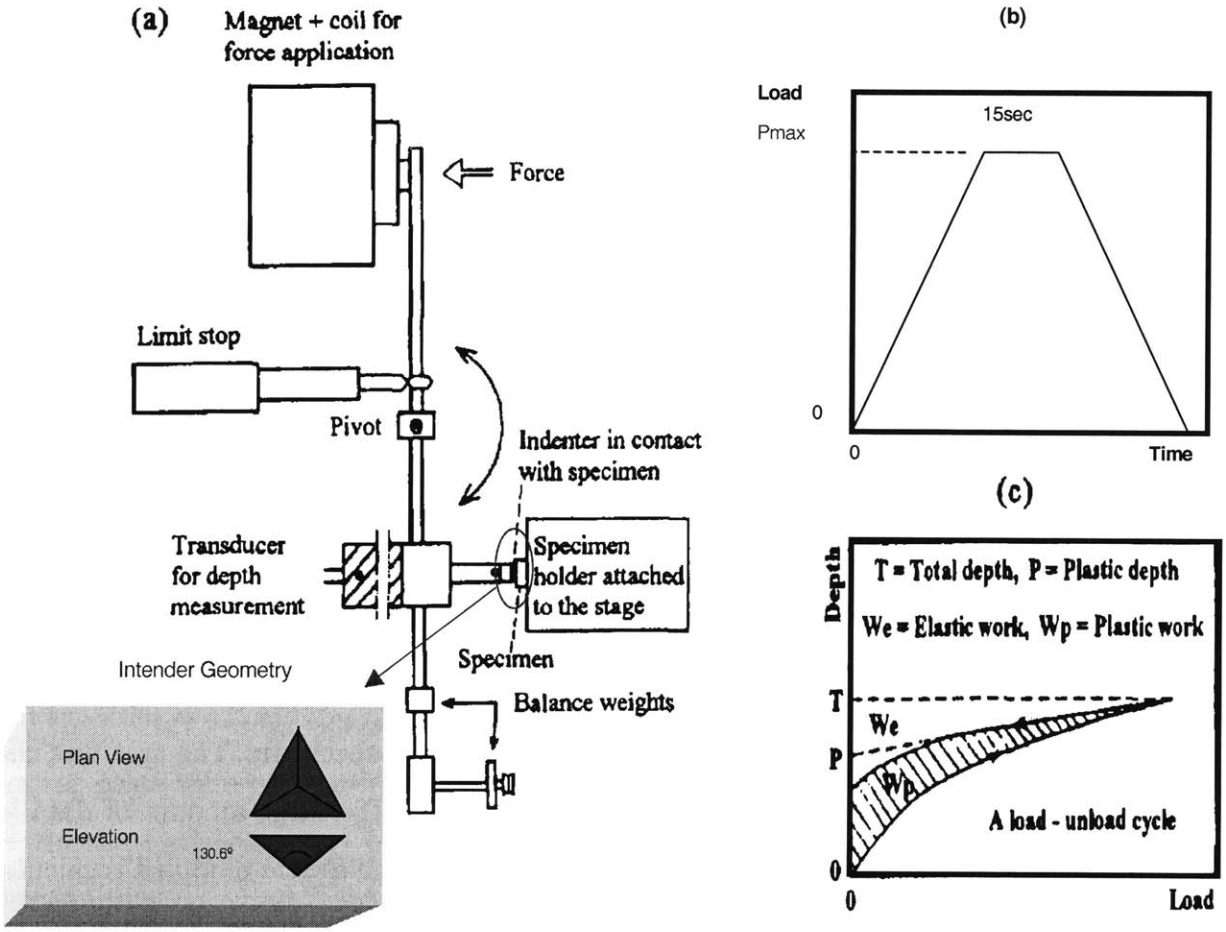

Figure 5-4: Experimental set-up of nanoindenter: (a) Berkovich indenter; (b) prescribed loading for a single cycle; (c) typical load-displacement graph [117].

coil to a fixed magnet. This sets the indenter into motion to the specimen surface which is firmly clamped to the loading stage. The displacement of the indenter (depth h of penetration into the specimen) is continuously monitored and recorded by the change in the capacitance of a parallel plate capacitor. In this way the complete $P-h$ response is obtained. A load cycle is shown in Figure 5-4(b), and a typical $P-h$ response in Figure 5-4(c). The used loading rate is 2.3 mN/s, which is slow enough to approximate quasi-static conditions. The indentation depth varies in the range of $300-500$ nm. In order to avoid possible overlapping of the affected areas, the distance between indentation points is controlled. Repeated loading-unloading cycles were performed in some of the tests to assess the pure elastic behavior of the material in that range.

Other features of the instrument include: (a) a personal computer control, which is used for monitoring, and data manipulation; (b) an optical microscope, which is used to locate the different cement paste phases and the test points, and to align the specimen beneath the indenter. Large Portlandite crystals are easily identified under the microscope, and their modulus is determined by indenting on them. However, measurements on the C-S-H could not be resolved with the use of microscope due to their very small characteristic length scale, and a series of 200 indentations covering an area of $1000\mu m^2$ (10 times the area of Figure 5-2) was conducted on each specimen. The area was chosen to be statistically representative of the C-S-H matrix. The large amount of data lends itself to a statistical analysis. After analyzing the data the elastic modulus is calculated. A frequency plot of the data is given in Figure 5-8. From this figure the mean value and standard deviation are extracted.

5.2.2 Analysis of Data

The response of a material to the multiaxial loading during indentation is governed by contact mechanics. This theory is completely general and can thus be applied over a range of size scales and for many indenter geometries. Two distinct classes of instrumented indentation exist; (a) Sharp indentation, which assumes elastoplastic deformation due to

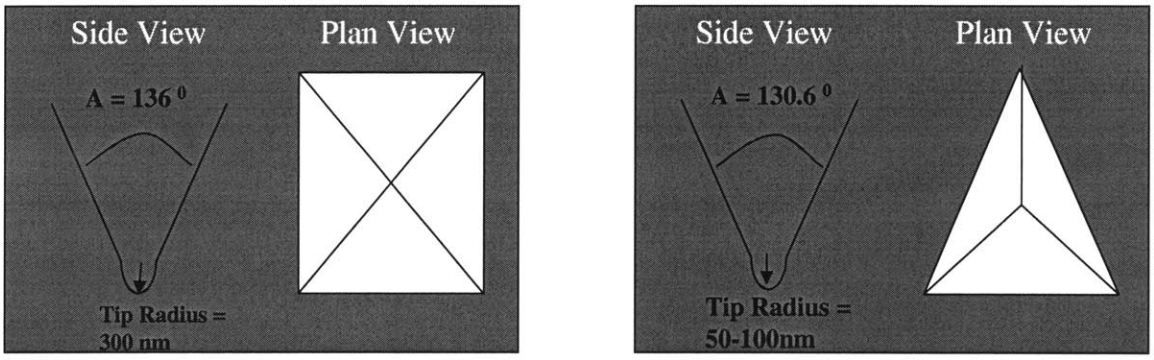

(a) Vickers (b) Berkovich

Figure 5-5: Geometrical features of (a) Vickers and (b) Berkovich indenter; after [111].

the almost immediate onset of plastic yielding, caused by the stress singularity at the indenter tip; and (b) Spherical indentation, which assumes initial elastic deformation, followed by the onset of yielding and subsequent plastic deformation. The geometry of the sharp indenter allows measurements to be performed at very fine scales (10^{-6}m); and it was adopted in this study. The two types of sharp indenter available at LEXCOM and their exact geometry are shown in Figure 5-5. Tests on degraded and non-degraded cement paste were performed using a Berkovich indenter (Figure 5-5(b)).

As the load is applied to an indenter in contact with a specimen surface, an indent/impression is produced that consists of permanent plastic deformation and elastic deformation. Recovery of the elastic deformation occurs during unloading. Determination of the elastic recovery by analyzing the unloading data according to a model for the elastic contact problem leads to a solution for calculation of the elastic modulus, E, of the test area. Several methods exist in the literature for analyzing the data. The most frequently used are the ones of Oliver and Pharr [88], Derner and Nixx [30] and the one developed at LEXCOM [42, 111]. All three types of analysis were employed in this study. The results obtained with the LEXCOM and Oliver-Pharr models were in very good agreement. Estimations of the elastic modulus using Derner and Nix method

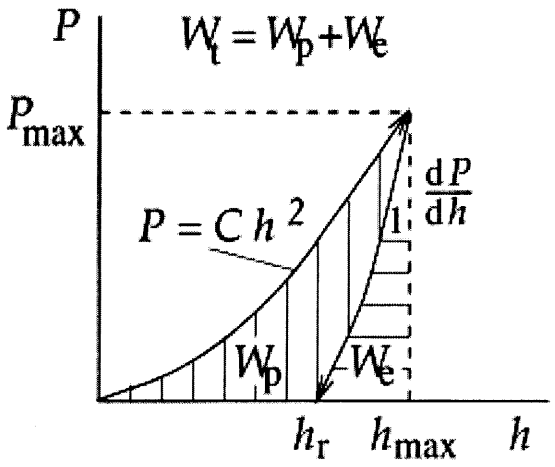

Figure 5-6: $P - h$ curves for loading and unloading, and the associated nomenclature.

deviated by $\pm$ 10 %. The first two can be considered as more reliable, as they account for the effect of the material pile-up or sink-in. They, therefore, account for the effective area of indentation. The analysis described below follows the one of LEXCOM. A more detailed derivation of this method is presented in Appendix B.

The problem at hand has four unknowns: the elastic modulus E, the yield stress σ_y, the stress corresponding to the characteristic plastic strain of 0.29 for the indented material in uniaxial compression $\sigma_{0.29}$ (see Appendix B), and the hardness p_{av}=P_{max}/A_{max}. A complete instrumented indentation $P - h$ curve obtained during loading and full unloading gives the following four parameters: the loading curvature $C = P_{max}/h_{max}^2$, the initial unloading slope dP/dh, the maximum indentation depth h_{max} and the residual depth of penetration, h_r (see Figure 5-6). Through finite element simulation the ratio of plastic work to total work W_p/W_t is related to the ratio $h_r/h_{max} = W_p/W_t$; and therefore knowledge of the plastic work from the area under the indentation curve (Figure 5-4c) may also suffice instead of measuring the residual depth of penetration [42]. The problem is thus well posed. Based on the equations presented in Appendix B the following relations hold:

$$1 - \frac{W_p}{W_t} = 1 - \frac{h_r}{h_{\max}} = d^* \frac{p_{av}}{E^*} = d^* S \tag{5.1}$$

where $d^* = 5$ for the Vickers pyramid indenter and $d^* = 4.678$ for the Berkovich indenter.

$$\frac{A_{\max}}{h_{\max}^2} = 9.96 - 12.64(1-S) + 105.42(1-S)^2 - 229.57(1-S)^3 + 157.67(1-S)^4, \text{ with } S = \frac{p_{av}}{E^*} \tag{5.2}$$

$$E^* = [\frac{(1-\nu^2)}{E} + \frac{(1-\nu_{in}^2)}{E_{in}}]^{-1} = \frac{1}{c^* \sqrt{A_{max}}} (\frac{dP}{dh}) = \frac{d^* p_{av}}{(1 - \frac{W_p}{W_t})} \tag{5.3}$$

where ν is Poisson's ratio, the subscript 'in' denotes properties of the indenter, and dP/dh is the slope of the $P-h$ curve at the initial stages of unloading from P_{max} The constant $c^* = 1.142$ for the Vickers pyramid indenter, and c^* =1.167 for the Berkovich indenter. In determining the elastic modulus the method involves the following steps:

1. The $P-h$ curve is experimentally determined for a complete loading and unloading cycle.

2. From the $P-h$ curve, h_r and h_{max} are determined and h_r/h_{max} is calculated.

3. Using the value of h_r/h_{max}, we find $S = p_{av}/E^*$ from Eq. (5.1). Alternatively, we can estimate the ratio of the plastic work to total work, W_p/W_t, graphically from the $P-h$ curve; and applying the left part of Eq. (5.1) we find S.

4. With S in hand (Step 3), and h_{max} directly read from the $P-h$ curve, we obtain the true contact area at maximum load, A_{max}, from Eq. (5.2). Alternatively it can be determined graphically (see Figure B-5 in Appendix B).

5. By determining the initial unloading slope dP/dh, and using A_{max} (Step 4), we calculate E^* using the right hand side of Eq. (5.3). The elastic modulus can then be calculated using the left hand side of (5.3), with the help of the known elastic properties of the indenter, E_{in} and ν_{in}.

The method of LEXCOM circumvents, by design, the need for visual observations of the contact area and incorporates into the analysis the effects of pile-up and sink-in. This method is valid provided that the diameter of the impression made by the indenter spans at least five times the characteristic length scale of the inhomogeneity (which is the limitation of the underlying continuum mechanics analysis). In our study, indentation areas, which are shown in Figure 5-2, are on the order of 10^{-6}m, which is considerably larger than the characteristic inhomogeneities (pores) present at a scale below. For purpose of confirmation of the obtained results the method of Oliver and Pharr [88] was also used providing, on average, results with excellent agreement (deviation $< \pm$ 1 %).

5.2.3 Comment on Sensitivity of Nanoindentation Measurements

This section investigates the sensitivity of the results in terms of (a) the quality and accuracy of the used equipment and (b) the different parameters introduced in the analysis. This two factors are independent of each other and are, therefore, separately discussed.

Measurements

The loading and unloading characteristics of the $P - h$ curve, which give access to the micromechanical properties of the material, depend on the experimental setup used to perform the experiments, i.e. machine compliance, friction between indenter and indented material, surface roughness, specimen clamping, sharpness of the indenter tip, residual stresses locked in the material during preparation, and so on. The high precision equipment combined with the detailed and careful execution of the experiments ensure the good quality of the experimental data. The used apparatus was calibrated before each test to ensure the accurate recording of the $P - h$ material response. Figure 5-7 taken from [111] shows the sharpness of the indenter, demonstrating the high quality of the used equipment.

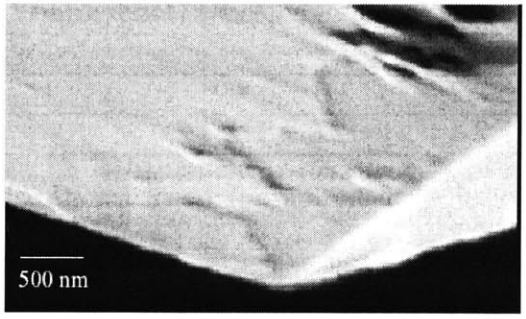

Figure 5-7: A scan electron micrograph showing the sharpness and symmetry of the Berkovich indenter tip used in the nanoindentation experiments [111].

Analysis

The sensitivity of the elastic modulus estimation to variations in the input parameters obtained from the $P-h$ curves was investigated in [111] for a number of different materials. For each of these materials, the sensitivity of the estimated elasto-plastic properties to variations in the three parameters - C, dP/dh, and W_p/W_t- around their respective true values (as estimated from forward analysis), was examined. In general, the elastic properties estimated through the reverse analysis displayed weak sensitivity to variations in the loading curvature, C, and the unloading slope, dP/dh, but exhibited strong sensitivity to variations in the plastic work ratio as examined in more details below. It was found that: (i) If the plastic work ratio is known within an error of $\pm$ 4 %, the elastic modulus is estimated within errors of $\pm$ 10 %. However in the case of brittle materials and composite materials (alloys) the sensitivity was weaker with estimations being within $\pm$ 6 %. Nevertheless the error is still significant, and for this reason the determination of $A_{\max}$ apart from the plastic work ratio was also monitored using the displacement method. (ii) In general, the sensitivity to changes in the positive and negative directions (i.e. overestimating and underestimating the plastic work ratio, respectively) are asymmetrical; with the largest deviation in the computed elastic modulus occurs when the plastic work ratio is overestimated by 4 %. It should also be noted that a sensitivity

	Elastic Modulus (GPa)		Residual Value (%)
	Non-Degraded	**Degraded**	**[Degraded/Non-Degraded] x100**
CH	38.0 ± 5	–	–
C-S-H_a	21.7 ± 2.2	3.0 ± 0.8	14
C-S-H_b	29.4 ± 2.4	12.0 ± 1.2	41

Table 5.1: Elastic Modulus of individual constituents obtained by nanoindentation (Mean/St. Dev.)

analysis of $P - h$ variations of E indicates that E values are relatively insensitive to Poisson's ratio; variations are estimated to be within $\pm$ 1 %.

5.3 Discussion

The elastic modulus versus the frequency is plotted in Figure 5-8 and the mean and standard deviation are extracted. The experimental results displayed in Figure 5-8 are summarized in Table 5.1, and suggest the existence of two types of C-S-H compounds present at a scale of 10^{-7}m. These two types of C-S-H appear to loose their stiffness with the depletion of calcium from their skeleton (Figure 5-8). The existence of two types of C-S-H can be clearly identified in the degraded state, for which a clear bimodal distribution is found (Figure 5-8(b)). The area under the curves is preserved when moving form the non-degraded to the degraded state. The middle peak in the non-degraded state can be attributed to the overlap of the two distributions. Two types of C-S-H have been previously reported in the literature. However experimental techniques available at the time did not allow quantification. Two recent papers by Richardson [92] and Jennings [60, 102] classify the two types of C-S-H in terms of Outer Product(Op)-Inner Product(Ip) and Low Density(LD)-High Density(HD) C-S-H, respectively. In this study, we identify by stiffness measurements two types of C-S-H. Indentation data provided by Acker [3] on *Ductal*[1] give almost identical stiffness results suggesting that these properties are intrinsic to all type of cement paste materials. The existence of intrinsic properties

[1] An Ultra high performancce concrete produced at very low w/c ratios (~0.18) and use of admixtures.

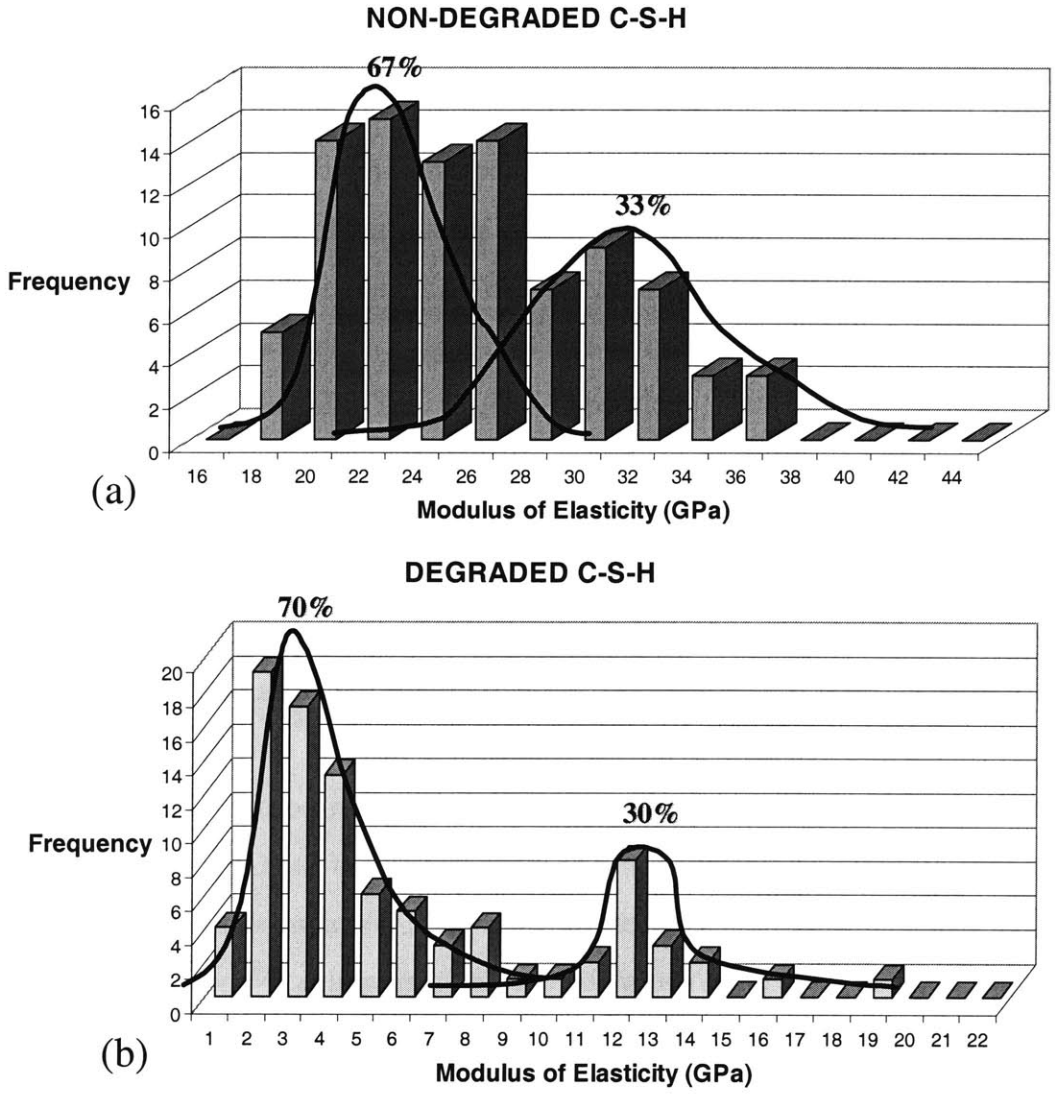

Figure 5-8: Results obtained from nanoindentation. Elastic modulus frequency histogram for C-S-H in (a) non-degraded and (b) degraded state. Two types of C–S-H are identified; C-S-H_a and C-S-H_b. % indicates volumetric proportions obtained by measuring the area under the curves.

at that scale can be attributed to a characteristic packing or arrangement of the two C-S-H types during hydration. These results are consistent with the modified Powers and Brownyard model proposed in Chapter 2.

If we assume that the two types of C-S-H have identical elementary components, it is reasonable to associate the Outer Product with a Low Density C-S-H, that is a Low stiffness C-S-H (C-S-H_a). It is instructive to note from Figure 5-8 that the Low stiffness C-S-H is more heavily affected by the chemical degradation than the High stiffness C-S-H (C-S-H_b); the first has residual values of elastic modulus on the order of 14% of the initial one, in comparison with 41% for C-S-H_b. This observation can be attributed to the increase in porosity, which gives rise to a higher surface area and therefore to a more severe degradation. In turn, enclosed C-S-H_b are less affected by the degradation

5.4 Summary of Experimental Results

The macroscopic elastic modulus of calcium leached cement paste and mortar is significantly affected by chemical degradation with residual values of 16 % (3.6 GPa) and 20 % (5.3 GPa), respectively. Experimental results suggest that the drop in macroscopic elasticity is a coupled consequence of (1) the increase in porosity due to the depletion of large Portlandite crystals, and (2) the loss of stiffness of the C-S-H phase. The depletion of large Portlandite crystals creates a new group of pores present at a scale of $10^{-6} - 10^{-4}$ m, which appears to be detrimental for the elastic modulus. Nanoindentation results suggest the existence of two families of C-S-H which maintain their volumetric proportions with calcium leaching. The loss of C-S-H stiffness can, therefore be attributed to the decalcification of the two types of C-S-H (loss of their intrinsic elasticity) and/or to the increase of meso/microporosity by leaching of probably engulfed nanocrystalline Portlandite and/or Ettringite ($< 1\mu m$). Beaudoin and Feldman [11], provided experimental data of the mechanical properties of C-S-H with different C/S ratios suggesting that the intrinsic elastic properties of C-S-H are independent of the C/S-ratio. This result,

if verified, would indeed suggest that the decrease in C-S-H properties as measured by nanoindentation tests, result from an increase in porosity at lower scales.

Part II

MICROMECHANICAL MODELING

Chapter 6

Continuum Micromechanical Models

The second part of this thesis builds a micromechanical elasticity model to capture the elastic behavior of unleached and leached cement-based materials. The multiscale structure of concrete discussed in Chapter 2 forms the backbone of the developed micromechanical approach, and guides the choice of the homogenization scheme that allows upscaling the elasticity properties from the microscale to the macroscale. This second part is composed of two chapters: Chapter 6 reviews some common upscaling schemes that have been proposed in the open literature, and examines their applicability to calcium leached materials. Based on the shortcoming of the existing approaches, we propose an improved model in Chapter 7, which includes the available information on the mechanical properties of the concrete constituents and their volumetric proportions, obtained by nanoindentation, as well as morphological features obtained from SEM investigation. Finally, the model is applied to non-degraded and degraded materials, and its predictive capabilities are discussed.

6.1 Effective Modulus Models for Concrete

The effective elastic modulus of concrete has been the subject of research for more than half a century. The models found in the open literature fall in one of the following

categories:

1. Empirical relations;

2. Applications of composite materials theory;

3. Computer simulations.

The earliest and simplest models for the elastic moduli of cementitious materials are based on the assumption that concrete (or mortar) consists of two phases: aggregate (or sand particles) and cement paste. To our knowledge, Hansen [47], Dantu and Kaplan [64] were the first to apply the Voigt-Reuss bounds to concrete. These bounds based on parallel (Voigt) and series (Reuss) assumption (see Figure 6-1(a) and (b)), are known to give the largest upper and lower bound of the shear and bulk modulus [57]. Any combination of the upper and the lower bound are situated within these bounds. For concrete considered as a two-phase material, the Hirsch model [59] and the Counto model [28] (Figure 6-1(c) and (d)) propose such combinations. But the physical significance of the combination is not evident. Further refinements found in the literature apply more sophisticated homogenization schemes, evoked in more details below, to the aggregate-cement matrix composite. However, experimental data presented in [85] suggest that a two-phase description of concrete falls short in capturing a salient feature of concrete properties, the ITZ.

With the advent of powerful computers model-based simulations of the effective elastic moduli became possible. Using percolation theory, Bentz and Garboczi developed a digital simulation model that generates the microstructure of cement paste and aggregates [34–37], and predicts the elastic behavior of concrete by finite element simulation. More recently, the effect of the ITZ was incorporated in the model-based computer simulations by a shell around the aggregate in the model [34].

While significant advances have been made in the last years, most of the efforts concentrate on the mm-scale of concrete, where the material can be considered as a three-phase material composed of aggregates, ITZ and matrix (cement paste), e.g. [68,69].

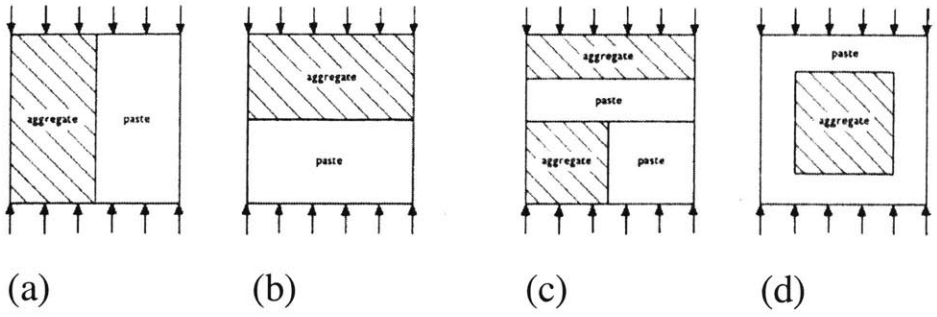

Figure 6-1: (a)Voigt, (b) Reuss, (c) Hirsch, and (d) Counto models

Smaller scales have been the focus of only physical chemistry investigation e.g. [6,61,92, 102]. The modeling approach developed in this thesis focusses precisely on these smaller scales. It aims at (1) complementing physical chemistry models on the mechanics side; by (2) incorportaing the contribution of the different cement paste constituents into the micromechanical approach.

6.2 Homogenization Schemes for Matrix-Inclusion Composite Materials

We present hereafter a non-exhaustive review of some homogenization schemes, that allow determination of the effective behavior of composite materials. Given the particular microstructure of concrete, the review will focus primarily on upscaling schemes for matrix/inclusion morphology, which will turn out, in the next Chapter, to be most appropriate for upscaling the properties of cement-based materials. Some fundamental relations of Continuum Micromechanics are recalled first. Then, following Hashin' presentation [49], we briefly discuss the following four classes of homogenization schemes: (a) Direct Approach, (b) Variational Approach, and (c) Approximations.

6.2.1 Some Fundamental Relations of Continuum Micromechanics

The first idea in studying heterogeneous material systems, that is materials that are composed of different phases, is to address them in a continuous fashion. This is often referred to as the continuum micromechanics approach [95]. The origins of continuum micromechanics can be traced back to the pioneering work of Eshelby [31], who solved the linear elastic problem of an elliptical inclusion in an infinite medium. That approach laid out the foundations for a class of upscaling methods, based on volume averaging and stress-strain localization. The first fundamental relation is that the macroscopic strain $\mathbf{E}$, respectively the macroscopic stress $\boldsymbol{\Sigma}$, of a representative elementary volume (REV), is the volume average of the microscopic strains $\boldsymbol{\varepsilon}(\mathbf{x})$, respectively microstresses $\boldsymbol{\sigma}(\mathbf{x})$:

$$\mathbf{E} = \langle \boldsymbol{\varepsilon} \rangle = \frac{1}{V} \int \boldsymbol{\varepsilon}(\mathbf{x}) dV; \; \boldsymbol{\Sigma} = \langle \boldsymbol{\sigma} \rangle_V = \frac{1}{V} \int \boldsymbol{\sigma}(\mathbf{x}) dV \tag{6.1}$$

where V is the REV, and $\mathbf{x}$ the position vector.

The second fundamental idea of Continuum Micromechanics is that it is possible to separate the heterogeneous matter into zones or phases with specific material properties, say an elastic stiffness $\mathbf{c}_r$, and volume fractions, say $f_{r=1,N} = V_r/V$, such that $\sum_{r=1}^{N} f_r = 1$, where N denotes the number of phases present in the REV. A phase, in Continuum Micromechanics, is not necessarily a distinct material, but rather a subdomain of the overall matter characterized by an on-average constant stress or strain state. As such, a phase may well be composed of different materials. In the simplest case, that is in linear elastic problems, one typically links the microscopic stresses and strains to the corresponding macroscopic quantities through localization relations of the type:

$$\boldsymbol{\varepsilon}(\mathbf{x}) = \mathbf{A}(\mathbf{x}) : \mathbf{E}; \quad \boldsymbol{\sigma}(\mathbf{x}) = \mathbf{B}(\mathbf{x}) : \boldsymbol{\Sigma} \tag{6.2}$$

where $\mathbf{A}(\mathbf{x})$ and $\mathbf{B}(\mathbf{x})$ represent the 4th order stress- and strain localization tensor, or

concentration tensor, respectively. In some special cases, these tensors are found from the solution of continuous elastic boundary value problems for an idealized geometrical microstructure, at the boundary of which the macroscopic strain, respectively macroscopic stress, are prescribed in a regular fashion. These regular displacement/stress boundary conditions, which need to be satisfied in an average sense [49], read:

$$\text{on } \partial V : \mathbf{u} = \mathbf{E} \cdot \mathbf{x};\ \mathbf{T} = \boldsymbol{\Sigma} \cdot \mathbf{n} \tag{6.3}$$

where $\mathbf{n}$ is the unit outward normal to the boundary ∂V of the REV. Given these regular boundary boundaries, it is straightforward to show, from a combination of (6.1) and (6.2), that the volume average of $\mathbf{A}(\mathbf{x})$ and $\mathbf{B}(\mathbf{x})$ over V corresponds to the 4th unit tensor, that is:

$$\mathbf{E} = \langle \boldsymbol{\varepsilon}(\mathbf{x}) \rangle_V = \langle \mathbf{A}(\mathbf{x}) : \mathbf{E} \rangle_V = \langle \mathbf{A}(\mathbf{x}) \rangle_V : \mathbf{E} \rightarrow \langle \mathbf{A}(\mathbf{x}) \rangle_V = \mathbf{I} \tag{6.4}$$

$$\boldsymbol{\Sigma} = \langle \boldsymbol{\sigma}(\mathbf{x}) \rangle_V = \langle \mathbf{B}(\mathbf{x}) : \boldsymbol{\Sigma} \rangle_V = \langle \mathbf{B}(\mathbf{x}) \rangle_V : \boldsymbol{\Sigma} \rightarrow \langle \mathbf{B}(\mathbf{x}) \rangle_V = \mathbf{I} \tag{6.5}$$

Finally, it suffices to introduce relevant constitutive relations for the different phases contained in V. For instance, in the case of a linear elastic behavior of all phases, the macroscopically 'effective' material properties (stiffness tensor $\mathbf{C}$) are obtained from (6.1), (6.2) and the local phase stiffness tensors $\mathbf{c}_r$:

$$\boldsymbol{\Sigma} = \langle \mathbf{c}_r : \boldsymbol{\varepsilon}_r \rangle_V = \langle \mathbf{c}_r : \mathbf{A}_r \rangle_V : \mathbf{E} \equiv \mathbf{C} : \mathbf{E} \rightarrow \mathbf{C} = \langle \mathbf{c}_r : \mathbf{A}_r \rangle_V \tag{6.6}$$

$$\mathbf{E} = \left\langle \mathbf{c}_r^{-1} : \boldsymbol{\sigma}_r \right\rangle_V = \left\langle \mathbf{c}_r^{-1} : \mathbf{B}_r \right\rangle_V : \boldsymbol{\Sigma} \equiv \mathbf{C}^{-1} : \boldsymbol{\Sigma} \rightarrow \mathbf{C}^{-1} = \left\langle \mathbf{c}_r^{-1} : \mathbf{B}_r \right\rangle_V \tag{6.7}$$

Last, a comment on REV is due. The REV refers to a statistically homogenous material volume, which contains a sufficient number of phase volumes or subvolumes V_r so that the REV is in deed representative. Furthermore, under macroscopically uniform stress or strain (i.e. boundary conditions (6.3)), the overall properties are independent of the size of V [95]. This is a pre-requisite for the application of Continuum Micromechan-

ics, which is closely related to the so-called Separation-of-Scale Principle: *"The scale of the inhomogeneity is assumed to be orders of magnitude smaller than the characteristic dimension of the problem of interest, such that there exists the intermediate dimension over which the properties averaging can be legitimately performed"* [25]. This condition needs to be checked for any application of the upscaling schemes presented below.

6.2.2 Direct Approach

The direct approach is based on the exact solution of a linear elastic boundary value problem for a specific geometrical model of a composite material. This direct solution implies that the microfields satisfy the phase governing differential equations (i.e. momentum balance), the interface conditions (Eq. (6.3)) and the external boundary conditions (6.3) applied to the composite. The relevance of such models highly depends on the capacity of the model to represent the microstructure of the composite. The number of choices that permit exact solution is limited. Three of the most common ones relevant for a matrix-inclusion geometry, are described below.

Dilute Scheme

The Dilute Scheme is based on the theory of dilute suspensions, and its origin can be traced back to the 1906 paper of Einstein dealing with the viscosity of a dilute suspension of rigid spheres in a Newtonian viscous fluid. The solid mechanics problem was solved by Eshelby [31]. Physically, this situation holds when the individual particles are so far apart that all interactions between them can be neglected, i.e. the state of strain in one particle is unaffected by any other particle. In his landmark paper [31], Eshelby showed that a single particle of ellipsoidal shape embedded in an infinite body subjected to homogeneous strain boundary conditions, has a state of uniform deformation. Application of the model to spherical particles of concentration f_I that are embedded in a homogeneous medium subjected to simple shear deformation, delivers the effective shear modulus in the form:

$$\frac{G}{G_m} = 1 + \left(\frac{G_i}{G_m} - 1\right) \frac{5\left(3\frac{K_m}{G_m} + 4\right)}{8 + 7\frac{K_m}{G_m} + 6\left(\frac{K_m}{G_m} + 2\right)\frac{G_i}{G_m}} \times f_I \tag{6.8}$$

where subscript i and m represent inclusions and matrix, respectively. Analogously, for a two-phase medium in volumetric deformation, the effective bulk modulus reads:

$$\frac{K}{K_m} = 1 + \frac{\frac{K_i}{K_m} - 1}{1 + \left[\left(\frac{K_i}{K_m} - 1\right) / \left(1 + \frac{4}{3}\frac{G_m}{K_m}\right)\right]} \times f_I \tag{6.9}$$

The linear dependence of $\frac{G}{G_m}$ and $\frac{K}{K_m}$ on f_I is a typical characteristic of the dilute approximation. Indeed, this linear dependence can be viewed as a truncated power series with regard to the particle volume fraction, which is of the form of Einstein's original solution:

$$\frac{M^*}{M} = 1 + \alpha \times f_I + \beta \times f_I^2 + ... \tag{6.10}$$

The dilute scheme gives estimates for the first coefficient, α. Estimation of the second coefficient, β, is rather more difficult and requires statistical information on the distribution of particles. Chen and Arcivos [24] and Batchellor and Green [25] proposed results for some specific cases.

Given that the dilute scheme is based on the assumption of a negligible interaction between inclusions, the scheme is restricted to materials with very low particle concentration ($< 3\%$ - [27]) and well-dispersed inclusions.

Composite Sphere Model

The finite concentration of inclusions requires a detailed elastic field analysis satisfying the interface continuity conditions along all particles surfaces. However, introducing a special assumption about the arrangement and morphology of the embedded inclusions, which is due to Hashin [48], allows for the formulation of a realistic estimate. Hashin's

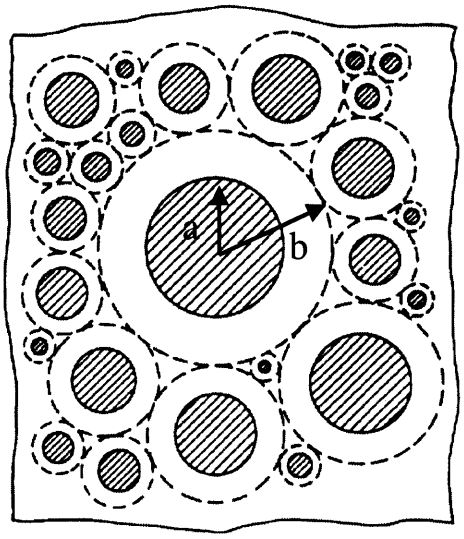

Figure 6-2: Composite sphere model, after [25].

model is shown in Figure 6-2. The main idea of this model relies on identification of a two-phase composite material by a fractal composite sphere arrangement. The corresponding Composite Cylinders Model was introduced by Hashin and Rosen [50]. A composite sphere is defined by an isotropic sphere (crossed area) enclosed in an isotropic concentric shell. In addition, a fixed ratio of radii $a/b = f_I^{1/3}$ is assumed such that the analysis of a single cell is representative of the entire composite. The gradation of sizes ensures a volume filling configuration. The model, therefore, provides good results for actual systems that have a fine gradation of sizes, but fails to represent accurately the elastic modulus of monodisperse systems (systems with single size particles) with high concentrations.

The composite sphere model initially aimed at determining bounds for the elastic moduli. However, in the case of the bulk modulus, the bounds coincided, thus providing

the exact solution, which reads:

$$\frac{K}{K_m} = 1 + \frac{f_I\left(\frac{K_i}{K_m} - 1\right)}{1 + (1 - f_I)\left[\left(\frac{K_i}{K_m} - 1\right) / \left(1 + \frac{4}{3}\frac{G_m}{K_m}\right)\right]} \tag{6.11}$$

In comparison with the dilute scheme, the composite sphere model predicts that the effective bulk modulus depends no more linearly on f_I. This is a consequence of incorporating the interaction of particles in the upscaling scheme. For very low inclusion concentrations, Eq. (6.11) converges to the dilute approximation, Eq. (6.9). While the model provides an exact solution for the bulk modulus, it provides only bounds for the shear modulus. The greater the difference between G_i and G_m, the greater is the difference between these bounds, and the scheme becomes less attractive.

Three-Phase Model or Generalized Self-Consistent Method

The Three-Phase Model provides a means of overcoming the inability to find a solution for the effective shear modulus of the composite spheres model. The model illustrated in Figure 6-3, is similar to the Composite Sphere Model. The only difference is that all but one phase are replaced by an equivalent homogeneous media. In fact, in this model the "matrix phase" (see Figure 6-3) has the effective properties of the composite medium. Applying a homogeneous strain at large distances and solving the elasticity problem, a solution for both the bulk and shear modulus is obtained. For example, the solution for the effective shear modulus G is given by the solution of the quadratic equation:

$$A\left(\frac{G}{G_m}\right)^2 + 2B\left(\frac{G}{G_m}\right) + C = 0 \tag{6.12}$$

where A, B and C are (somewhat complicated) functions of the shear moduli, Poisson's ratios and volumetric proportions of the individual phases composing the composite material. The exact equations for bulk and shear modulus can be found in [49]. In addition, it has been argued that this model provides the exact solution for the effective

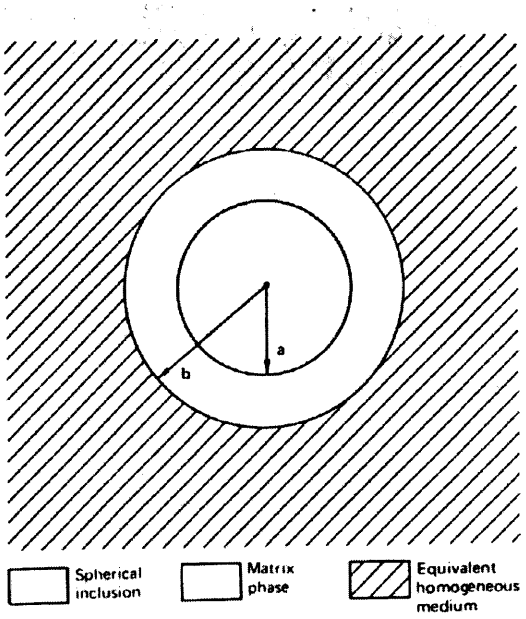

Figure 6-3: Three phase model [25]

shear modulus of the composite sphere model [49]. This originates from the fact that the effective bulk modulus estimation coincides with the one of the composite sphere model, but the proof is still missing. Hervé and Zaoui later extended this model to n-layered model [53].

6.2.3 Variational Approach – Bounds

Variational approaches provide bounds of the effective elastic moduli when exact solutions are not possible. Their practical importance, however, depends on their proximity. Employing the variational principles of stress and strain[1], upper and lower bounds can

[1]Variational principles are intimately related to the theorems of minimum potential (resp. comlementary) energy. The theorem of minimum potential (resp. complementary) energy states that the potential (resp. complementary) energy of a system, $\mathcal{E}_{pot}(\mathbf{x})$ (resp. $\mathcal{E}_{com}(\boldsymbol{\sigma})$) associated with a displacement $\mathbf{x}$ (resp. stress $\boldsymbol{\sigma}$) experiences a minimum when the displacement $\mathbf{x}$ (resp. stress $\boldsymbol{\sigma}$) is the exact solution of the problem. It is then intuitively understood that the potential (resp. complementary) energy associated with any other displcement $\mathbf{x}'$ (resp. $\boldsymbol{\sigma}'$) is greater than or equal to the minimum potential

be obtained for the effective elastic moduli (G, K, E).

The most simple bounds are the Voigt-Reuss bounds, which are obtained by neglecting any particular morphological arrangements of the phases. In this case, strains (resp. stress) are assumed to be uniform in the material. For the case of a macroscopically isotropic composite material containing N phases, the assumption of a uniform state of strain across all phases (i.e., $\forall r$; $\mathbf{A}_r = \mathbf{I}$ in Eq. 6.2), together with the theorem of minimum potential energy, leads to the Voigt upper bound, which is often referred to as the rule of mixtures:

$$K^+ = \sum_{i=1}^{N} f_i K_i; G^+ = \sum_{i=1}^{N} f_i G_i \tag{6.13}$$

Analogously, a uniform state of stress throughout the entire material (i.e., $\forall r$; $\mathbf{B}_r = \mathbf{I}$ in Eq. 6.2) combined with the theorem of minimum complementary energy, yields the Reuss lower bound:

$$\frac{1}{K^-} = \sum_{i=1}^{N} \frac{c_i}{K_i}; \frac{1}{G^-} = \sum_{i=1}^{N} \frac{c_i}{G_i} \tag{6.14}$$

For most practical applications, in which the elasticity of the different phases varies in significant proportions, the bounds are far apart, and are therefore of little practical use for predictive purposes of the macroscopic moduli. This shortcoming motivated Hashin-Strikman (H-S), to develop more stringent bounds based on a refined variational principle of linear elasticity [51]. The considered composite material consists of (in a statistical sense) quasi-isotropic and homogeneous phases of arbitrary geometry. For a two-phase material, considering that phase 1 (volume fraction f_1) is softer than phase 2 ($K_1 < K_2, G_1 < G_2$), the H-S bounds read:

---

energy, $\mathcal{E}_{pot}(\mathbf{x}) \leq \mathcal{E}_{pot}(\mathbf{x}')$ (resp. $\mathcal{E}_{com}(\boldsymbol{\sigma}) \leq \mathcal{E}_{com}(\boldsymbol{\sigma}')$).

$$K^- = K_1 + \frac{1-f_1}{\frac{1}{K_2-K_1} + \frac{3f_1}{3K_1+4G_1}} \leq K \leq K^+ = K_2 + \frac{f_1}{\frac{1}{K_1-K_2} + \frac{3(1-f_1)}{3K_2+4G_2}} \tag{6.15}$$

$$G^- = G_1 + \frac{c_2}{\frac{1}{G_2-G_1} + \frac{6(K_1+2G_1)c_1}{5G_1(3K_1+4G_1)}} \leq G \leq G^+ = G_2 + \frac{c_1}{\frac{1}{G_1-G_2} + \frac{6(K_2+2G_2)c_2}{5G_2(3K_2+4G_2)}} \tag{6.16}$$

It also follows, from the usual relation of Young's modulus E to K and G that,

$$E^{(\pm)} = \frac{9K^{(\pm)}G^{(\pm)}}{3K^{(\pm)} + G^{(\pm)}} \tag{6.17}$$

Improved bounds can be obtained upon an assumption about the morphology of the inclusions. A series of proposals for different morphologies was presented by Zaoui [95].

6.2.4 Approximations

Approximations are by their very nature of unlimited variety, as they depend on the made assumptions. One group of schemes is based on semi-empirical approximations developed without the benefit of a model or theory, containing unknown parameters that are fitted experimentally. More sophisticated models of composite materials form another group. With the help of an assumption that is in principle incorrect, the schemes are based on the premise that the error introduced is insignificant. Some common schemes that fall in the second group are discussed below.

Self-Consistent Scheme (SCS)

Beside the Composite Sphere Model, the Self-Consistent Scheme (SCS) is the most employed model for the determination of macroscopic behavior of isotropic composite media. The SCS is intimately related to percolation theory, and describes best materials characterized by perfect disorder. Originally developed by Hershey and Kröner [52] for a

single phase polycrystalline material, it was extended by Budiansky [17] and Hill [58] to multiphase composites. In the original model, a single crystal is viewed as an ellipsoidal inclusion embedded in an infinite medium of *unknown* isotropic properties of the homogenized medium. The system is subjected to the regular boundary conditions (6.3) at large distance from the inclusion. The boundary value problem is solved for an arbitrary ellipsoidal particle, [31]. The resulting uniform strain in the particle is a function of the effective properties of the surrounding medium. Next, through (6.1), the volume average stress or strain in the inclusion are set equal to the macroscopic stress or strain. The isotropic effective properties are then solved through a set of coupled implicit equations of the bulk modulus K and shear modulus G. For a 2-phase spherical inclusion composite, the following two equations need to be solved numerically:

$$\frac{f_1}{K - K_2} + \frac{1 - f_1}{K - K_1} = \frac{3}{3K + 4G} \tag{6.18}$$

$$\frac{f_1}{G - G_2} + \frac{1 - f_1}{G - G_1} = \frac{6(K + 2G)}{5G(3K + 4G)} \tag{6.19}$$

In the case of multiphase composite material, each phase in the composite is lumped as a single ellipsoidal inclusion in an infinite matrix of unknown homogeneous properties. All phases are treated as inclusions even if the phases are continuous. Applying homogeneous stress or strain at infinity gives volume average relations for each inclusion phase. Repeating the same procedure for all phases, average relations for all phases are obtained as implicit functions of the effective properties. This procedure yields a set of average relations for the entire composite material that needs to be solved numerically along similar lines as the 2-phase composite described by (6.18) and (6.19).

Finally, it is instructive to consider the two extreme cases of (i) an inclusion of infinite stiffness and (ii) an inclusion of zero stiffness (voids). Application of Eqs. (6.18) and (6.19) to these conditions shows that the shear modulus G becomes zero for a volume fraction of $f_1 = 0.5$ in the case of voids; and infinite at a volume fraction of $f_1 = 0.5$

in the case of rigid inclusions. This result is, however, not totally unrealistic, if we associate the zero shear modulus at $f_1 = 0.5$ with a percolation threshold of the solid phase. While this value is on the lower side, percolation thresholds of 60% volume fraction have been reported in the literature [25]. The SCS , therefore, is best suited for high volume fractions with strong interactions. Furthermore, the underlying inclusion boundary value problem of the SCS requires satisfaction of displacement and traction continuity condition at the particle-equivalent body interface. The macroscopic variables (effective variables), therefore, need to be merged with the microscopic ones (inclusion) which is somewhat meaningless, given that the former are averaged quantities of the latter [49]. It could be argued that this merger violates the principle of separation of scales, which is a prerequisite for the application of continuum micromechanics [49].

Mori-Tanaka Scheme

In contrast to the SCS and other homogenization schemes the Mori-Tanaka (MT) model [82] is not based on a precise geometrical interpretation of the matter [27], but involves complex manipulations of the field variables, with special concepts of eigenstrain and backstress, etc. [82]. It has been argued that the MT model is the non-dilute counterpart of the dilute scheme [27], which allows for the account of interactions between particles, thus overcoming the limitation of the dilute scheme.

Figure 6-4(a) shows a Representative Element Volume (A) with a high concentration of inclusions subjected to a uniform strain boundary condition. In the MT model, each particle is considered separately to which the dilute scheme of an inclusion embedded in an infinite matrix subject to a "fictitious" displacement boundary condition is applied (Figure 6-4(b)). The macroscopic strain $\mathbf{E}$ is set equal to the volume average of the strain $\boldsymbol{\varepsilon}$ over the REV A:

$$\langle \boldsymbol{\varepsilon} \rangle_A = \mathbf{E} \tag{6.20}$$

The particle problem shown in Figure 6-4(b), is solved first, based on Eshelby's solution

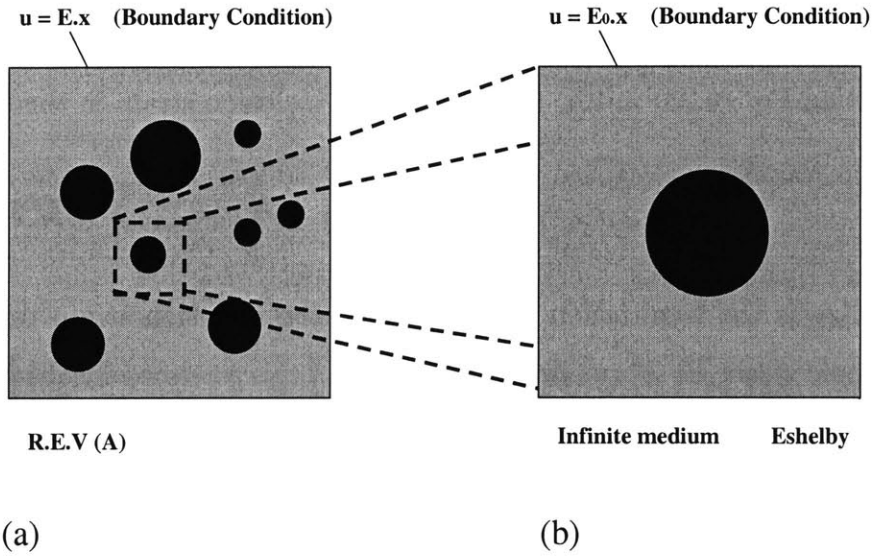

Figure 6-4: Mori-Tanaka approach applied to an R.E.V of high concentration of inclusions (a). Each particle is viewed seperately and the Eshelby solution is utilized (b). u, x are vectors and E, E_0 are second order tensors.

of an ellipsoidal inclusion subjected to the (fictitious) uniform strain boundary condition of the form $(6.3)_I$:

$$\mathbf{u} = \mathbf{E}_0 \cdot \mathbf{x} \tag{6.21}$$

$\mathbf{E}_0$, however, is the "macroscopic" strain for the fictitious REV considered in Figure 6-4(b). The strain in the inclusion ($\boldsymbol{\varepsilon}_I$) is related to $\mathbf{E}_0$ by the strain localization condition (6.3):

$$\boldsymbol{\varepsilon}_I = \mathbf{A} : \mathbf{E}_0 \tag{6.22}$$

The localization tensor $\mathbf{A}$ here is a function of the Eshelby tensor, the local elasticities and the volume fractions of the phases. A combination of (6.20) and (6.22) yields[2]:

[2]For uniform strain ($\mathbf{E}_0$) the following relation holds $\langle \mathbf{A} : \mathbf{E}_0 \rangle_A = \langle \mathbf{A} \rangle_A : \mathbf{E}_0$.

$$\mathbf{E} = \langle \mathbf{A} \rangle_A : \mathbf{E}_0; \quad \mathbf{E}_0 = \langle \mathbf{A} \rangle_A^{-1} : \mathbf{E} \tag{6.23}$$

Substituting Eq. (6.23) in Eq. (6.22) yield the inclusion strain in the form:

$$\boldsymbol{\varepsilon}_I = \mathbf{A}_{MT} : \mathbf{E}; \quad \mathbf{A}_{MT} = \mathbf{A} : \langle \mathbf{A} \rangle_A^{-1} \tag{6.24}$$

where $\mathbf{A}_{MT}$ is the localization tensor relating the inclusion strain to the real far field macroscopic strain $\mathbf{E}$. Through the term $\langle \mathbf{A} \rangle_A^{-1}$, this modified localization tensor allows for interaction between particles to be considered. Note that $\langle \mathbf{A} \rangle_A^{-1} = \mathbf{I}$ corresponds to the dilute scheme.

By way of illustration, we consider a spherical inclusion problem under non-dilute conditions. The MT scheme delivers the effective bulk and shear moduli in the form:

$$K = K_m + \frac{(K_i - K_m) f_I}{1 + a\,(1 - f_I)\left(\frac{K_i}{K_m} - 1\right)} \tag{6.25}$$

$$G = G_m + \frac{(G_i - G_m) f_I}{1 + b\,(1 - f_I)\left(\frac{G_i}{G_m} - 1\right)} \tag{6.26}$$

where K_m (resp. K_i) is the bulk modulus of the matrix (resp. inclusion); G_m (resp.G_i) is the shear modulus of the matrix (resp. inclusion), and a and b in (6.25) and (6.26) read:

$$a = \frac{3K_m}{3K_m + 4G_m}; b = \frac{6}{5}\frac{K_m + 2G_m}{3K_m + 4G_m} \tag{6.27}$$

It is instructive to note that the MT scheme coincides with the lower (resp. upper) Hashin-Strikman bound for rigid inclusions (resp. pores). Furthermore, as in the composite sphere model, Eqs. (6.25) and (6.26) converge to the dilute scheme for $f_I \to 0$.

We will argue in the next Chapter that the Mori-Tanaka Scheme is the most appropriate for upscaling concrete properties over several order of magnitudes.

Chapter 7

A Multi-Step Homogenization Model for Cement-Based Materials

We have seen in Chapter 6 that Continuum Micromechanics provides the elements to upscale elastic properties. While the mesoscopic composite material (concrete, mortar), composed of cement paste as matrix, aggregates as inclusions and the ITZ as the common interface, has been studied in some details, less attention has been paid to lower levels, that is to the cement paste constituents. With both the multiscale structure of concrete of Chapter 2, and the experimental values of Chapter 4 and 5 in mind, this chapter focuses on a two-step homogenization model for the effective properties of hardened cement paste. The chapter is composed of four parts. The micromechanical representation of the multiscale structure of cement-based materials is first discussed. Then, the two-step homogenization procedure for cement paste is developed, which allows upscaling of the elasticity properties from the level of the C–S–H to the macroscale, and this for both the unleached and leached state of the material. Then, the required input parameters to the two-step homogenization model are outlined. Finally, the predictive capabilities of the model are discussed in some details.

7.1 Micromechanical Representation of the Multi-scale Structure of Concrete

The backbone of the micromechanical model is the four-level microstructure of concrete discussed in Chapter 2. We note that this four-level structure satisfies the principle of scale separability, which allows application of the upscaling schemes of continuum micromechanics. In addition, from a morphological point of view, all levels are characterized by a matrix–inclusion geometry that can be effectively treated with the Mori-Tanaka scheme [82]. The Mori-Tanaka scheme, presented in Section 6.2.3, is selected for its simplicity, and its very good performance in the characteristic concentration range of the multiple phases involved (typically, $10 - 30\%$), but also for the range of Poisson's ratios considered ($0.2 \leq \nu \leq 0.31$); cf. [27].

Focus of the micromechanics approach developed below is the effective modulus of cement pastes. The contributions of the different constituents to the macroscopic stiffness of hcp take place at different observation scales. In particular, the two levels that separate the C–S–H phases at level I from the cement paste at level II, suggests a two-step homogenization procedure, as sketched in Figure 7-1:

1. The first step consists in application of an appropriate homogenization scheme to level I ($L = 5 - 10$ μm). This level refers to the smallest material length scale that is, at present, accessible by mechanical testing. For this scale, the nanoindentation results presented in Chapter 5, provide clear evidence of two types of C–S–H, with different elastic properties that affect the overall elasticity of the composite. The average elastic properties determined by nanoindentation (see Table 5.1 and Figure 5-8), however, include the effect of porosity and of any nanocrystalline CH or minor compounds present at smaller scales ($< 1\mu$m). The two types of C–S–H represent phases —in a micromechanical sense. In this sense, the REV (volume V_p), displayed in Figure 7-1(a), is composed of two phases: a low density C–S–H_a-phase, and a

high density C–S–H_b-phase, of volume fractions:

$$f_a = \frac{V_a}{V_p}; \quad f_b = \frac{V_b}{V_p}; \quad f_a + f_b = 1 \tag{7.1}$$

V_a and V_b are the volumes occupied by the two C–S–H phases. The volume fractions of the two C–S–H phases at this scale depend primarily on the $w/c-$ratio, and are not affected by calcium leaching. For $w/c = 0.5$, these volume fractions were obtained from a statistical analysis of the nanoindentation tests (i.e., Figure 5-8). Alternatively, as detailed below, application of advanced physical chemistry models, as the one proposed by Jennings and Tennis [61, 102], provide access to these volume fractions. For $w/c = 0.5$, the volume fractions have been found to be (see Figure 5-8):

$$f_a = 0.7; \quad f_b = 0.3 \tag{7.2}$$

which holds for both unleached and leached cement-based materials. Furthermore, from a morphological standpoint, the difference in stiffness of the two phases found by nanoindentation suggests that the stiffer C–S–H_b-phase plays the role of an inclusion phase embedded into a softer C–S–H_a- matrix. There are several micromechanics schemes suitable for this matrix inclusion morphology: Dilute Scheme, Composite Sphere Model, Three-Phase Model, Mori-Tanaka Scheme, and so on. The high volume fraction of the inclusion phase ($f_b = 0.3$), however, excludes the Dilute Scheme which is restricted to low volume concentrations (typically, $f_I < 3\%$; see Section 6.2.1). While the Composite Sphere Model can accommodate such high volume fractions, the poor grading of the C-S-H_b inclusion phase, which is a consequence of the (mainly mono-sized) cement particles, makes this scheme less effective for our purpose. The Three-Phase Model can accommodate both, high volume fraction and poor grading of the inclusion. However, its predictive capabilities are known to become less effective when considering stiff inclusions in a compressible matrix [26], which is the case given the difference in average stiffness values of the

two C–S–H phases (see Figure 5-8). From these shortcomings, it appears to us that the Mori-Tanaka scheme is best suited for the given homogenization problem, and the simplicity of the scheme makes it even more attractive.

2. The second homogenization step, sketched in Figure 7-1(b), consists in bridging from level I to level II. In this step, the stiffness contribution of large Portlandite crystals, respectively of pores in the case of degraded materials, which take effect at an observation scale of several tens of micrometers, is homogenized over the entire microstructure REV (level II). The characteristic length of volume V_u is $L = 100 - 150\mu$m. The REV is composed of three phases: (i) large CH-Portlandite-crystals (resp. pores for degraded materials) of volume V_{CH}; (ii) the C-S-H matrix resulting from the first homogenization step of volume $V_{\text{C-S-H}}$; and (iii) air voids of volume V_{V}, which are often encountered at high $w/c-$ratios. The volume fractions of the three phases are:

$$f_{\text{CH}} = \frac{V_{\text{CH}}}{V_u};\ f_{\text{C-S-H}} = \frac{V_{\text{C-S-H}}}{V_u};\ f_{\text{V}} = \frac{V_{\text{V}}}{V_u};\ f_{\text{CH}} + f_{\text{C-S-H}} + f_{\text{V}} = 1 \tag{7.3}$$

From a morphological standpoint, CH and air voids can be viewed as spherical inclusions in the C–S–H matrix. In fact, CH crystals in hcp are large and of undetermined shape. Their random orientation can be effectively treated by considering a spherical inclusion morphology for the CH crystal phase. It is reported that in the case of stiff inclusions embedded in a soft matrix, the exact geometry of the inclusions is of minor significance [94]. By contrast, in the the case of voids exact morphological features become of primary importance. SEM pictures (Section 5.1) show that the new group of pores formed with the depletion of CH crystals can be well approximated with spheres. Finally, for similar reasons discussed above, the Mori-Tanaka scheme is adopted for the homogenization of the two types of spherical inclusions in a C–S–H matrix.

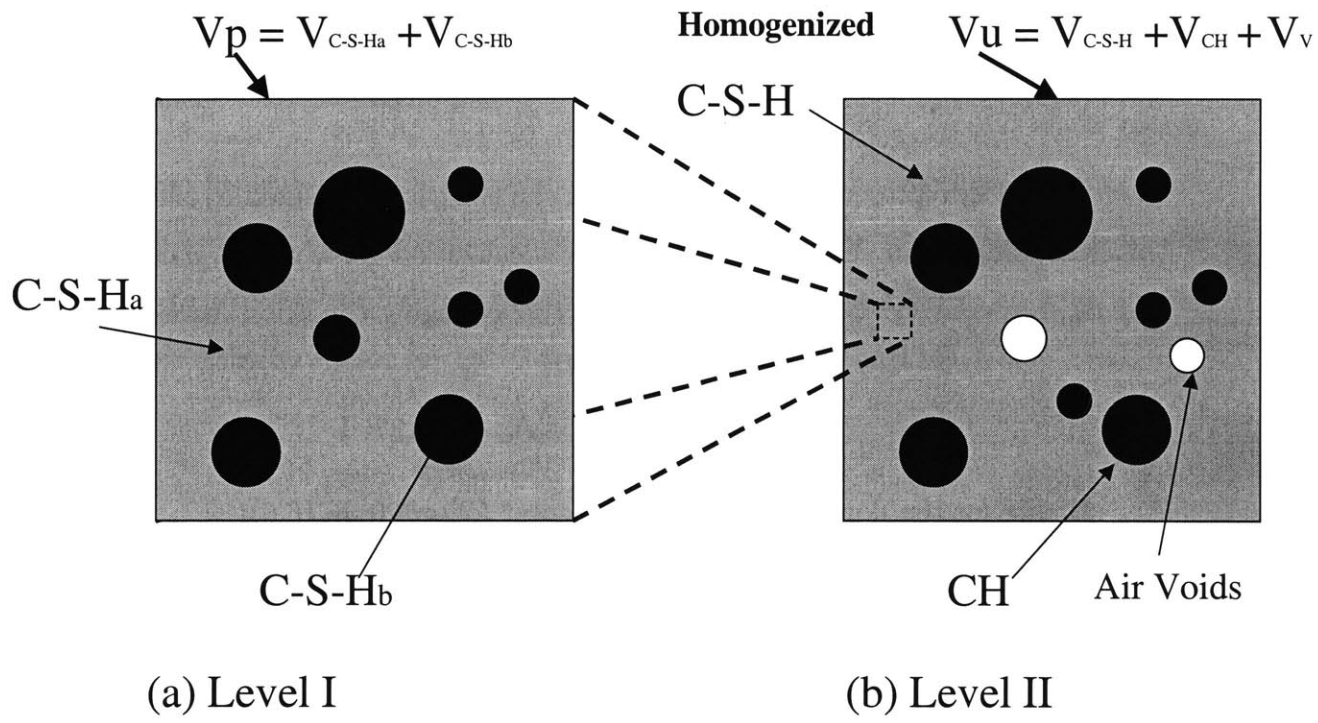

Figure 7-1: Choice of Representative Elementary Volumes (REV) for the two-step homogenization model for cement paste: (a) level I; (b) level II.

7.2 Two-Step Homogenization Procedure for Cement Paste

7.2.1 Step 1: C–S–H Matrix

The C–S–H matrix is considered a two-phase composite material, in which the stiffer C–S–H_b-phase plays the role of inclusion embedded in the softer C–S–H_a-phase considered as matrix. The strain localization relations (6.2) for the two-phases read:

$$\boldsymbol{\varepsilon}_a = \mathbf{A}_a : \mathbf{E}; \quad \boldsymbol{\varepsilon}_b = \mathbf{A}_b : \mathbf{E} \tag{7.4}$$

where $\boldsymbol{\varepsilon}_a$and $\boldsymbol{\varepsilon}_b$ represent the local strains in the two phases, related to the homogeneous (macroscopic) strain tensor $\mathbf{E}$ by 4th-order localization (or concentration) tensors $\mathbf{A}_a$ and $\mathbf{A}_b$, respectively. Combining (7.4) with the averaging condition (6.20) gives:

$$\langle \mathbf{A} \rangle_{V_p} = \mathbf{I} \iff f_a \mathbf{A}_a + f_b \mathbf{A}_b = \mathbf{I} \tag{7.5}$$

An estimate for the homogenized stiffness tensor follows from (6.6):

$$\mathbf{C}_p^{est} = f_a \mathbf{c}_a : \mathbf{A}_a^{est} + f_b \mathbf{c}_b : \mathbf{A}_b^{est} \tag{7.6}$$

where $\mathbf{c}_{r=a,b}$ and $\mathbf{A}_{r=a,b}^{est}$ denote, respectively, the stiffness tensor and an estimate for the localization tensor of the C–S–$H_{r=a,b}$–phases. The localization tensor $\mathbf{A}_{r=a,b}^{est}$ incorporates the information about the morphology, the arrangement and the volume fractions of the phases. In the present case of a matrix/inclusion morphology, estimates of the localization tensors $\mathbf{A}_a^{est}$ and $\mathbf{A}_b^{est}$ are suitably provided by the Mori-Tanaka scheme; for instance for the inclusion phase:

$$\mathbf{A}_b^{est} = \left[\mathbf{I} + \mathbf{S}_b^{esh} : (\mathbf{c}_a : \mathbf{c}_b - \mathbf{I})\right]^{-1} : \left\langle \left[\mathbf{I} + \mathbf{S}_b^{esh} : (\mathbf{c}_a : \mathbf{c}_b - \mathbf{I})\right]^{-1} \right\rangle_{V_p}^{-1} \tag{7.7}$$

where $\mathbf{S}_b^{esh}$ is the Eshelby tensor of phase b. The localization tensor for the matrix phase is conveniently determined from Eq. (7.5):

$$\mathbf{A}_a^{est} = \frac{1}{f_a}\left[\mathbf{I} - f_b \mathbf{A}_b^{est}\right] \tag{7.8}$$

Since both phases and the homogenized material are isotropic, the stiffness tensors $\mathbf{c}_{r=a,b}$ and $\mathbf{C}_p^{est}$ take the form:

$$\mathbf{c}_r = 3k_r\mathbf{K} + 2\mu_r\mathbf{J}; \quad \mathbf{C}_p^{est} = 3k_p^{est}\mathbf{K} + 2\mu_p^{est}\mathbf{J} \tag{7.9}$$

where $k_{r=a,b}$, $\mu_{r=a,b}$, k_p^{est} and μ_p^{est} are the bulk moduli and the shear moduli of the phases $r = a, b$ and the homogenized material; $K_{ijkl} = \frac{1}{3}\delta_{ij}\delta_{kl}$ is the volumetric part of the 4th-order unit tensor $\mathbf{I}$,and $\mathbf{J} = \mathbf{I} - \mathbf{K}$ its deviatoric part. The morphology of isotropic homogenized materials can be reasonably represented by phases filling up spherical inclusions. The Eshelby tensor for the C-S-H$_b$ phase reads as, e.g. [114],

$$\mathbf{S}_b^{esh} = \mathbf{S}_{sph}^{esh} = \alpha^{est}\mathbf{K} + \beta^{est}\mathbf{J} \tag{7.10}$$

with

$$\alpha^{est} = \frac{3k_a}{3k_a + 4\mu_a}; \beta^{est} = \frac{6(k_a + 2\mu_a)}{5(3k_a + 4\mu_a)} \tag{7.11}$$

Finally, substituting (7.9) to (7.11) into (7.6), (7.7) and (7.9) yields the homogenized bulk and shear moduli in the form:

$$k_p^{est} = k_a + \frac{f_b(k_b - k_a)}{1 + \alpha^{est} f_a\left(\frac{k_b}{k_a} - 1\right)} \tag{7.12}$$

$$\mu_p^{est} = \mu_a + \frac{f_b(\mu_b - \mu_a)}{1 + \beta^{est} f_a\left(\frac{\mu_b}{\mu_a} - 1\right)} \tag{7.13}$$

Last, the effective Young's modulus is evaluated from:

$$E_p^{est} = \frac{9k_p^{est}\mu_p^{est}}{3k_p^{est} + \mu_p^{est}} \tag{7.14}$$

7.2.2 STEP 2: Cement Paste

Cement paste is considered as a three-phase composite material, in which the homogenized medium (C-S-H) of Step 1 forms a matrix to accommodate the large Portlandite crystals (CH), and Voids (V). The following micromechanical relations hold for this homogenization step:

$$\varepsilon_{\text{C-S-H}} = \mathbf{A}_{\text{C-S-H}} : \mathbf{E};\ \varepsilon_{\text{CH}} = \mathbf{A}_{\text{CH}} : \mathbf{E};\ \varepsilon_V = \mathbf{A}_V : \mathbf{E} \tag{7.15}$$

$$\langle \mathbf{A} \rangle_{V_u} = \sum_r f_r \langle \mathbf{A} \rangle_r = \mathbf{I} \tag{7.16}$$

$$\mathbf{C}_u^{est} = f_{\text{C-S-H}}\, \mathbf{c}_{\text{C-S-H}} : \mathbf{A}_{\text{C-S-H}}^{est} + f_{\text{CH}}\, \mathbf{c}_{\text{CH}} : \mathbf{A}_{\text{CH}}^{est} + f_{\text{V}}\, \mathbf{c}_{\text{V}}^{est} : \mathbf{A}_{\text{V}}^{est} \tag{7.17}$$

where $\mathbf{c}_{\text{C-S-H}} = \mathbf{C}_p^{est}$ is the stiffness tensor (7.9) from Step 1.

Given the matrix–inclusion morphology, we employ again the Mori-Tanaka scheme for estimates of the localization tensors of the two inclusion phases $r = \text{CH,V}$:

$$\mathbf{A}_r^{est} = \left[\mathbf{I} + \mathbf{S}_r^{esh} : \left(\mathbf{c}_{\text{C-S-H}}^{-1} : \mathbf{c}_r - \mathbf{I}\right)\right]^{-1} : \left\langle \left[\mathbf{I} + \mathbf{S}_r^{esh} : \left(\mathbf{c}_{\text{C-S-H}}^{-1} : \mathbf{c}_r - \mathbf{I}\right)\right]^{-1} \right\rangle_{V_u}^{-1} \tag{7.18}$$

In addition, using Eq. (7.16) yields the one of the matrix phase:

$$\mathbf{A}_{\text{C-S-H}}^{est} = \frac{1}{f_{\text{C-S-H}}} \left[\mathbf{I} - \left(f_{\text{CH}}\mathbf{A}_{\text{CH}}^{est} + f_{\text{V}}\mathbf{A}_{\text{V}}^{est}\right)\right] \tag{7.19}$$

Finally, assuming isotropic elasticity, the stiffness tensors have the form:

Level I		Level II	
Non-Degraded	**Degraded**	**Non-Degraded**	**Degraded**
C-S-H_a	C-S-H_a	C-S-H	C-S-H
C-S-H_b	C-S-H_b	Voids	Voids
		Clinker	Clinker
		CH	

Table 7.1: Phases involved in the two-level homogenization model.

$$\mathbf{c}_{\text{C-S-H}} = \mathbf{C}_p^{est} = 3k_p^{est}\mathbf{K} + 2\mu_p^{est}\mathbf{J};\ \mathbf{c}_r = 3k_r\mathbf{K} + 2\mu_r\mathbf{J}; \mathbf{C}_u^{est} = 3k_u^{est}\mathbf{K} + 2\mu_u^{est}\mathbf{J} \quad (7.20)$$

where k_p^{est} and μ_p^{est} are the bulk modulus and shear modulus of the C–S–H matrix, given by (7.12) and (7.13), respectively; k_r, μ_{r_r}, k^{est} and μ^{est} are the bulk moduli and the shear moduli of the inclusion phases (r = CH,V), and of the homogenized material, i.e. the cement paste.

Last, substituting (7.20), (7.10) and (7.11) into (7.15) to (7.19) yields the homogenized moduli.

7.3 Input Parameters

The micromechanical model requires several input parameters for the effective elastic properties estimation: the elastic moduli and volumetric proportions of each phase. Table 7.1 shows the different phases that need to be considered at each level, in calculating the elastic modulus of cement paste.

7.3.1 Intrinsic Elastic Moduli (Individual constituent)

Table 7.2 summarizes the intrinsic elastic moduli of the individual constituents found in either the open literature, or by our experiments. Several values for the elastic modulus of CH crystals are reported in the open literature, but values for C–S–H and clinker

are scarce. Beaudoin [10] and Wittmann [112] measured the elastic modulus of CH compacts pressurized at different levels to obtain specimens with different porosities. The elastic modulus of these compacts was obtained from three-point bending tests. The intrinsic modulus of CH was found by extrapolating to zero porosity, log E versus porosity curves. The logarithmic relation between elastic modulus and porosity shows a good fit in the range of considered porosities, however no theoretical argument supports that the assumed relationship should hold for low porosity values. The obtained values are shown in Table 7.2. Monteiro [80] used the elastic stiffness coefficients of CH, determined by the use of Brillouin Spectrum[1] in both the V-R bounds and H-S bounds, to obtain the following range of elastic modulus and Poisson's ratios:

$$E_{\mathrm{CH}} = 39.77 - 44.89\mathrm{GPa}; \nu_{\mathrm{CH}} = 0.305 - 0.343 \text{ (V-R)} \tag{7.21}$$

$$E_{\mathrm{CH}} = 39.77 - 44.22\mathrm{GPa}; \nu_{\mathrm{CH}} = 0.305 - 0.325 \text{ (H-S)} \tag{7.22}$$

where E_{CH}, ν_{CH} are the intrinsic elastic modulus and Poisson's ratio of CH crystals. By intrinsic we mean here the elastic properties of the material at zero porosity.

The use of nanoindentation in our experimental procedure (Chapter 5) provide a reliable means of verifying this data.

7.3.2 Volumetric Proportions

The volumetric proportions of the different cement paste constituents can be calculated by considering the hydration reactions of all cement phases[2]. An example is given in Table 7.3, where the hydration of C_3S is considered. Taking $C_{1.7}SH_4$ as the chemical formula of the hydrate and given a density of 2.01, the volumetric proportions of the hydration products can be calculated. The molar volume of the hydrates is lower than the sum of

[1] Measurements of the ultrasonic and hypersonic longitudinal velocities, on grown crystals and at different directions, provide the stiffness coefficients.

[2] Exact volumetric proportions of cement phases are provided in Table 3.1.

Constituent	E (GPa)	Poissons Ratio-ν	Method	Reference
Quartz Aggregates	58			
CH	35.24		E	Beaudoin J.J.(1983) [10]
	48		E	Wittmann F.H.(1986) [112]
	39.77<E<44.22	0.305<ν<0.325	B	Monteiro PJ.M.(1995) [80]
	36±3		I	Acker P.,(2001) [3]
	38±5		I	**
Clinker				
C_3S	135±7	0.3	I	Acker P.,(2001) [3]
	147±5	0.3	E	Velez K. et al (2001) [110]
C_2S	140±10	0.3	I	Acker P.,(2001) [3]
	130±20	0.3	E	Velez K. et al (2001) [110]
C_3A	160±10		I	Acker P.,(2001) [3]
	145±10		E	Velez K. et al (2001) [110]
C_4AF	125±25		E	Velez K. et al (2001) [110]
Alite	125±7		I	Velez K. et al (2001) [110]
Belite	127±10		I	Velez K. et al (2001) [110]
C-S-H	34(includes both types)		E	Beaudoin J.J.(1986) [11]
α	20±2		I	Acker P.,(2001) [3]
	21.7±2.2		I	**
β	31±4		I	Acker P.,(2001) [3]
	29.4±2.4		I	**
C-S-H (Leached)				
α	**3.0 ± 0.8**			**
β	**12.0 ± 1.2**			**

Table 7.2: Intrinsic Elastic properties of cement paste constituents E = Extrapolation, B= Brillouin Spectrum, I= Indentation, *The only information available for the elastic properties of C-S-H comes from nanoindentation performed at a level of 10E-6 m. **Experimental data from Chapter 5.2. Values in bold are used in the homogenization procedure.

	C_3S	+	5.3H	—>	$C_{1.7}SH_4$	+	1.3CH	
Density (g/cm^3)	3.15		1		2.01		2.24	
Molar mass (g)	228		18		227.2		74	
Molar volume (cm^3)	72.38		18		111.37		33.03	
Total volume (cm^3)	167.78				154.3			$\Delta V = -13.48$

Table 7.3: Hydration reaction for C3S

Φ_c	Φ_h	Φ_w	Φ_v	$\varepsilon_c = \Phi_w + \Phi_v$
$\frac{1-\alpha}{1+3.15\frac{w}{c}}$	$\frac{2.13\alpha}{1+3.15\frac{w}{c}}$	$\frac{3.15\frac{w}{c}-1.32\alpha}{1+3.15\frac{w}{c}}$	$\frac{0.19\alpha}{1+3.15\frac{w}{c}}$	$\frac{3.15\frac{w}{c}-1.13\alpha}{1+3.15\frac{w}{c}}$

Table 7.4: Volumetric proportions of indivindual constintuents obtained from the hydration of C3S

the molar volumes in the anhydrous C_3S and the water consumed by the hydration degree (Le Chatelier contraction). For a given hydration degree[3] α, the volumetric proportions of unhydrated cement Φ_c, hydrates Φ_h, water Φ_w and voids Φ_v can be calculated using Table 7.4. This approach, however, cannot discriminate between the two types of C-S-H. Therefore, experimental data or the Jennings-Tennis model should be used. The J-T model is described in detail in Appendix C. Figure 7-2 provides the estimated volumetric proportions of the different hydration products of a cement paste with $w/c-$ratio of 0.5 as predicted by the J-T model. The volumetric proportions obtained by the proposed use of nanoindentation technique coincide with the values suggested by the J-T model (C-S-H_a = 70%, C-S-H_b = 30%).

[3]Hydration degree can be easily measured using calorimetric techniques or using the Powers-Brownyard model. In our case a hydration degree of 1 was considered due to the high $w/c-$ ratio of 0.5.

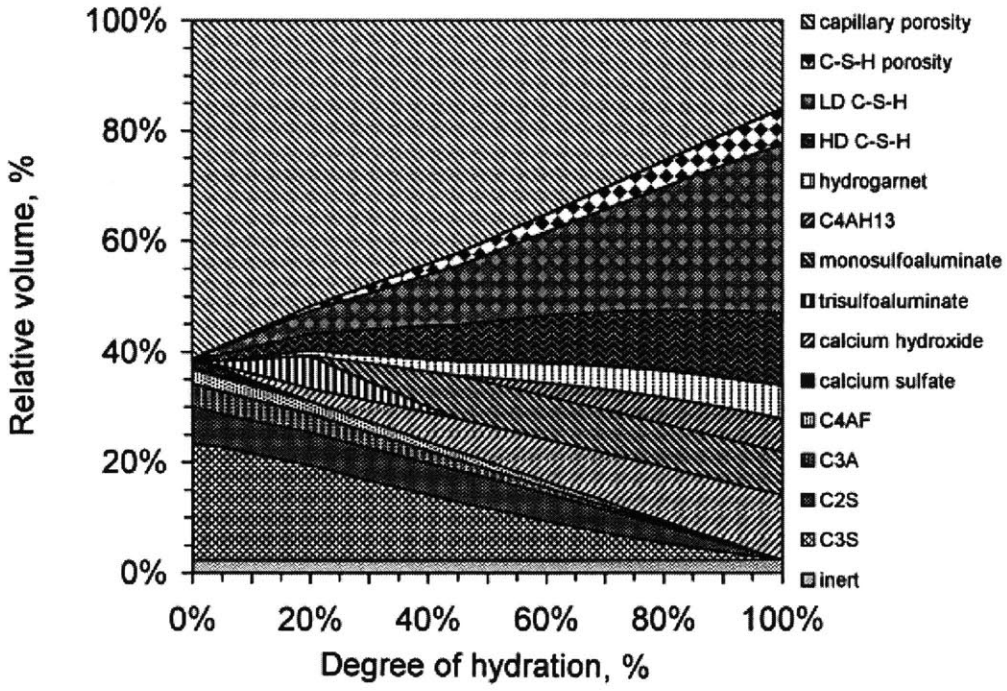

Figure 7-2: Relative volume of each of the phases (as predicted by the J-T model) as a function of the degree of hydration. The example is for a paste with water:cement ratio of 0.50, and 55% C_3S, 18% C_2S, 10% C_3A, and 8% C_4AF, an average Type I cement composition [102].

7.4 Application of the Micromechanical Model

7.4.1 Non-Degraded Cement Paste

Level I

The intrinsic elastic properties of the two types of C-S-H are:

$$E_a = 21.7\,\text{GPa};\quad E_b = 29.4\ \text{GPa} \tag{7.23}$$

The Poisson's ratio for both phases is unknown, and will be assumed to be the same, $\nu_a = \nu_b = 0.24$. Volumetric proportions, estimated using the J-T model and confirmed with nanoindentation experiments, are $f_a = 0.3$ and $f_b = 0.7$. Given this data, the elastic modulus of the homogenized medium can be calculated by using Eqs. (7.12)-(7.14), yielding

$$E_p^{est} = E_{\text{C-S-H}} = 23.8\ \text{GPa} \tag{7.24}$$

Level II

Due to the high $w/c-$ratio (> 0.38) and the continues curing of the samples, the hydration degree is taken as 1 (see Sections 2.1.1 and 2.2.1), and a clinker phase need not to be considered. The input parameter are:

- The elastic properties of the two phases:

$$E_{\text{C-S-H}} = 23.8\ \text{GPa};\quad E_{\text{CH}} = 38.0\ \text{GPa};\ \nu_{\text{C-S-H}} = 0.24;\ \nu_{\text{CH}} = 0.31 \tag{7.25}$$

- Volumetric proportions which are estimated using the J-T model, and are confirmed by the hydration reaction demonstrated before; A 3% of air voids [3] for a $w/c = 0.5$ was in addition considered; thus:

$$f_{\text{C-S-H}} = 0.86;\quad f_{\text{CH}} = 0.11;\quad f_{\text{V}} = 0.03 \tag{7.26}$$

Use of this values in the homogenization model yields the following value

$$E_u^{est} = 23.2 \text{ GPa} \tag{7.27}$$

which almost coincides with the experimental value $E = 22.8$ GPa obtained by UPV-measurements.

7.4.2 Degraded Cement Paste

Level I

The intrinsic input parameters for the calcium leached material at level I are:

$$E_a = 3.0\,\text{GPa}; \quad E_b = 12.0 \text{ GPa}; \; \nu_{\text{C-S-H}_a} = \nu_{\text{C-S-H}_b} = 0.24 \tag{7.28}$$

The volumetric proportions of the two types were found to be not affected by calcium leaching, thus, $f_a = 0.3$ and $f_b = 0.7$. Use of this data set in Eqs. (7.12), (7.13) and (7.14), yields for the degraded C–S–H matrix:

$$E_p^{est} = E_{\text{C-S-H}} = 4.3 \text{ GPa} \tag{7.29}$$

Level II

The area previously occupied by the large CH crystals, at level II, is now replaced by pores embedded in the homogenized medium. The volumetric proportions of the two phases are:

$$f_{\text{C-S-H}} = 0.86; \; f_{\text{V}} = 0.14 \tag{7.30}$$

where the void volume fraction, f_{V}, was calculated by adding to the initial value of 3% of voids the volume fraction of CH present in the non-degraded specimen (11%). The only input parameter is now the C–S–H matrix stiffness (7.29), and the value of the Poisson's ratio $\nu_{\text{C-S-H}} = 0.24$. This data set yields the following predicted stiffness for the calcium

	Elastic Modulus, E (GPa)		
	UPV measurement	**Prediction**	**Error (%)**
Non-Degraded	22.8	23.2	2
Degraded	3.6	3.5	3

Table 7.5: Elastic modulus of Degraded and Non-Degraded Cement Paste as Measured by UPV and Predicted by the proposed model.

leached cement paste:

$$E_u^{est} = 3.5 \text{ GPa} \tag{7.31}$$

The value is in good agreement with the experimentally determined value of $E = 3.6$ GPa.

Table 7.5 summarizes the values predicted by the model for the $w/c = 0.5$ cement paste. With an error of only 3%, the model predicts with great accuracy the effective elasticity of cement pastes, for both the non-degraded and the degraded state.

7.4.3 Predictive Capabilities of the Model

Calcium Leaching

We want to evaluate the relative importance of C-S-H decalcification compared to large CH crystal dissolution on the macroscopic elastic stiffness. To this end, we apply the model to two hypothetical scenarios:

Scenario 1: Assume a cement paste with no large CH crystals (i.e. consumed in a pozzolanic reaction) subjected to calcium leaching. The predicted elastic modulus is $E_u^{est} = 4.3$ GPa, that is a residual value of 19% of the initial value of the non-degraded specimen.

Scenario 2: The C-S-H phase is assumed to remain unaffected after leaching with only the large CH crystals being depleted. In this case, the completed degraded cement paste has an elastic modulus $E_u^{est} = 18.7$ GPa, that is 81% of its initial value.

These two scenarios demonstrate the significance of C-S-H decalcification on the overall loss of elastic stiffness, which contributes 4 times more than the CH crystal dissolution. The C-S-H phase dominates the volumetric proportions of cement paste materials, and its contribution to the macroscopic elastic performance is, therefore, significant.

Ultra High Performance Concrete (UHPC)

Application of the model to ultra high performance concrete (UHPC) requires consideration of the clinker phase on level II, along similar micromechanical lines as the consideration of Portlandite crystals. For a UHPC of $w/c = 0.2$, and a hydration degree of $\alpha = 40\%$, the model predicts an elastic modulus on the order of $E_u^{est} = 60$ GPa, which is on the same order as experimental values of 55–65 GPa [3]. Unreacted cement particles appear to act as a natural reinforcement to the cementitious composite, and dominate the stiffness. In addition, the good link of the clinker to the hydration products avoids the introduction of a weak interphase.

Scale Effects

The model suggests that any constituent present at a specific scale will have a more significant effect (weight) than the effect of the same constituent (with the same volume fraction) present at a lower length scale. This may explain why small pores present at the length scale of the 10^{-9}m contribute little to the macroscopic elasticity whereas the porosity present at high length scales, i.e. air voids of a size of 10^{-3}m, appear to be detrimental to the elastic modulus. This suggests that the higher the characteristic length scale of the constituent the more significant the contribution.

7.5 Concluding Remarks

The two-step homogenization model predicts the effective macroscopic behavior of cement paste with a high degree of accuracy. This model can serve as input for already

existing upscaling schemes for mortars (level III) and concrete (level IV), e.g. [68, 69]. However, in this case, the ITZ need to be added as an additional phase. To show the importance of the ITZ, figure 7-3 displays the Voigt-Reuss and Hashin-Strikmann bounds for degraded mortar treated as a two phase composite (Aggregate-Cement Paste), in which the ITZ was neglected. The figure also displays the macroscopic experimental results on mortar, which lie not only outside the H-S bounds, but also outside the V-R bounds. This underlines the importance of the ITZ on the effective behavior of mortar and concrete. A three-phase model that considers the ITZ requires further information on the volumetric proportions and the elastic properties of the ITZ. Several researchers performed quantitative analysis on the ITZ [87, 116, 117], and several models have been proposed [37, 71]. But a generalization seems still out of reach, given that the mechanical properties (and most probably the volumetric proportions of the ITZ) depend on the CH-content, ettringite, and so on, which are dissolved during calcium leaching (see Section 2.1.2). Further investigations on the mechanical properties and volumetric proportions of the ITZ are necessary to properly predict the loss of elastic stiffness of mortars subjected to leaching.

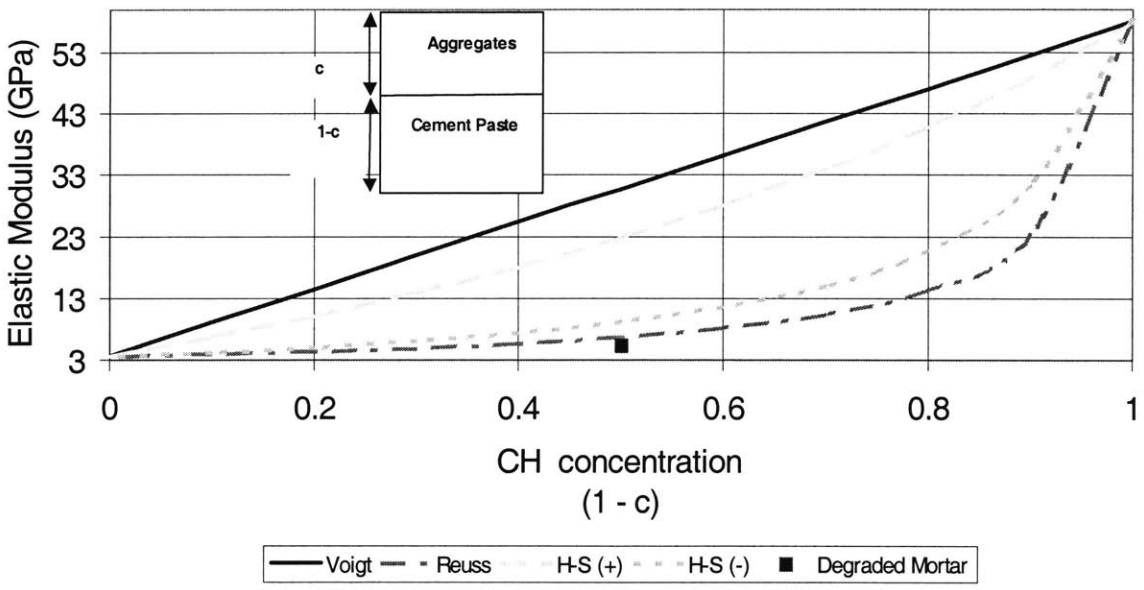

Figure 7-3: Elastic Modulus of degraded mortar as compared with the Voigt-Reuss and Hashin-Strikmann bounds

Chapter 8

Conclusions and Perspectives

The impact of calcium leaching induced aging on the long-term dimensional stability is of great concern for long-term health-monitoring of concrete structures exposed to a wetting environment. In recent years, a sound knowledge base emerged to address this problem, first in physical chemistry, and more recently in Durability Mechanics. The research results presented in this thesis contribute to this knowledge base through a study of the evolution of the microstructure, and the development of a scale bridging micromechanical approach that addresses the loss of elastic modulus of the material at different scales.

A short review of the additional knowledge gained and conclusions drawn from this study is presented below. Then some perspectives for future research are developed.

8.1 Review of Results

8.1.1 Structure of Concrete

To address the multiscale effect of calcium leaching induced aging, we propose a modified Powers and Brownyard model that incorporates two types of C-S-H and their characteristic porosity. The experimental results obtained in this study confirm the existence of two types of C-S-H with intrinsic elastic properties originating (probably) from a characteristic packing during the hydration process. The formation of low elasticity C-S-H_a

takes place at the early stages of hydration in water saturated conditions, thus favoring a more loosely packed configuration (low density). By contrast, the high density C-S-H_b are formed at later stages of hydration, driven by complex diffusion processes that favor a better arrangement of particles, packed in a dense configuration. Indentation results obtained in this research compare well with other indentation data [3] obtained for other cement-based materials of different mix design ($w/c-$ratio, etc.), suggesting that the found elasticity properties are intrinsic to cement paste. By intrinsic we mean that the elastic properties of the two types of C-S-H are independent of the mix proportions, which affect only the volumetric proportions of the two types of C-S-H. Calcium leaching leads to a loss of this intrinsic elasticity, but the volume fractions of the two types of C-S-H are not affected. This suggests that the calcium leaching induced aging occurs in a homogeneous way in the C-S-H matrix.

8.1.2 Calcium Leaching

The experimental and theoretical results developed in this study provide evidence of the origins of the macroscopic degradation of the elastic stiffness of calcium leached cement-based material. Macroscopic measurements record residual values on the order of 16% and 20% of the initial elastic stiffness of both cement paste and mortar, respectively. The drop in macroscopic elasticity is a coupled consequence of (i) the increased porosity which manifests itself primarily in form of large pores present at a length scale of $10^{-5} - 10^{-4}$ m, the space previously occupied by large CH crystals; and (ii) the loss of intrinsic elasticity of the C-S-H phase by decalcification. The decalcification of the C-S-H phase appears to be the primary source of the macroscopic elastic modulus degradation. In particular, the low density C-S-H_a-phase appears to be more vulnerable to chemical degradation than the dense C-S-H_b-phase. This suggests that a cement paste with a higher volumetric proportion of C-S-H_b will be less affected by calcium leaching induced aging.

8.1.3 Two-step Homogenization Model for Cement Paste

The two types of C-S-H are considered in a micromechanics model for cement paste that incorporates the cement paste constituents and their volumetric proportions. Combined with the J-T model, which provides the volume fractions of the two types of C-S-H for a given $w/c-$ratio, the model predicts the elastic modulus of any cement paste with high accuracy. Since all cement paste constituents are incorporated in the model, the model equally applies to chemically degraded materials. In addition, a new experimental method is proposed that gives direct access to the volumetric proportions of the two types of C-S-H. Results obtained with this method are in excellent agreement with the values provided by the J-T model.

8.2 Future Perspectives

The indentation results of two significantly different cement-based materials (our results and Acker's results [3]) provide strong evidence that the elastic properties of the two types of C-S-H are intrinsic to cement paste. Additional experimental data is required to confirm this finding.

In addition, the experimental investigation adopted in this thesis circumvents, by design, the effect of calcium leaching on cement paste containing unhydrated cement particles. The high $w/c-$ratio of the considered material ensures that no clinker is left in the hardened microstructure. Future research should focus on the effect of chemical degradation on the unhydrated cement paste, because the type of concrete employed in nuclear containments have typically a low $w/c-$ratio, and consequently a high degree of unhydrated cement.

Finally, our study focusses on the two asymptotic states of degradation. In a next step, it is important to link these two asymptotic states. This requires a model based on non-equilibrium thermodynamics, that bridges between the two asymptotic states studied in this thesis. Such a model, then, has the premise to predict, in space and time,

the effects of calcium leaching induced aging on the dimensional stability of concrete structures; and long-term health monitoring will become possible. This is the focus of on-going research.

Appendix A

Porosity and Density Measurements

A.1 Porosity Measurements

The porosity measurements in this study were obtained by drying to 105 °C. To appreciate this method, it is useful to recall the different types of water present in cement-based materials.

A.1.1 Water in Hardened Cement Paste

The major contribution in this field is due to Feldman and Sereda [33]. Material presented below owes much to the Feldman-Sereda model. The model suggests that due to the high surface area of C-S-H there is a large affinity for water molecules to be absorbed on the surface. In fact, water can exist in cement paste in 5 different forms:

1. Water vapor: Water vapor is found in partially filled larger voids of the macropores. It occupies the empty space, and contributes to the thermodynamic equilibrium of the water-vapor system in the capillary pores.

2. Capillary water: Water in the capillary and larger pores is free from the influence of the attracting surface forces. Water in voids larger than 50 nm is considered to be free, and its removal does not result in any deformation or volume change.

3. Adsorbed water: Water under the influence of attractive surface forces, is referred to as adsorbed water. $5 - 6$ molecular layers form a surface layer $1.3 - 1.5$ nm thickness. This water is lost after drying the sample below 30% relative humidity (RH).

4. Interlayer water: This is the water form between two solid surfaces, is usually held in micropores by hydrogen bonding. A RH less than 11% can cause its removal, which leads to shrinkage deformation and volumetric changes.

5. Chemically combined water: This water is chemically combined within the different hydration products. It is not lost, except at very elevated temperatures at which chemical decomposition of the individual constituent takes place.

A.1.2 Measurements

The Feldman and Sereda model indicates that water and therefore porosity is contained within a layered structure of the C-S-H phase ranging in size from macroscopic to enlarged interlayer spaces of nanometer dimensions. One can, therefore, only define porosity measurements in relation with a specific drying condition and the liquid (Helium, Methanol, Water) used. In our experiments, water saturated samples were weighted and then dried at 105 °C. The principal assumption of this technique is that water is accessible to the entire pore structure of hardened cement paste, and consequently the weight loss is a measure of the total porosity. Based on the Feldman and Sereda model, a temperature of 105 °C is enough to cause the free water (water vapor, capillary water, absorbed water and interlayer water) to evaporate; thus giving a measure of total porosity. Special attention was paid to a dry surface of the specimens before measuring the saturated weight. The relevance of porosity measurements by drying is still an on-going debate. Indeed, it has been argued that a part of the chemically bound water is lost from the interlayer spaces under the conditions employed in our study [99]. Nevertheless, since both degraded and non-degraded samples were subject to the same drying conditions, mea-

surements recorded are expected to provide (at least) a relative measure of the porosity change induced by calcium leaching.

A.2 Density Measurements

In our study, density values were determined from volume and mass measurements. Length and weight measurements were performed with an accuracy of 0.01 mm and 0.001 g, respectively. In order to ensure the good accuracy of our results, additional measurements using "Archimedes Principle" were also performed and compared. Samples were weighted in air (W_{air}) and in water (W_{water}) and the corresponding density was determined from:

$$\rho_{sample}=\rho_{water} \times \frac{W_{air}}{W_{air} - W_{water}} \tag{A.1}$$

where ρ_{sample} and ρ_{water} = density of the sample and the water; W_{air} and W_{water} = weight of the sample in air and water. The two techniques gave identical results.

Appendix B

Theoretical Framework for Sharp Indentation (LEXCOM)

The following outline of the indentation method follows in parts the presentation given by Giannakopoulos and Suresh in [42]. It is included here for the purpose of completion of our experimental analysis.

B.1 Introduction

The elastic modulus of a material can be easily estimated by recourse to continuous indentation. Some complications may arise however in clearly interpreting the indentation results. Such a complication arises from the "pile-up" or "sink-in" of the material around the indenter, which is primarily affected by the plastic properties of the material [41]. In a low-strain-hardening alloy for example , plastically displaced material tends to flow up to (and pile-up against) the faces of the indenter due to the incompressibility of plastic deformation. The result is a "barrel-shaped" impression due to pile-up around the sharp polygonal indenter, as shown in Figure B-1(a). On the other hand, for high-strain-hardening materials, the plastically deformed region is pushed out from the indenter with the imprint sinking below the initial surface level. The result is a "pin-cushionlike" im-

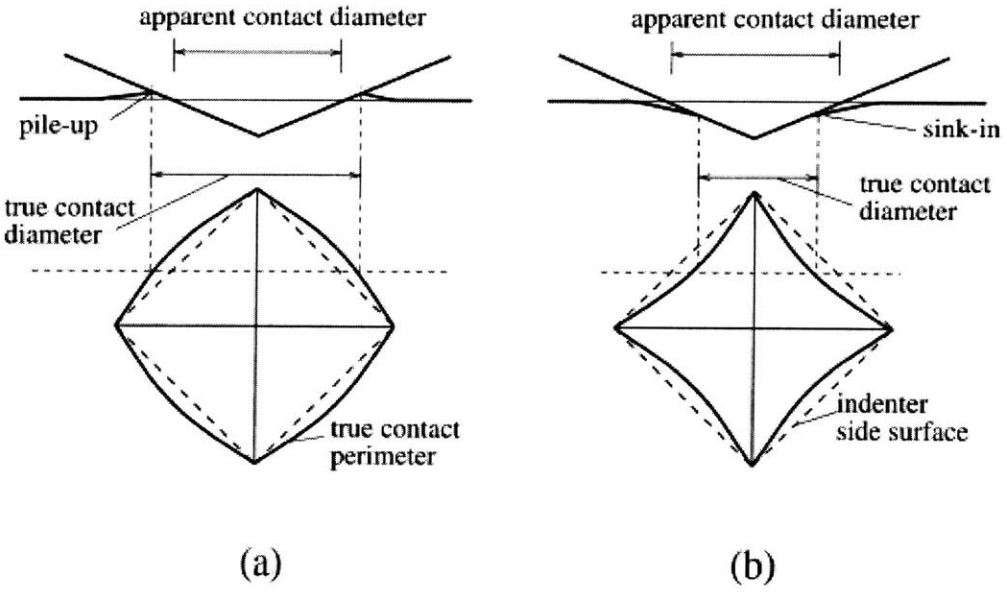

Figure B-1: Schematic illustrations of (a)pile-up and (b)sink-in around a sharp indenter.

pression around the sharp indenter, as shown in Figure B-1(b). Methods which properly account for pile-up or sink-in around the indenter are essential for the interpretation of the plastic properties of materials by recourse to instrumented indentation.

As a consequence of pile-up or sink-in, large differences may arise between the true contact area (which is influenced by the pile-up and sink-in of the materials and which is often difficult to assess in-situ during indentation) and the apparent contact area which is usually observed after indentation. A knowledge of the relationship between the indentation load and the true (projected) contact area, however, is essential to extract the mechanical properties from instrumented indentation. This difficulty can be overcome if explicit expressions, relating the true contact area A and the depth of penetration of the indenter h into the material being tested, are known a priori for different indenter geometries.

In this Appendix, we recall some of the elements of the theoretical framework for

instrumented sharp indentation and outline a methodology which enables the determination of elastic properties of materials by employing instrumented sharp (i.e. Vickers or Berkovich) indentation. The present description deals with the "inverse" problem of extracting material properties through instrumented indentation and is based on the work of Giannakopoulos and Suresh [42]. A key feature of the method outlined here is that it provides unique correlations between penetration depth h and true contact area A for commercially available sharp indenters; the method also circumvents the need for contact area measurement through visual observations while, at the same time, taking into account pile-up and sink-in. Results on the equivalence between an energy approach and the displacement approach to indentation is also presented. Details of the numerical simulations from which the results of Giannakopoulos and Suresh [42] are extracted can be found in Refs. [41,96,98].

B.2 Theory for Sharp Indentation

Within the context of continuum analyses, sharp pyramidal or conical indenters lead to geometrically similar indentation states. That is, for a given indenter shape or included tip angle, the average contact pressure, $p_{av} = P/A$, is independent of the indentation load P or the true contact area A. It depends only on the included angle at the tip of the indenter (e.g. [97]). This average contact pressure is identified with the hardness H. Detailed three-dimensional, large-strain, plasticity simulations [40,41,67] reveal that the tip radius of the sharp indenter, R, has a negligible effect on indentation and the $P-h$ curve provided that the depth of penetration of the indenter into the material, $h > R/40$. In addition, adhesion and friction between the indenter and the substrate were found to have only a small effect on the hardness and the $P-h$ curve.

Experiments [23] and computations [41] also show that there exists a unique characteristic equivalent plastic strain, which separates different modes of plastic deformation directly beneath the sharp indenter. This is schematically shown in Figure B-2. The

innermost region comprises a zone where the material is "cut" by the sharp indenter; this cutting mode is amenable to analysis by means of the classical slip-line theories of rigid-perfect plasticity [70]. Surrounding this region is a zone of strong gradients in plastic strains which is engulfed by an elastoplastic regime where the so-called "cavity" model can be applied to extract the hemi-spherically shaped elastoplastic boundary. A unique characteristic strain separates the innermost "cutting" region from its surroundings. Elaborate studies [23, 41] on the characteristic plastic strain suggest a value in the range $0.25 - 0.36$. In subsequent discussion, we use a fixed value of the characteristic strain of 0.29, which has been identified through finite element analyses of a wide range of ductile metals subjected to sharp indentation. The characteristic strain is independent of the indenter size or indentation load (provided that $h > R/40$), and is weakly influenced by the tip angle of the sharp indenter. Spherical or other blunt indenters do not lead to such a characteristic strain. Invoking the existence of this characteristic strain is a key step in the determination of mechanical properties by sharp indentation [41, 96–98].

B.2.1 Force-Depth ($P-h$) Relations and the Displacement Approach

Figure B-4 gives a scheme of the load-penetration depth ($P - h$) curve for a sharp indenter. During loading, the curve generally follows the relation, $P = Ch^2$, where C is the indentation curvature which is a measure of the "resistance" of the material to indentation. The contact pressure, $p_{av} = P_{max}/A_{max}$, can be identified with the hardness of the indented material; P_{max} is the maximum indentation load which makes the indenter penetrate the material by a depth h_{max}, thereby creating a true (projected) contact area A_{max} on the indented surface. Three-dimensional finite-element simulations of elastoplastic indentation along with experiments [114—117] provide the following result:

$$C = \frac{P}{h^2} = M_1 \sigma_{0.29} \left\{ 1 + \frac{\sigma_y}{\sigma_{0.29}} \right\} \left\{ M_2 + \ln \left(\frac{E^*}{\sigma_y} \right) \right\}, \text{for } 0.5 \leq \frac{p_{av}}{\sigma_y} \leq 3.0 \qquad \text{(B.1)}$$

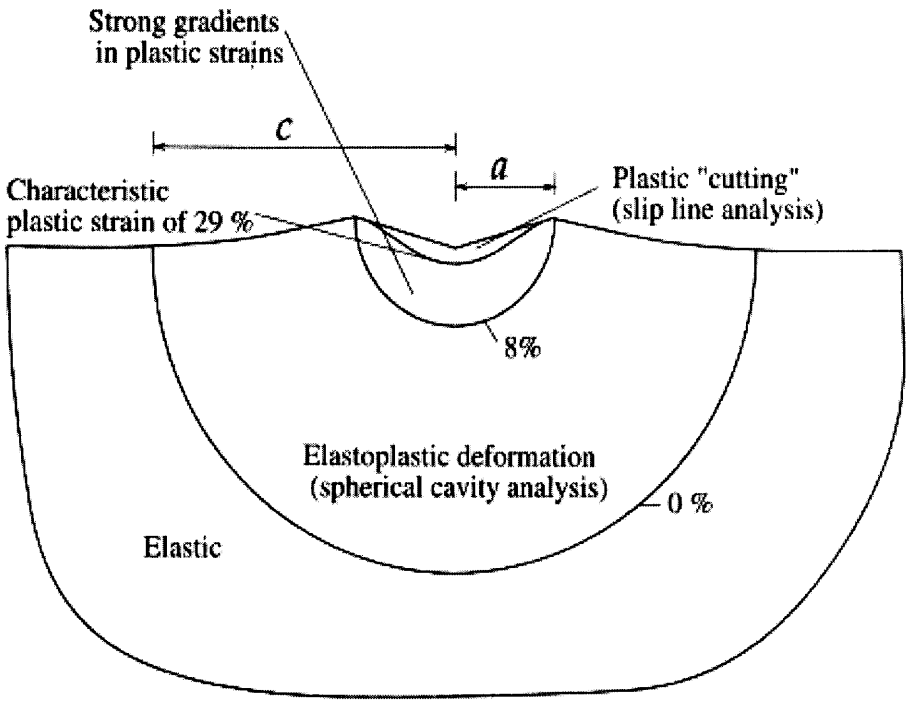

Figure B-2: Different regimes of plastic flow at the tip of a sharp indenter.

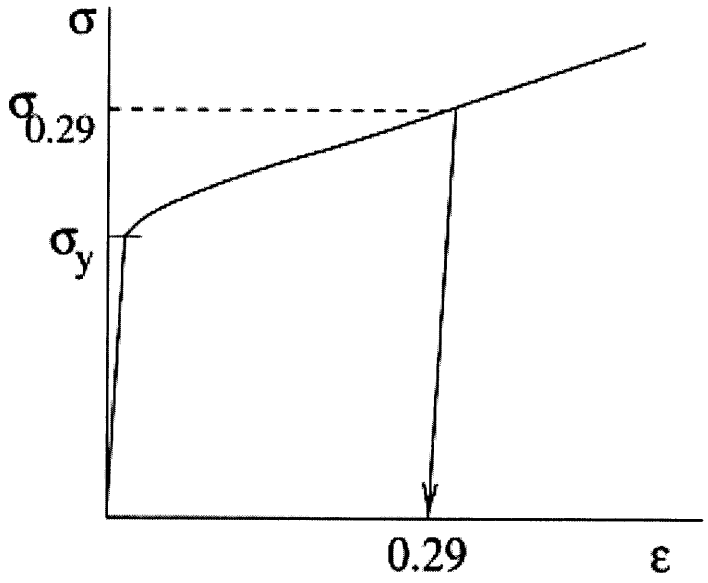

Figure B-3: Uniaxial compression stress-strain curve and the characteristic strain.

In Eq. (B.1), σ_y is the yield strength and $\sigma_{0.29}$ is the stress corresponding to the characteristic plastic strain of 0.29 for the indented material in uniaxial compression, as shown schematically in Figure B-3. The constants in this equation are $M_1 = 7.143$ and $M_2 = -1$ for the Vickers pyramid indenter with an included tip angle of 136°. The corresponding values for the Berkovich indenter are $M_1 = 6.618$ and $M_2 = -0.875$ with an included tip angle of 130.6°. If p_{av}/σ_y falls outside the bounds given in Eq. (B.1), the indentation response is either elastic (for $p_{av}/\sigma_y < 0.5$) or elastic-perfectly plastic (for $p_{av}/\sigma_y < 0.5$ = 3). By accounting for the effects of strain hardening on pile-up and sink-in, and on the true contact area through three-dimensional simulations, the following relationship between A_{max} and h_{max} has been derived for elastoplastic materials [41]:

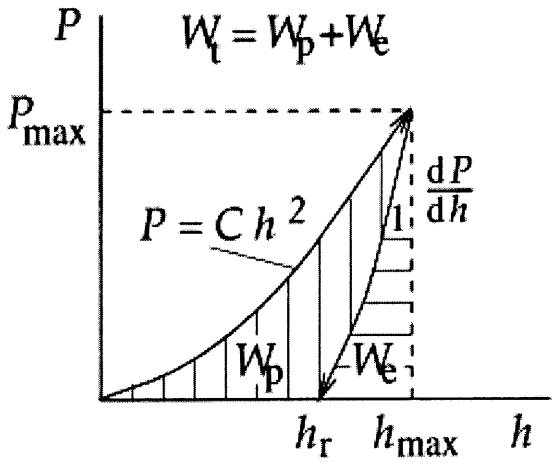

Figure B-4: $P - h$ curves for loading and unloading, and the associated nomenclature.

$$\frac{A_{\max}}{h_{\max}^2} = 9.96 - 12.64(1-S) + 105.42(1-S)^2 - 229.57(1-S)^3 + 157.67(1-S)^4 \quad \text{(B.2)}$$

with $S = \frac{p_{av}}{E^*}$.This equation is a polynomial fit to the computationally determined values of A_{max}/h_{max}^2 , which are listed in the table of Figure B-5. More accurate analytical fits to the results can be obtained from the results of the table by using higher order polynomials or other functional approximations. In Eq. (B.2), the effective elastic modulus of the indenter-specimen system, E^*, is defined as

$$E^* = \left[\frac{1-\nu^2}{E} + \frac{1-\nu_{in}^2}{E_{in}}\right]^{-1} = \frac{1}{c^*\sqrt{A_{max}}}\left(\frac{dP}{dh}\right) = \frac{d^* p_{av}}{\left(1 - \frac{W_p}{W_t}\right)} \quad \text{(B.3)}$$

where ν is Poisson's ratio, E is Young's modulus, the subscript 'in' denotes properties of the indenter, and dP/dh is the slope of the $P - h$ curve of the initial stages of unloading from P_{max} (see Figure B-4). The constant $c^* = 1.142$ for the Vickers pyramid indenter and 1.167 for the Berkovich indenter. The ratio of the residual depth of penetration, h_r upon complete unloading (see Figure B-4) to the maximum penetration depth, h_{max},

prior to unloading, is indicative of the extent of plastic deformation and strain hardening [41,96,98], such that

$$\frac{\sigma_{0.29} - \sigma_y}{0.29E^*} = 1 - 0.142\frac{h_r}{h_{\max}} - 0.957\left(\frac{h_r}{h_{\max}}\right)^2 \tag{B.4}$$

This result holds for Vickers and Berkovich indenters. This equation, which is a polynomial fit to the computational results of the table in Figure B-5, converges to the correct trends in the following two limiting cases. (1) For elastic indentation where $h_r = 0$, the right hand side of Eq. (B.4) obviously reduces to 1 indicating that $\frac{\sigma_{0.29}-\sigma_y}{0.29} = E^*$ for linear elastic response. (2) For the case of a rigid-perfectly plastic material where h_r/h_{max}, the right hand side of Eq. (B.4) reduces to zero indicating no strain hardening. Different intermediate hardening responses during sharp indentation can be quantified with greater precision using the results shown in Figure B-5, and accounting for the influence of the initial yield strain, σ_y/E^*. Elastoplastic finite element analyses of the sharp indenter, performed in [42] and [41], also reveal that

$$\frac{h_r}{h_{\max}} = 1 - d^*\frac{p_{av}}{E^*} = 1 - d^*S \tag{B.5}$$

where $d^* = 5$ for the Vickers pyramid indenter and $d^* = 4.678$ for the Berkovich indenter. Eq. (B.5) is in reasonable accord with the empirical result of Breval and MacMillan [26] who employed Vickers indentation for a variety of materials. As shown in Figure B-5, $h_r/h_{max} = 0.875$ gives the critical strain hardening for which there is neither a pile-up nor a sink-in of the material around the indenter. Combining Eqs. (B.2) and (B.5) readily provides a unique relationship between A_{max} and h_{max}, i.e., the true contact area which takes into account pile-up and sink-in can be extracted directly from the $P - h$ curve without the need for any visual observations.

$\{\sigma_{0.29} - \sigma_y\}/(0.29E^*) + 11\frac{\sigma y}{E^*}$	$(h_r/h_{max}) = (W_p/W_t)$	A_{max}/h^2_{max}
1	0.00	9.82
0.33	0.76	16.00
0.27	0.85	24.50
0.05	0.91	25.50
0.025	0.94	28.99
0.00	1.00	41.65

Note: (a) Pile-up occurs when $0.875 < (h_r/h_{max}) \leq 1$.
(b) Sink-in occurs when $0 \leq (h_r/h_{max}) < 0.875$.
(c) No pile-up or sink-in when $(h_r/h_{max}) = 0.875$, where the true contact area A and the apparent contact area A_{app} are equal, i.e. $A = A_{app} \approx 24.5h^2$ (for Vickers indentation).

Figure B-5: Numerically Determined Correlations Between Material Strain Hardening, Residual Impression Depth, and Maximum Contact Area.

B.2.2 The Energy Approach

>From a practical standpoint, the measurement of residual depth h_r from instrumented indentation is generally prone to considerable experimental error due to a variety of factors, such as the roughness of the indented surface. As a result, the area under the $P - h$ curve, which provides a measure of elastic and plastic energy components of deformation during indentation, was developed in [42] as an equivalent, but practically convenient, method for extracting mechanical properties. There is a direct equivalence between the plastic energy of indentation and the residual depth, h_r, which was proposed in [42]. The area under the loading portion of the $P - h$ curve is a measure of the total work, W_t, done by the indenter in deforming the material:

$$W_t = \int_0^{h_{\max}} P(h)dh = \int_0^{h_{\max}} Ch^2 dh = \frac{Ch_{\max}^3}{3} = \frac{P_{\max}h_{\max}}{3} = \frac{P_{\max}^{1.5}}{3\sqrt{C}} \qquad \text{(B.6)}$$

Here, the commonly accepted notion that $P = Ch^2$ is invoked for the sharp indenter. As shown in Figure B-4, the total work W_t can be decomposed into elastic and plastic parts: $W_t = W_e + W_p$. The computations presented here following [42] reveal that

$$\frac{W_e}{W_t} = 1 - \frac{W_p}{W_t} = 1 - \frac{h_r}{h_{\max}} = d^* \frac{p_{av}}{E^*} = d^* S \tag{B.7}$$

The foregoing results on the equivalence between the displacement approach and the energy approach were validated in [42] with the aid of available experimental evidence. With the above theoretical framework, and using the step-by-step method presented in Chapter 5 local and bulk mechanical properties can be estimated.

Appendix C

Jennings and Tennis (J-T) Model

The following outline of the Jennings and Tennis (J-T) model follows in parts the description given in [102] and [61]. The J-T model was developed based on experimental data base extracted from the open literature. The basis of the model is that C-S-H forms as one of two types, High- or Low-density C-S-H. Based on this concept, a microstructure for C-S-H is proposed that is consistent with a series of experimental data (surface area measurements, nitrogen sorption etc.) and that provides a means of quantifying, through physical chemistry, the volumetric proportions of each cement paste constituent (hydration products), including the two types of C-S-H.

C.1 Description of the model

The first task is to determine the quantity of C-S-H and other components in the microstructure of cement pastes. The model assumes simple stoichiometric reactions for the hydration of the four dominant compounds in Portland cement, C_3S, C_2S, C_3A, and C_4AF. These formulas proposed in [102] are adopted to accurately reflect current theories on cement hydration (see Eqs. (C.1-C.6)):

$$2C_3S + 10.6H \rightarrow C_{3,4} - S_2 - H_8 + 2.6CH \tag{C.1}$$

$$2C_2S + 8.6H \rightarrow C_{3,4} - S_2 - H_8 + 0.6CH \tag{C.2}$$

$$C_3A + 3C\bar{S}H_2 + 26H \rightarrow C_6A\bar{S}_3H_{32} \tag{C.3}$$

$$2C_3A + 3C_6AS_3H_{32} + 4H \rightarrow C_4A\bar{S}H_{12} \tag{C.4}$$

$$C_3A + CH + 12H \rightarrow C_4AH_{13} \tag{C.5}$$

$$C_4AF + 2CH + 10H \rightarrow 2C_3(A,F)H_6 \tag{C.6}$$

The first two equations are the most important as they define the quantity of C-S-H formed. The composition for C-S-H is reasonably well established as being valid in neat Portland cement pastes. Eq. (C.3) is used for the initial reactions of C_3A in the presence of sulfate to form Ettringite. After the initial supply of sulfate is depleted, Eq. (C.4) is used for additional C_3A hydration to form monosulfoaluminates. Eq. (C.5) is used for continued hydration of C_3A after all ettringite is consumed. In Eq. (C.6), the product of the ferrite reaction is a hydrogarnet. Although several other aluminum-bearing compounds are known to form under various conditions [102], the set of reactions used here are consistent with current ideas about the nature of early reactions of the interstitial phases and the formation of the major products of long-term hydration.

Given the composition of the cement and the water/cement ratio (w/c-ratio), the governing chemical and kinetic equations provide a means of computing the quantity of the various phases present in the microstructure at any given time. The percentage of capillary porosity, V_{cp}, is calculated as follows:

$$V_{cp} = V_w - \sum (V_p - V_r) \tag{C.7}$$

where V_w is the initial volume percent of water, V_p is the volume percent of hydration product, V_r is the volume percent of reactant, and the summation is over all reactions. The volume of gel porosity is included in the volume of C-S-H.

In this model, the distribution of C-S-H into each type is determined by assuming that the LD C-S-H is the only component of the microstructure that contributes appreciably to

the surface area as measured by nitrogen. Each type of C-S-H contains a specific amount of total gel porosity: none of the pores in HD C-S-H are accessible to nitrogen, while only some of the pores in LD C-S-H are accessible to nitrogen. Nitrogen adsorption data on D-dried samples is used to calibrate the model and provide estimates of the formation of the two types of C-S-H. Defining M_r, the ratio of the mass of LD C-S-H to the total mass of C-S-H:

$$M_r = \frac{S_{N_2} M_D}{S_{LD} M_t} \tag{C.8}$$

where S_{N_2} is the specific surface area of the dried paste (determined from nitrogen sorption isotherms), M_D is the mass of dried paste, S_{LD} is the surface area per gram of D-dried LD C-S-H (which is not independently measurable), and M_t is the total mass of C-S-H. Using multiple linear regression, an equation for M_r is obtained [102] that is applied to other data:

$$M_r = 3.017(w/c)\alpha - 1.347\alpha + 0.538 \tag{C.9}$$

where w/c is the water/cement ratio and α is the degree of hydration. Once the the mass ratio is calculated, via Eq. (C.9), the volume percentage of HD C-S-H is given by:

$$V_{HD} = \frac{M_t - M_r M_t}{\rho_{HD}} \tag{C.10}$$

and the volume percentage of LD C-S-H by::

$$V_{LD} = \frac{M_r M_t}{\rho_{LD}} \tag{C.11}$$

where V_x is the volume of x, ρ_x is the density of x, and M_t is the total mass of C-S-H. The additional volume of pores in LD C-S-H is shown in Eq. (C.12):

$$V_P = V_{LD} - \frac{M_r M_t}{\rho_{HD}} \tag{C.12}$$

where V_P is the volume of additional porosity in the LD. The variables remaining to be determined are ρ_{HD}, ρ_{LD} and S_{LD}. Values obtained after optimizing the model are proposed in [102].

Bibliography

[1] *BS 1881: Part 209, Recommendations for the measurements of dynamic modulus of elasticity*, 1990.

[2] *ASTM C 597-83, Standard test method for Pulse Velocity through concrete*, 1991.

[3] P. Acker. Micromechanical analysis of creep and shrinkage mechanisms. In F.-J. Ulm, Z.P. Bazant, and F.H. Wittmann, editors, *Creep, Shrinkage and Durability Mechanics of Concrete and other quasi-brittle Materials*, Cambridge, MA, August 2001. Elsevier, Oxford UK.

[4] F. Adenot. *Durabilité du béton: Caractérisation et Modélisation des Processus Physiques et Chimiques de Dégradation du Ciment.* PhD dissertation, University of Orleans, France, 1992. In French.

[5] P. C. Aitcin. Cements of yesterday and today - concrete of tomorrow. *Cement and Concrete Research*, 30(9):1349–1359, September 2000.

[6] M. F. Ashby and D. R. H. Jones. *Engineering Materials I: An Introduction to Their Properties and Applications.* Pergamon, 1980.

[7] ASTM. *C 215-91, Test method for fundamental transverse, longitudinal, and torsional frequencies of concrete specimens.*

[8] B. D. Barnes, S. Diamond, and W. L. Dolch. Micro-morphology of the interfacial zone around aggregates in portland-cement mortar. *Journal of the American Ceramic Society*, 62(1-2):21–24, 1979.

[9] V. Baroghel-Bouny. *Caractérisation des pâtes de ciment et des bétons. Méthodes, analyse, interprétations.* PhD dissertation, ENPC, France, 1994. In French.

[10] J.J. Beaudoin. Comparison of mechanical properties of compacted calcium hydroxide and portland cement paste systems. *Cement and Concrete Research*, 13:319–324, 1983.

[11] J.J. Beaudoin and R.F. Feldman. Dependence of degree of silica polymerization and intrinsic mechanical properties of C-S-H on C/S. In *8th International Congress on the Chemistry of Cement*, Rio de Janeiro, 1986.

[12] C. Le Bellégo. *Couplages chimie - mécanique dans les structures en béton attaquées par l'eau: étude expérimentale et analyse numérique.* PhD dissertation, ENS Cachan, France, 2001. In French.

[13] D.P. Bentz and E.J. Garboczi. Modelling the leaching of calcium hydroxide from cement paste: effects on pore space percolation and diffusivity. *Materials and Structures*, 25:523–533, 1992.

[14] Bernal et al. *Magazine of Concrete Research*, 2:1, 1952.

[15] U. R. Berner. Modelling the incongruent dissolution of hydrated cement minerals. *Radiochimica Acta*, 44/45:387–393, 1988.

[16] Brooks and Newman. The structure of concrete. In *Proceedings of (an international conference)*, page xvi, London, 1965.

[17] B. Budiansky. One the elastic moduli of some heterogeneous media. *J. Mech. Phys. Solids*, 13:223, 1965.

[18] M. Buil, E. Revertegat, and J. Oliver. Modeling cement attack by pure water. In *Int. Symp. On Stabilization /Solidification of Hazardous, Radioactive and Mixed Wastes*, Williamsburg, 1990.

[19] C. N. S. Instruments Limited, 61-63 Homes road, London. *Pundit Manual*, 1975.

[20] C. Carde. *Caractérisation et Modélisation de l'altération des Proprietés Mécaniques Due a la Lixiviation des Matériaux Cimentaires.* PhD dissertation, INSA Toulouse, France, 1996. In French.

[21] C. Carde and R. Francois. Effect of the leaching of calcium hydroxide from cement paste on mechanical and physical properties. *Cement and Concrete Research*, 27(4):539–550, 1997.

[22] C. Carde, R. Francois, and J.M. Torrenti. Leaching of both calcium hydroxide and C-S-H from cement paste: Modeling the mechanical behavior. *Cement and Concrete Research*, 26(8):1257–1268, 1996.

[23] M. M. Chaudhri. Subsurface strain distribution around vickers hardness indentations in annealed polycrystalline copper. *Acta Materialia*, 46(9):3047–3056, May 1998.

[24] H. S. Chen and A. Acrivos. Effective elastic-moduli of composite-materials containing spherical inclusions at non-dilute concentrations. *International Journal of Solids and Structures*, 14(5):349–364, 1978.

[25] R. M. Christensen. *Mechanics of Composite Materials.* John Wiley and Sons, New York, 1979.

[26] R. M. Christensen and K. H. Lo. Solutions for effective shear properties in 3 phase sphere and cylinder models. *Journal of the Mechanics and Physics of Solids*, 27(4):315–330, 1979.

[27] R.M. Christensen. A critical evaluation for a class of micromechanics models. *Journal of the Mechanics and Physics of Solids*, 38(3):379–404, 1990.

[28] U.J. Counto. The effect of the elastic modulus of the aggregate on the elastic modulus , creep and creep recovery of concrete. *Magazine of Concrete Research*, 16(48):129–138, 1964.

[29] S. Diamond. Aspects of concrete porosity revisited. *Cement and Concrete Research*, 29(8):1181–1188, August 1999.

[30] M. F. Doerner and W. D. Nix. A method for interpreting the data from depth sensing indentation instruments. *J. Mater. Res.*, 1:601–609, 1986.

[31] J. D. Eshelby. The determination of the elastic field of an ellipsoidal inclusion. *Proc. R. Soc. London A*, 241:376–392, 1957.

[32] P. Faucon, A. Delagrave, J.C. Petit, C. Richet, J.M. Marchand, and H. Zanni. Aluminum incorporation in calcium silicate hydrate (c-s-h) depending on their ca/si ratio. *Journal of Physical Chemistry B*, 103:7796–7802, 1999.

[33] R. F. Feldman and Sereda. A model for hydrated portland cement paste as deduced from sorption-length change and mechanical properties. *Materials and structure-sEngineering Journal*, 6:509–19, 1968.

[34] E. J. Garboczi and D. P. Bentz. Digital-simulation of the aggregate-cement paste interfacial zone in concrete. *Journal of Materials Research*, 6(1):196–201, January 1991.

[35] E. J. Garboczi and D. P. Bentz. Multi-scale picture of concrete and its transport properties: Introduction for non-cement researchers. Internal Report 5900, NIST, 1996.

[36] E. J. Garboczi and D. P. Bentz. Multiscale analytical/numerical theory of the diffusivity of concrete. *Advanced Cement Based Materials*, 8(2):77–88, September 1998.

[37] E.J. Garboczi and D.P. Bentz. Analytical formulas of interfacial transition zone properties. *Advanced Cement Based Materials*, 6:99–108, 1997.

[38] B. Gérard. *Contribution des couplages mécanique-chimie-transfert dans la tenue à long terme des ouvrages de stockage des déchets radioactifs.* PhD dissertation, ENS Cachan, France, 1996. In French.

[39] J. T. Germaine. Personal communication.

[40] A. E. Giannakopoulos and P. L. Larsson. Analysis of pyramid indentation of pressure-sensitive hard metals and ceramics. *Mechanics of Materials*, 25(1):1–35, January-February 1997.

[41] A. E. Giannakopoulos, P. L. Larsson, and R. Vestergaard. Analysis of vickers indentation. *International Journal of Solids and Structures*, 31(19):2679–2708, October 1994.

[42] A.E. Giannakopoulos and S. Suresh. Determination of elastoplastic properties by instrumented sharp indentation. *Scripta Materialia*, 40(10):1191–1198, 1999.

[43] Gonnerman et al. Effect of end conditions of cylinder on compressive strength of concrete. *Proc. ASTM*, 24 Part II:1036, 1924.

[44] Gonnerman et al. Effect of size and shape of test specimen on compressive strength of concrete. *Proc. ASTM*, 25 Part II:237–250, 1925.

[45] G. W. Groves. In *Symposium Proceedings* [78], page 3.

[46] S. A. Hamid. The crystal-structure of the 11-A natural tobermorite $Ca_{2.25}[Si_3O_{7.5}(OH)_{1.5}].1H_2O$. *Zeitschrift Fur Kristallographie*, 154(3-4):189–198, 1981.

[47] T. C. Hansen. *Swedish Cement and Concrete Research Inst.*, 29, 1958.

[48] Z. Hashin. The elastic moduli of heterogenous material. *ASME Journal of Applied Mechanics*, 29:143–150, 1962.

[49] Z. Hashin. Analysis of composite-materials - a survey. *Journal of Applied Mechanics-Transactions of the ASME*, 50(3):481–505, 1983.

[50] Z. Hashin and B. W. Rosen. The elastic moduli of fiber reinforced materials. *ASME Journal of Applied Mechanics*, 31:223–232, 1964.

[51] Z. Hashin and J. Shtrikman. A variational approach to the theory of the elastic behaviour of multiphase material. *Journal of Mechanics of Solids*, 11:127–140, 1963.

[52] A. V. Hershey. The elasticity of an isotropic aggregate of anisotropic cubic crystals. *Journal of Applied Mechanics*, 21:236, 1954.

[53] E. Herve and A. Zaoui. n-layered inclusion-based micromechanical modelling. *International Journal of Engineering Science*, 31(1):1–10, 1993.

[54] F. Heukamp. *Experimental and Theoretical Durability Mechanics of Concrete: The Case of Calcium Leaching.* PhD dissertation, Massachusetts Institute of Technology, USA, 2002. In preparation.

[55] F.H. Heukamp, F.-J. Ulm, and J.T. Germaine. Mechanical properties of calcium leached cement pastes: Triaxial stress states and the influence of the pore pressure. *Cement and Concrete Research*, 31(5):767–774, 2001.

[56] F.H. Heukamp, F.-J. Ulm, and J.T. Germaine. Poroplastic properties of calcium leached cement-based materials. *Cement and Concrete Research*, 2001. Submitted for publication.

[57] R. Hill. The elastic behavior of a crystalline aggregate. *Proceedings of the Physical Society of London A*, 65:349–354, 1952.

[58] R. Hill. A self-consistent mechanics of composite materials. *J. Mech. Phys. Solids*, 13:213, 1965.

[59] T.J. Hirsch. Modulus of elasticity of concrete affected by elastic moduli of cement paste matrix and aggregate. *Journal of the American Concrete Institute. Proceedings*, 59(3):427–452, 1962.

[60] J. M. Illston. *Construction Materials: Their Nature and Behavior.* E and FN Spon, 2nd edition, 1996.

[61] H. M. Jennings. A model for the microstructure of calcium silicate hydrate in cement paste. *Cement and Concrete Research*, 30(1):101–116, January 2000.

[62] R. Jones. *Non-Destructive Testing of Concrete.* Cambridge University Press, London, 1962.

[63] R. Jones et al. Recommendations for testing concrete by the ultrasonic pulse method. *Materials and Structures/Research and Testing*, 2(10):275–284, July-August 1969.

[64] M. F. Kaplan. *Concrete Radiation Shielding.* Concrete Design and Construction. Longman Scientific and Technical, New York, 1989.

[65] Kesler and Higuchi. Determination of compressive strength. *Proceedings ASTM*, 53:1044–1051, 1953.

[66] Ralph A. Kohl, editor. *Proceedings of a Session on Nuclear Waste Handling and Storage*, Boston, MA, October 1986. ASCE and ASCE national convention.

[67] P. L. Larsson, A. E. Giannakopoulos, E. Soderlund, D. J. Rowcliffe, and R. Vestergaard. Analysis of berkovich indentation. *International Journal of Solids and Structures*, 33(2):221, January 1996.

[68] G. Q. Li, Y. Zhao, and S. S. Pang. Four-phase sphere modeling of effective bulk modulus of concrete. *Cement and Concrete Research*, 29(6):839–845, June 1999.

[69] G. Q. Li, Y. Zhao, S. S. Pang, and Y. Q. Li. Effective young's modulus estimation of concrete. *Cement and Concrete Research*, 29(9):1455–1462, September 1999.

[70] F. J. Lockett. *J. Mech. Phys. Solids*, 11:345, 1963.

[71] M. P. Lutz, P. J. M. Monteiro, and R. W. Zimmerman. Inhomogeneous interfacial transition zone model for the bulk modulus of mortar. *Cement and Concrete Research*, 27(7):1113–1122, July 1997.

[72] M. Mainguy and O. Coussy. Propagation fronts during calcium leaching and chloride penetration. *ASCE J.Engrg. Mech.*, 126(3):250–257, 2000.

[73] V.M. Malhotra. *Testing hardened concrete: Nondestructive Methods.* American Concrete Institute, 1976.

[74] J. C. Maso. Interfacial transition zone in concrete. Report 11, RILEM, 1996.

[75] Megaw et al. *Nature*, 177:390, 1956.

[76] P. K. Mehta and D. Manmohan. In *Proceedings of the 7th International Congress on Chemistry of Cement*, Paris, 1980.

[77] P. K. Mehta and P. J. M. Monteiro. *Concrete: Structures, Properties and Materials.* Prentice Hall, 2nd edition, 1993.

[78] Mindess and Shah, editors. *Bonding in Cementitious Materials, Symposium Proceedings*, volume 114, Pittsburg, PA, 1988. Materials Research Society, MRS.

[79] P. J. M. Monteiro. A note on the Hirsch model. *Cement and Concrete Research*, 21(5):947–950, September 1991.

[80] P. J. M. Monteiro and C. T. Chang. The elastic-moduli of calcium hydroxide. *Cement and Concrete Research*, 25(8):1605–1609, December 1995.

[81] P. J. M. Monteiro and C. P. Ostertag. Analysis of the aggregate cement paste interface using grazing-incidence X-ray scattering. *Cement and Concrete Research*, 19(6):987–988, November 1989.

[82] T. Mori and K. Tanaka. Average stress in matrix and average elastic energy of materials with misfitting inclusions. *Acta Metallurgica*, 21(5):571–574, 1973.

[83] C. M. Neubauer, H. M. Jennings, and E. J. Garboczi. A three-phase model of the elastic and shrinkage properties of mortar. *Advanced Cement Based Materials*, 4(1):6–20, July 1996.

[84] A. M. Neville. *Properties of Concrete.* Longman group, 4th edition, 1995.

[85] A. U. Nilsen and P. J. M. Monteiro. Concrete - a 3-phase material. *Cement and Concrete Research*, 22(1):147–151, 1993.

[86] Obert and Duvall. Discussion of dynamic methods of testing concrete with suggestions for standardization. *Proceedings ASTM*, 41:1053–1070, 1941.

[87] I. Odler and A. Zurz. Structure and bond strength of cement aggregates interfaces. In Mindess and Shah [78], pages 21–27.

[88] W. C. Oliver and G. M. Pharr. An improved technique for determining hardness and elastic-modulus using load and displacement sensing indentation experiments. *Journal of Materials Research*, 7(6):1564–1583, June 1992.

[89] ORNL and John Hopkins University. Report on aging of nuclear power plant reinforced concrete structures. Technical report, U. S. Nuclear Regulatory Commission (NRC), 1996.

[90] X. Ping, J. J. Beaudoin, and R. Brousseau. Flat-aggregate portland-cement paste interfaces 1: Electrical conductivity models. *Cement and Concrete Research*, 21(6):999–1005, 1991.

[91] John W. Rayleigh. *The Theory of Sound.* Dover Press, New York, 2nd edition, 1945.

[92] I.G. Richardson. The nature of C-S-H in hardened cements. *Cement and Concrete Research*, 29:1131–1147, 1999.

[93] H. Saito, S. Nakane, S. Ikari, and A. Fujiwara. Preliminary experimental study on the deterioration of cementitious materials by an acceleration method. *Nuclear Engineering and Design*, 138:151–155, 1992.

[94] P. Simeonov and S. Ahmad. Effect of transition zone on the elastic behavior of cement-based composites. *Cement and Concrete Research*, 25(1):165–176, January 1995.

[95] P. Suquet. Effective properties of nonlinear composites. In P. Suquet, editor, *Continuum Micromechanics*, number 377 in CISM Courses and Lectures, pages 197–264. Springer, Wien New York, 1997.

[96] S. Suresh and A. E. Giannakopoulos. Report Inst 2/98, Massachusetts Institute of Technology, 1998.

[97] S. Suresh and A. E. Giannakopoulos. A new method for estimating residual stresses by instrumented sharp indentation. *Acta Materialia*, 46(16):5755–5767, October 1998.

[98] S. Suresh, A. E. Giannakopoulos, and J. Alcala. Spherical indentation of compositionally graded materials: Theory and experiments. *Acta Materialia*, 45(4):1307–1321, April 1997.

[99] H. F. W. Taylor. *Chemistry and Industry*, 9:620, 1981.

[100] H. F. W. Taylor. Bs 1881: Part 203, ultrasonic pulse velocity meauserements. *BS*, 1986.

[101] H.F.W. Taylor. *Cement Chemistry.* Thomas Telford, London, 2nd edition, 1997.

[102] P. D. Tennis and H. M. Jennings. A model for two types of calcium silicate hydrate in the microstructure of portland cement pastes. *Cement and Concrete Research*, 30(6):855–863, June 2000.

[103] C. Tognazzi. *Couplage Fissuration - Dégradation chimique dans les matériaux cimentaires: Caractérisation et modélisation.* PhD dissertation, INSA Toulouse, France, 1998. In French.

[104] D. L Turcotte and G. Schubert. *Applications of Continuum Physics to GEological Problems.* John Wiley and Sons, 1982.

[105] F.-J. Ulm. Durability mechanics. Lecture Notes, MIT, 2001.

[106] F.-J. Ulm. Mechanics of material systems. Lecture Notes, MIT, 2001.

[107] F.-J. Ulm et al. Monitoring the durability performance of concrete in nuclear waste containment. Annual report, Department of Energy, 2000.

[108] F.-J Ulm, J.-M. Torrenti, and F. Adenot. Chemoporoplasticity of calcium leaching in concrete. *ASCE Journal of Engineering Mechanics*, pages 1200–1211, 1999.

[109] Varghese et al. Testing concrete by ultrasonic pulse. relation between wave velocity and compressive strength. *The Indian Concrete Journal*, 32(2):46–49;52, 1958.

[110] K. Velez, S. Maximilien, D. Damidot, G. Fantozzi, and F. Sorrentino. Determination by nanoindentation of elastic modulus and hardness of pure constituents of portland cement clinker. *Cement and Concrete Research*, 31(4):555–561, 2001.

[111] T. A. Venkatesh, K. J. van Vliet, A. E. Giannakopoulos, and S. Suresh. Determination of elasto-plastic properties by instrumented sharp indentation: Guidelines for property extraction. *Scripta Materialia*, 42(9):833–839, April 2000.

[112] F. H. Wittmann. Estimation of the modulus of elasticity of calcium hydroxide. *Cement and Concrete Research*, 16(6):971–972, November 1986.

[113] C. C. Yang and R. Huang. Double inclusion model for approximate elastic moduli of concrete material. *Cement and Concrete Research*, 26(1):83–91, January 1996.

[114] A. Zaoui. Materiaux heterogenes et composites. Lecture Notes, Ecole Polytechnique, Paris, in French, 1997.

[115] M. H. Zhang et al. The microstructure of the cement aggregates interfaces. In Mindess and Shah [78], pages 89–95.

[116] W. Zhu and P. J. M. Bartos. Assessment of interfacial microstructure and bond properties in aged GRC using a novel microindentation method. *Cement and Concrete Research*, 27(11):1701–1711, November 1997.

[117] W. Z. Zhu and P. J. M. Bartos. Application of depth-sensing microindentation testing to study of interfacial transition zone in reinforced concrete. *Cement and Concrete Research*, 30(8):1299–1304, August 2000.

[118] R. W. Zimmerman, M. S. King, and P. J. M. Monteiro. The elastic-moduli of mortar as a porous-antigranulocytes material. *Cement and Concrete Research*, 16(2):239–245, March 1986.